MARMARA UNIVERSITY
INSTITUTE FOR GRADUATE STUDIES
IN PURE AND APPLIED SCIENCES

MAGNETO-POLYMERIC MICROWAVE COMPOSITES AND THEIR APPLICATION IN ANECHOIC CHAMBER PAINT

SERDAR GÖKÇE

MASTER THESIS
Department of Physics

Thesis Supervisor
Prof. Dr. Şahin Aktaş

ISTANBUL, 2017

MARMARA UNIVERSITY
INSTITUTE FOR GRADUATE STUDIES IN PURE AND APPLIED SCIENCES

MAGNETO-POLYMERIC MICROWAVE COMPOSITES AND THEIR APPLICATION IN ANECHOIC CHAMBER PAINT

SERDAR GÖKÇE
(521213001)

MASTER THESIS
Department of Physics

Thesis Supervisor
Prof. Dr. Şahin Aktaş

ISTANBUL, 2017

MARMARA UNIVERSITY
INSTITUTE FOR GRADUATE STUDIES IN PURE AND APPLIED SCIENCES

Serdar GÖKÇE, a Master of Science student of Marmara University Institute for Graduate Studies in Pure and Applied Sciences, defended his thesis entitled "Magneto-Polymeric Microwave Composites and Their Application In Anechoic Chamber Paint", on January 25, 2017 and has been found to be satisfactory by the jury members.

Jury Members

Prof. Dr. Şahin AKTAŞ

Marmara University ....

Prof. Dr. Ziya Engin ERKMEN

Marmara Üniversitesi ....

Prof. Dr. Ahmet ALTINDAL

Yıldız Teknik Üniversitesi ....

APPROVAL

Marmara University Institute for Graduate Studies in Pure and Applied Sciences Executive Committee approves that Serdar GÖKÇE be granted the degree of Master of Science Department of Physics, Solid state Program on January 25, 2017.

Director of the Institute

Prof. Dr. Uğur Yahşi

ACKNOWLEDGEMENT

I would like to gratitude to my supervisor **Prof. Dr. Şahin Aktaş** for his motivation and valuable advices in my thesis.

I also would like to express my gratitude to **Doç. Dr. Mustafa Özdemir** who gave me M.R lecture and directed me doing this thesis.

I would like to thank **Prof. Dr. Bulat Rami** whom I took FMR lecture and had supplied me motivation and the necessary materials for research.

I am also thankful to research assistant **Maksut Maksutoğlu** for his significance advice and help to use laboratory devices.

I want to thank to TUBİTAK (project no: 113F158) for funding this research .

CONTENTS

ACKNOWLEDGEMENT…… iii

CONTENTS……. iv

ABSTRACT……. viii

ÖZET……..……. ix

SYMBOLS AND ABBREVIATIONS……. x

LIST OF FIGURES……..……. xi

LIST OF TABLES……..…….. xvi

CHAPTER 1

INTRODUCTION…… 1

CHAPTER 2

ELECTROMAGNETIC THEORY…….. 5

2.1 Maxwell Equations……. 5

2.2 The Wave Equation and Basic Plane Wave……..... 8

2.3 Electromagnetic Loss Mechanism……..…….....**.** 10

2.4 Boundary Conditions……...……..….. 14

2.5 Reflection and Transmission……... 16

2.5.1 Propagation Matrices…… 17

2.5.2 Matching Matrices……..... 22

2.5.3 Single Dielectric Slab……..…...…….. 27

2.6 Types of Microwave Absorbing……..…… 32

2.7 Anechoic Chamber……..…… 39

2.8 NRW Calculation and Reflection Loss…….……..…… 42

CHAPTER 3

EXPERIMENTAL AND CHARACTERIZATION…..…… 47

3.1 BaM Nanopowders Coated with PMMA……...……...…….. 48

3.1.1 XRD Analysis…….…… 48

3.1.2 SEM Analysis……..…….. 50

3.1.3 VSM Analysis……...……...…….. 51

3.1.4 FMR Results..……...……...…….. 54

3.1.5 Microwave Dielectric and Magnetic Properties…...……. 55

3.2 SrM Nanopowders Coated with PMMA……...…….. 59

3.2.1 XRD……...…….. 59

3.2.2 SEM Analysis…….....…….. 60

3.2.3 VSM Analysis……...…….…… 61

3.2.4 FMR Results..…….…….…….. 62

3.2.5 Microwave Dielectric and Magnetic Properties...……. 63

3.3 PbM Nanopowders Coated with PMMA……..…….. 66

3.3.1 XRD Analysis……..…….. 66

3.3.2 SEM Analysis……..…….. 68

3.3.3 VSM Analysis…….…….. 68

3.3.4 FMR Results..…….…….. 69

3.3.5 Microwave Dielectric and Magnetic Properties…….…….. 70

3.4 Micro-Sized Magnetic and Non-magnetic Powders..…… 73

3.4.1 Bulk Rectangular Samples……..…..…… 73

3.4.2 Rectangular Shaped Foam Sample……..…..…… 78

CHAPTER 4

PRODUCTION OF MICROWAVE ABSORPTION MATERIAL.…..…….. 83

4.1 Small Sample……... 83

4.2 Pyramidal Absorber…….…… 86

4.2.1 Conventional Design……..…… 86

4.2.2 New Design..…….. 87

4.3 NRL Arch Test Fixture and Measurement……...…… 88

CHAPTER 5

SIMULATION……..……..…….. 93

5.1 Small Sample……...…….…….…….. 94

5.1.1 Micro-Sized Rectangular Sample……. 94

5.1.2 Multilayer Absorber……...……..……. 98

5.1.3 Metamaterial Absorber…...……..……. 106

5.1.4 Multihole Absorber..……..…… 108

5.2 Pyramidal Absorber…….…….…….…….. 110

5.2.1 Single Pyramid……..…...…….…… 110

5.2.2 NRL Arch……...……...…… 113

CHAPTER 6

RESULTS AND DISCUSSION….……..……. 115

6.1 Toroidal Sample…….…..…….. 115

6.1.1 Carbonly Iron…… 115

6.1.2 Nickel……..…….……. 119

6.1.3 Carbon……..……..… 123

6.2 Pyramidal Absorbers……..……..……... 127

6.2.1 Conventional..……..…….…… 127

6.1.2 New Design……..……. 130

CONCLUSION…….…… 132

REFERENCES……..…… 134

APPENDIX…..……..…… 146

ÖZGEÇMİŞ……..……

ABSTRACT

MAGNETO-POLYMERIC MICROWAVE COMPOSITES AND THEIR APPLICATION IN ANECHOIC CHAMBER PAINT

In recent years, the rising demand for electronic devices in military, medical, telecommunication systems has resulted in the use of radar absorbing materials (RAM) to eliminate the electromagnetic interference. Especially, pyramidal microwave absorbers are utilized to provide production test of the electronic devices after fabricating. In this thesis, the nanoparticles together with PMMA polymer, micro-sized particles with different mixture and the pyramidal absorbers have been studied in order to enhance the RAM required for anechoic chamber design.

Barium ($BaFe_{12}O_{19}$), Strontium ($SrFe_{12}O_{19}$) and Lead ($PbFe_{12}O_{19}$) nano-hexaferrites which have have high magnetocrystalline anisotropy were synthesized by using the sol-gel method. Then, PMMA were mixed with these nanoparticles in a stoichiometric ratio of 20/80, 40/60, 60/40. These new materials were fabricated as toroidal shape. They were characterized by means of XRD, SEM, VSM and FMR analysis. The dielectric, magnetic properties and scattering parameter (S11, S21) of these composite samples were investigated in the frequency range between 2-18 GHz.

The micro-sized samples were produced as rectangular and toroidal shape. The dielectric permittivity, magnetic permeability, loss tangents, scattering parameter and microwave absorption rate of micro-sized particles were examined between 12.4-18 GHz. The reflection loss-RL analysis technique was applied on the result of toroidal shape micro-sized absorbers in the frequency range of 2 to 18 GHz.

The conventional and double type of microwave pyramidal absorbers based on micro-sized particle were designed and produced. The reflectivity values of them in P Band were measured with "*NRL Arch Test Fixture*" which is manufactured made of polyamide in this research. The micro-sized and nano-sized samples were simulated by using rectangular, circular waveguide technique to compare between simulation and measurement results. The multilayer absorbers composed of nano-hexaferrite were simulated by changing the thickness of their layer. The power loss density (PLD) of single pyramid was examined. As a result, the radar/microwave absorbing material which has absorption rate of %99 is improved.

ÖZET

MANYETO-POLİMERİK MİKRODALGA KOMPOZİTLER VE YANKISIZ ODA KAPLAMALARINDA UYGULAMALARI

Son zamanlarda, askeri, medical, telekomünikasyon sistemlere artan talep elektromanyetik girişimi azaltmak için radar soğurucu malzemelerin (RAM) kullanımına neden olmuştur. Özellikle, piramit yapılı mikrodalga soğurucu malzemelerden , elektronik aletlerin üretimi sonrası gereken testlerini gerçekleştirmek amacıyla faydalanılır. Bu tezde, yankısız oda kaplamasında gerekli RAM malzemeleri geliştirmek için, PMMA polimerli nanoparçacıklar, farklı karışımlara sahip mikroparçacıklar ve piramit soğurucular çalışılmıştır.

Yüksek manyetik kristal anizotropiye sahip Baryum ($BaFe_{12}O_{19}$), Stronsiyum ($SrFe_{12}O_{19}$) ve Kurşun ($PbFe_{12}O_{19}$) nanoparçacıkları sol-gel metodu kullanılarak sentezlendi. Daha sonra, bu parçacıklar 20/80, 40/60, 60/40 stokiyometrik oranlarda PMMA polimeri ile karıştırıldı. Bu yeni malzemeler toroidal şekillerde üretilmiştir. XRD, SEM, VSM ve FMR analizleri vasıtasıyla karakterizasyonu yapıldı. Bu kompozit malzemelerin dielektrik, manyetik özellikleri ve saçılma parametreleri (S11,S21) 2-18 GHz frekans aralığında incelendi.

Mikro boyutlu parçacıklar dikdörtgensel ve toroidal şekillerde üretildi. Bu numunelere ait dielektrik permitivite, manyetik permabilite, tanjant kayıpları, saçılma parametreleri ve mikrodalga soğurma oranları 12.4-18 GHz aralığında incelendi. Toroidal şekilli mikrodalga soğurucuların sonuçlarına 2-18 frekans aralığında yansıma kaybı-YK analiz tekniği uygulanmıştır.

Mikroparçacık temelli geleneksel ve duble mikrodalga piramit soğurucular tasarlandı ve üretildi. Bu araştırmada imal edilen "NRL yay test düzeneği" ile P bantta yansınabilirlik değerleri ölçüldü. Mikro ve nano yapılı parçacıkların simülasyon ve ölçüm değerlerini karşılaştırmak için dikdörtgensel ve dairesel dalga kılavuzu tekniği kullanılarak simülasyonları yapıldı. Nano hekzaferritten oluşan çok katmanlı soğurucuların simülasyonu katman kalınlıklarını değiştirerek yapıldı. Tek piramitlerin güç kayıp yoğunluğu incelendi. Sonuç olarak, %99 soğurma oranlarına sahip mikrodalga/radar soğurucu malzemeler geliştirildi.

SYMBOLS AND ABBREVIATIONS

EMI : Electromagnetic Interference

dB : decibel

FSS : Frequency Selective Surface

EMC : Electromagnetic Compatibility

RAM : Radar Absorbing Material

XRD: X-Ray Powder Diffraction Analysis

MAM : Microwave absorbing material

OATM : Open area test measurement

DUT : Device under test

AUT : Antenna under test

VNA : Vector Network Analyzer

VSM: Vibrating Sample Magnetometer

SEM: Scanning Electron Microscopy

FMR: Ferromagnetic Resonance

PNA: Phase Network Analyzer

PEC: Perfect Electric Conductor

TRL : Thru-Reflect-Line

NRL : Naval Research Laboratory

CST: Computer Simulation Technology

PMMA: Polymethyl methacrylate

LIST OF FIGURES

Figure 2.1. Parallel plate capacitor for illustration of electromagnetic loss in any dielectric layer **11**

Figure 2.2. Equivalent circuit of Inductor **13**

Figure 2.3. Loss tangent vector diagram **14**

Figure 2.4. Surface charge, tangential and normal fields at an interface between two media **15**

Figure 2.5. Forward and backward electric fields on material interface **17**

Figure 2.6. Uniform plane wave **17**

Figure 2.7. Field quantities propagated between two positions in space **21**

Figure 2.8. Field across an interface **23**

Figure 2.9. Single dielectric slab **28**

Figure 2.10. Graded dielectric absorbers by impedance matching **33**

Figure 2.11. Illustration of single pyramidal absorber **34**

Figure 2.12. Basic resonant absorber and their equivalent circuits **38**

Figure 2.13. Reflection performance of Jaumann absorber for different number of sheets **39**

Figure 2.14. Representation of typical anechoic chamber **40**

Figure 2.15. Representation of phase between spherical and plane wave **41**

Figure 2.16 Transmission line with the sample and three region **42**

Figure 3.1. Flow chart of sol-gel method for synthesizing barium hexaferrite **47**

Figure 3.2. XRD pattern of BaM hexaferrite with 20/40/60 PMMA ratios **48**

Figure 3.3. SEM images of samples prepared at different PMMA/BaM ratios **51**

Figure 3.4. Hysteresis loop of produced BaM hexaferrites at room temperature **52**

Figure 3.5. Plots of the saturation magnetization M_s, permenant magnetization M_r, coercive field H_c and squareness ratio M_r/M_s for each type hexaferrite samples **54**

Figure 3.6. FMR curves of BaM hexaferrite powders **55**

Figure 3.7. Dielectric permittivity (a) and magnetic permeability (b) curves of Ba1 . **56**

Figure 3.8. Dielectric permittivity (a) and magnetic permeability (b) curves of Ba2 . **56**

Figure 3.9. Dielectric permittivity (a) and magnetic permeability (b) curves of Ba3 . **57**

Figure 3.10. Scattering parameters S11, S21 for Ba1 (a) , Ba2 (b), Ba3 (c) in the frequency range between 2-18 GHz **58**
Figure 3.11. Reflection (R) and Transmission (T) coefficients for Ba1 (a) , Ba2 (b), Ba3 (c) in the range frequency range between 2-18 GHz **58**
Figure 3.12. XRD pattern of SrM hexaferrites with 20/40/60 PMMA ratios **59**
Figure 3.13. SEM images of samples prepared at different PMMA/SrM ratios **61**
Figure 3.14. Hysteresis loop of produced SrM hexaferrites at room temperature **62**
Figure 3.15. FMR curves of SrM Hexaferrite powders **63**
Figure 3.16. Complex dielectric permittivity and permeability including real and imaginary part. The permittivity (a) and permeability (b) for Sr1, permittivity (c) and permeability (d) for Sr2, permittivity (e) and permeability (f) for Sr3..... **64**
Figure 3.17. Scattering parameters S11, S21 for Sr1 (a), Sr2 (b), Sr3 (c) in the range frequency range between 2-18 GHz **65**
Figure 3.18. Reflection (R) and Transmission (T) coefficients for Sr1 (a), Sr2 (b), Sr3 (c) in the range frequency range between 2-18 GHz **66**
Figure 3.19. XRD pattern of PbM hexaferrites with 20/40/60 PMMA ratios **67**
Figure 3.20. SEM images of samples prepared at different PMMA/PbM ratios **68**
Figure 3.21. Hysteresis loop of produced PbM hexaferrites at room temperature **69**
Figure 3.22. FMR curves of PbM Hexaferrite powders **70**
Figure 3.23. Complex dielectric permittivity (a) and permeability (b) of Pb1 including real and imaginary part **71**
Figure 3.24. Complex dielectric permittivity (a) and permeability (b) of Pb2 including real and imaginary part **71**
Figure 3.25. Complex dielectric permittivity (a) and permeability (b) of Pb2..... **72**
Figure 3.26. Scattering parameters S11, S21 for Pb1 (a) , Pb2 (b), Pb3 (c) in the range frequency range between 2-18 GHz **72**
Figure 3.27. Reflection (R) and Transmission (T) coefficients for Pb1 (a) , Pb2 (b), Pb3 (c) in the range frequency range between 2-18 GHz **73**
Figure 3.28. Real part of permittivity and dielectric loss tangent of C, CFeNi, Fe, FeNi, Ni micropowder samples **74**

Figure 3.29. Real part of permeability and magnetic loss tangent of C, CFeNi, Fe, FeNi, Ni micropowder samples **75**
Figure 3.30. Scattering parameters S11 and S21 of C, Fe, Ni, FeNi and CFeNi samples **76**
Figure 3.31. Reflection (R) and Transmission (T) of C, Fe, Ni, FeNi and CFeNi samples **77**
Figure 3.32. Absorption (A) and Shielding Effectiveness (SE) of C, Fe, Ni, FeNi and CFeNi samples **77**
Figure 3.33. Real part of permittivity, permeability and dielectric loss tangent, magnetic loss tangent plots of rectangular shaped foam samples of C, Fe, Ni **79**
Figure 3.34. Scattering parameters S11,S21, reflection (R) and transmission (T) of C, Fe, Ni, FeNi and CFeNi foam samples **80**
Figure 3.35. Absorption (A) and Shielding Effectiveness (SE) of foam samples of C, Fe, Ni **81**
Figure 4.1. The manufactured rectangular small samples of C, Fe, Ni, FeNi, CFeNi **84**
Figure 4.2. Toroid small sample and its manufacturing tool **85**
Figure 4.3. Rectangular foam samples containin C,Ni and Fe micropowder **85**
Figure 4.4. Dimensions of conventional (a) and double design pyramid absorber (b) **86**
Figure 4.5. Appearance of pyramidal absorber before painting with anti-fire paint ..**87**
Figure 4.6. Appearance of pyramidal microwave absorbers after they have been painting with anti-fire paint **88**
Figure 4.7. Illustration of Arch measurement setup with pyramidal microwave absorber. **89**
Figure 4.8. Dimensions and Far-field distances of Arch measurement setup for X and P band **90**
Figure 4.9. New type Arch measurement setup operating at X, P, K and Ka band **91**
Figure 4.10. (a) The illustration of new design arch operating at 8.2-40 GHz and (b) its parts that are stick, disk, clamp and movable holder made of polyamid..**92**
Figure 5.1. New type Arch measurement setup operating at X, P, K and Ka band **93**
Figure 5.2. 12.4–18 GHz (P Band, WR62) measurement tool (a) and screenshot from

simulation (b).....**94**
Figure 5.3. Dimensions and perspective image of microwave absorbing sample simulated by using waveguide method.....**95**
Figure 5.4. Comparison of scattering parameter S11, S21 between simulation and measurement for Ni sample.....**96**
Figure 5.5. Comparison of scattering parameter S11, S21 between simulation and measurement for FeNi sample.....**97**
Figure 5.6. Comparison of scattering parameter S11, S21 between simulation and measurement for CFeNi sample **97**
Figure 5.7. Comparison of scattering parameter S11, S21 between simulation and measurement for Fe sample.....**98**
Figure 5.8. APC7 toroid measurement kit (a) with precision airline body (middle) and precision airline center conductor, toroid design in CST software (b), toroid design with waveguide ports 1,2 (c) **99**
Figure 5.9. Plot on the screen of network analyzer after the calibration for toroid measurement (a), pusher to insert easily the sample in the waveguide (b) **100**
Figure 5.10. Plot of permittivity of Ba1 sample and fitting line **101**
Figure 5.11. Comparision of scattering plots between measurement and simulation of (a) Ba1, (b) Sr1, (c) Pb1 and (d) Carbonly Iron (Fe).....**102**
Figure 5.12. Simulation design of multilayer absorber consisted of Ba1, Sr1, Pb1 and Fe layers.....**103**
Figure 5.13. S11 parameter versus frequency for multilayer absorber while (a) changing x ,constant y=0.15mm and (b) changing y, constant x=1.3mm **104**
Figure 5.14. Scattering parameter plots versus frequency of multilayer absorber for the case x=1.3mm and y=0.15mm.....**105**
Figure 5.15. Perspective view of metamaterial absorber in waveguide from CST Microwave software **106**
Figure 5.16. Simulation results (a) S11, (b) S21 of metametarial absorber for various codes of Fe, CFC, FFF, FFC, CEC, EEC and (c) their absorption plots **107**
Figure 5.17. Screen image of modeling multihole absorber and perspective view ...**109**

Figure 5.18. Microwave energy absorption curve for multihole absorber changing the radius of cone.....**110**
Figure 5.19. Power loss density (PLD), Simulation design and boundary conditions of single pyramid absorber based on Fe, Ni, C, Eccosorb and Teflon samples **111**
Figure 5.20. Power loss density (PLD), Simulation design and boundary conditions of single pyramid absorber for Ba1, C and Fe samples **112**
Figure 5.21. Modeling of reflectivity measurement setup in CST microwave studio**113**
Figure 5.22. (a) S21 parameter and (b) 3D field on two dimensional plane for the metal plate case.....**114**
Figure 6.1. (a) Scattering parameters and (b) dielectric/magnetic constants of toroidal Fe sample in the frequency range between 2-18 GHz **116**
Figure 6.2. (a) Absorption and (b) reflection loss of toroidal Fe sample. **117**
Figure 6.3. Reflection loss analysis graph for toroidal Fe sample. From top to bottom : reflection loss, matching thickness, loss tangent and matching impedance.....**118**
Figure 6.4. Contour graph of reflection loss for toroidal Fe sample **119**
Figure 6.5. (a) Scattering parameters and (b) dielectric/magnetic constants of toroidal Ni sample in the frequency range between 2-18 GHz.....**120**
Figure 6.6. (a) Absorption and (b) reflection loss of toroidal Ni sample **121**
Figure 6.7. Reflection loss analysis graph for toroidal Ni sample **122**
Figure 6.8. Contour graph of reflection loss for toroidal Ni sample **123**
Figure 6.9. (a) Scattering parameters and (b) dielectric/magnetic constants of toroidal C sample in the frequency range between 2-18 GHz **124**
Figure 6.10. (a) Absorption and (b) reflection loss of toroidal C sample **125**
Figure 6.11. Reflection loss analysis graph for toroidal C sample.....**126**
Figure 6.12. (a) Absolute impedance and (b) the contour graph of reflection loss for toroidal C sample.....**127**
Figure 6.13. Measurement of reflectivity of conventional type absorber **130**
Figure 6.14. Measurement of reflectivity of double type pyramidal absorber.....**131**

LIST OF TABLES

Table 2.1. Boundary equations for dielectric interface, electric and magnetic wall condition **16**

Table 3.1. 2θ values, (hkl) indices and calculated distance between planes obtained XRD profile for BaM hexaferrite powder **49**

Table 3.2. Calculated cell parameters and unit volume from the XRD profile **50**

Table 3.3. Calculated $H_c, M_s, M_r, M_r/M_s$ values for BaM,SrM and PbM Hexaferrites with different PMMA ratios **53**

Table 3.4. Material codes of synthesized hexaferrites and their PMMA ratios **53**

Table 3.5. 2θ values, (hkl) indices and the calculated distance between planes obtained XRD profile for SrM hexaferrite powders **60**

Table 3.6. 2θ values, (hkl) indices and the calculated distance between planes obtained XRD profile for PbM hexaferrite powders **67**

Table 3.7. Absorption rate in terms of percentage and the resonance frequency of PbM series **73**

Table 4.1. Content in weight ratio and particle size of carbonyl iron powder **83**

Table 4.2. Mixture ratio and codes of samples **84**

Table 5.1. Metametarial absorbers in various configuration with codes **107**

1. INTRODUCTION

RAM (Radar Absorbing Material) has been researched intensively due to have potential application in various field. RAM materials has been widely used in both civilian and military applications such as on ships, aircraft, anechoic chamber [1]. RAM materials have been developed recently using different kind of material [2-3]. Among of absorber materials, hexaferrites have attracted a lot of attention because of large magneto-crystalline anisotropy, high electrical resistivity and high saturation magnetization [4-7]. As hexaferrites are used permanent magnet, common application are magnetic recording media and microwave absorber. However they have been in use in electrical devices such as circulators [8], oscillators [9] and isolators [10].

There are various techniques to synthesize hexaferrite in the literature such as sol-gel method [11-17], co-precipitation [18-23], solid state reaction technique [24-26], hydrothermal synthesis [27-28], citrate precursor method [29-31], self-propagating combustion method [32-34] have been studied. In this study, hexaferrite nanoparticles were prepared by the sol-gel method together with PMMA (Polymethyl methacrylate) as the template due to the advantages of inexpensive precursor, a simple process, time saving and a resulting nano-sized powder [35]. Nanosize ferromagnetic materials have advantage than those of the bulk material [36].

There is a large volume of published studies to modify the magnetic and microwave parameters of barium [37-46] and strontium ferrite [47-56] based on substitutions. Hexagonal ferrites have the formula $MFe_{12}O_{19}$ where "M" symbol is usually Ba and Sr. This type hexaferrites have larger coercive field and high saturation magnetization which Ba [57] and Sr [58] type hexaferrite has reported as 72 emu/g and 74.3 emu/g respectively.

The investigation of electromagnetic wave absorber started in the 1930's [59]. The first patent that was quarter-wave resonant type absorber developed in 1936 in the Netherlands [60]. At this absorber, carbon as a lossy resistive material and Titanium dioxide for its high permittivity to reduce the thickness were used [61]. Two types of material (MacFarlane 1945; Schade 1945) were successfully developed in Germany for

use in submarines. The first is called “Wesch” material consisted of a semiflexible rubber sheet loaded with carbonyl iron powder which had resonant around 3 Ghz. The second material, Jaumann Absorber was produced by a multilayer approach. It was evaluated by alternating resistive sheets that the distance between sheets consistent with quarter wavelength condition (measured at the center frequency of the absorption band) for a larger bandwidth [62]. This absorber provides the reflectivity of -20dB over 2-15 GHz at the normal incidence. In the US, the material known as HARP (Halpern-anti-radar-paint) was developed during the same time, which achieved 15-20 dB reduction in reflectivity at resonance frequency.

A well-known absorber developed during this period was the Salisbury Screen (Salisbury 1952). A resistive sheet placed at quarter wavelength ($\lambda/4$) from the metal plate, was spaced by a low dielectric material. Salisbury Screens operate by resonant technique and were widely used in earlier anechoic chamber designs. Yet another resonant absorber in wide use, was the Dallenbach Layer (Ruck et al 1970). It consisted of a homogeneous lossy layer on a metal plate. The thickness of the lossy layer was selected so as to match its input impedance with the intrinsic impedance of the free space [63].

The microwave absorber can be used to minimize the electromagnetic reflection from the metal plate such as aircrafts, ships, tanks and the walls of anechoic chambers and electronic equipment [64-66]. A good microwave absorber must have the high absorbance and low reflectance in the same frequency range. For the purpose of preparing a low-reflecting absorber in the desired frequency range, two fundamental conditions must be satisfied [67], the first is that the incident wave can enter the absorber by the greatest extent (impedance matching characteristic). The second is that the electromagnetic wave entering into the materials can be almost entirely attenuated and absorbed within the finite thickness of the absorber (attenuation characteristic) [68]. The reflection of incident wave on the interface is proportional to the magnitude of the impedance between free space and transmitting media. When the surface input impedance of the material is achieved to be equal that of free space, the zero reflection is obtained for such structure. Accordingly, three kinds of absorber have been developed such as pyramidal, tapered and matching [69]. Moreover perfect impedance matching can also be realized as the electric permittivity and the magnetic permeability are the

same [62]. However the existence of perfect matching impedance is an ideal condition so that cannot be achieved actually. The important thing is that investigate the material whose impedance close to the matching condition. There is is no finalized design law for the matching of the parameters in the material design yet [70-74].

The dielectric and/or magnetic losses have an important role in the manufacture of microwave absorbing materials when the electromagnetic wave impinged it. To develop microwave absorbing materials with high efficiency, many studies have been carried out [75-81]. The properties of microwave absorber such as loss factor, impedance, dielectric and magnetic parameter can be evaluated by controlling thickness and material type from narrow to broad frequency band [82]. For an absorber, the absorption properties are determined by its complex permeability μ_r, permittivity ε_r, and thickness. To get strong reflection loss peak, the value of μ_r/ε_r is great importance for the impedance matching [83]. However, we know from the publications on the microwave absorbers that the dielectric permittivity is usually much larger than the permeability. So the high μ_r/ε_r is not desired because only a small part of electromagnetic wave can enter the microwave absorber [84-85]. For enhancing the entered EMW in the absorber, many studies are published that the strong reflection loss can be achieved by mixing the magnetic ferrite particle with relatively low permittivity [86-88].

The microwave absorbers are widely used in the building of anechoic chamber. It was originally discovered to realize the manufacturing test of aircraft during the Second World War [89]. Anechoic chamber is a shielded room designed to absorb the undesired electromagnetic waves inside the chamber and eliminate the signal and noise from outside the chamber. It simulates OATM (Open Area Test Measurement) which is needed to perform EMC (Electromagnetic Compatibility) measurement for testing emissions and immunity. It is mainly consisted of an antenna system and microwave absorber materials mounted on the walls. Ideal anechoic chamber that can be considered as it absorbs all reflections from object and the shield surrounding the chamber obstruct all incoming signal can simulate free space medium. Any anechoic chamber is designed to realize the measurement of EMC and radar cross section. There is many different design of anechoic chamber which is basically constructed for performing EMC testing involving applications such as military, medical, telecommunication, automotive, aerospace and consumer electronics [90].

The operating frequency range and absorption level of anechoic chamber need to be above a certain limit to meet measurement standards. In order to anechoic chamber satisfy the international standards of EMC measurement, the absorbers must have the absorption characteristics higher than 20dB in the frequency range from 30 MHz to 18 GHz [91].

The performance of the absorber in an anechoic chamber is most important to eliminate the reflected signals. The absorbers for anechoic chamber to realize broad and strong absorption can be produced impregnating conductive carbon into a polyurethane or polystyrene foam. Then these materials are formed to various shapes to obtain impedance matching between absorber surface and free space. The absorption of energy over the frequency band from microwave to 500 MHz can be adjustable by changing the carbon content and the tapered shaped in the absorber whose length should be greater than one wavelength [92]. For strong absorption, one of the main parameter is absorber shape that affects the performance of microwave absorbers. Many type of shape exist in the market, such as pyramid, wedge, walkway, convoluted, and oblique absorber. Among these, pyramidal shape absorbers are typically large materials whose pyramid or cone structures extend perpendicular to the surface in a regularly spaced pattern [93-96]. In order to provide a gradual transition as impedance from free space to the absorber, pyramidal absorbers were improved. The size of the pyramid structure affects the change in the impedance which is critical parameter to good absorption. For example, the pyramidal absorber manufactured with pyramids many wavelength thick maintained the absorption level greater than 50 dB [90]. This great performance results primarily from the multiple reflections that occur between the pyramids (Appendix A). The incident electromagnetic wave is absorbed gradually by the side of the pyramid due to many reflections [97]. However, the pyramidal absorbers are thick and fragile with respect to the flat absorbers.

Another type of absorber is tapered loading absorber which is typically a slab composed of a low loss material mixed with a lossy material. The lossy particles is gradually dispersed into the material to provide matching impedance with tapering towards the inside of the material [98-99]. One of disadvantage of these absorbers is to have poor performance respect to pyramidal absorbers. However, they are thinner than the others.

2. ELECTROMAGNETIC THEORY

2.1. Maxwell Equations

Electromagnetic fields at the macroscopic level can be generally described by Maxwell's equations:

$$\nabla.E = \frac{\rho}{\varepsilon_0} \qquad \text{Gauss Law} \qquad (2.1a)$$

$$\nabla.\vec{B} = 0 \qquad (2.1b)$$

$$\nabla x\vec{E} = -\frac{\partial \vec{B}}{\partial t} \qquad \text{Faraday Law} \qquad (2.1c)$$

$$\nabla x\vec{B} = \mu_0 \vec{J} + \mu_0 \varepsilon_0 \frac{\partial \vec{E}}{\partial t} \qquad \text{Ampere's Law} \qquad (2.1d)$$

where $\vec{E}$ is the electric field strength vector (V/m), $\vec{B}$ is the magnetic flux density vector (Wb/m^2 or Tesla). The sources of the electromagnetic field are the electric current density vector $\vec{J}$ (A/m^2) and the electric charge density ρ ($Coul/m^3$) [100]. In free space or away from sources, the electric charge density ρ and the electric current density $\vec{J}$ equals zero. So the Maxwell equations take the simpler form:

$$\nabla.\vec{E} = 0$$

$$\nabla.\vec{B} = 0$$

$$\nabla x\vec{E} = -\frac{\partial \vec{B}}{\partial t} \qquad \text{Source - free Maxwell's equations} \qquad (2.2)$$

$$\nabla x\vec{B} = \mu_0 \varepsilon_0 \frac{\partial \vec{E}}{\partial t}$$

For a dielectric material, an applied electric field $\vec{E}$ produce additional polarization vector ($\vec{P}$). This polarization vector is called the electric polarization. In the similar way, for magnetic materials, an applied magnetic field $\vec{H}$ creates magnetic dipole moments ($\vec{M}$). This polarization is called the magnetic polarization. Therefore, the electric polarization and magnetic polarization are related to bound charge density ($\rho_b = -\nabla.\vec{P}$) and bound current density ($J_b = \nabla x\vec{M}$), respectively. Total charge density is defined as,

$$\rho = \rho_f + \rho_b$$
$$\rho = \rho_f - \nabla\vec{P} \qquad \text{surface charge} \qquad (2.3)$$

Substituting this expression into the Gauss law (2.1a) gives

$$\nabla.\vec{E} = \frac{\rho_f - \nabla\vec{P}}{\varepsilon_0}$$

$$\varepsilon_0\nabla.\vec{E} + \nabla\vec{P} = \rho_f$$

$$\nabla.(\varepsilon_0\vec{E} + \vec{P}) = \rho_f \qquad (2.4)$$

$$\nabla.\vec{D} = \rho_f$$

$$\vec{D} = \varepsilon_0\vec{E} + \vec{P}$$

where $\vec{D}$ is the electric displacement vector or the electric current density. Total current density is defined as,

$$\vec{J} = \vec{J}_f + \vec{J}_b + \vec{J}_P \qquad (2.5)$$

$$\vec{J} = \vec{J}_f + \vec{\nabla}x\vec{M} + \frac{\partial\vec{P}}{\partial t}$$

Substituting this expression into the Ampere law (2.1d) gives

$$\nabla x\vec{B} = \mu_0(\vec{J}_f + \nabla x\vec{M} + \frac{\partial \vec{P}}{\partial t}) + \mu_0\varepsilon_0\frac{\partial \vec{E}}{\partial t}$$

$$\nabla x(\frac{\vec{B}}{\mu_0} - \vec{M}) = \vec{J}_f + \frac{\partial}{\partial t}(\varepsilon_0\vec{E} + \vec{P}) \qquad (2.6)$$

$$\vec{H} = \frac{1}{\mu_0}\vec{B} - \vec{M}$$

$$\nabla x\vec{H} = \vec{J}_f + \frac{\partial \vec{D}}{\partial t}$$

In this case, the maxwell's equations in media can be rewritten in terms of free charges and currents,

$$\nabla.\vec{D} = \rho_f \qquad (2.7a)$$

$$\nabla.\vec{B} = 0 \qquad (2.7b)$$

$$\nabla x\vec{E} = -\frac{\partial \vec{B}}{\partial t} \qquad \text{Maxwell's equations in a medium} \qquad (2.7c)$$

$$\nabla x\vec{H} = \vec{J}_f + \frac{\partial \vec{D}}{\partial t} \qquad (2.7d)$$

Where the electric and magnetic flux densities $\vec{D}$, $\vec{B}$ are related to the field intensity $\vec{E}$, $\vec{H}$. These relationships between flux density and field strength are called "constitutive relations". These are for simple dielectric and magnetic materials (σ is conductivity of material:

$$\vec{D} = \varepsilon\vec{E}$$

$$\vec{B} = \mu\vec{H} \qquad (2.8)$$

$$\vec{J} = \sigma\vec{E}$$

2.2. The Wave Equation and Basic Plane Wave

In order to get electromagnetic wave equation, we are going to use the Maxwell's equations again. Electric and magnetic field can be considered the time dependence function.

$$\begin{aligned}\vec{E} &= E(x,y,z)e^{j\omega t} \\ \vec{H} &= H(x,y,z)e^{j\omega t}\end{aligned} \tag{2.9}$$

So assuming an e^{jwt} time dependence, we can replace the time derivatives in (2.2) with " $j\omega$ ". This converts Maxwell's equation in phasor form:

$$\nabla x E = -j\omega\mu H \tag{2.10a}$$

$$\nabla x H = j\omega\varepsilon E \tag{2.10b}$$

E and H can be solved using curl rule[1]. If we apply the cirl rule on the equation of 2.10a and 2.10b, the wave equation or "Helmholtz Equation" can be derived.

$$\begin{aligned}\nabla x \nabla x E &= \nabla x(-j\omega\mu H) \\ \nabla(\nabla.E) - \nabla^2 E &= -j\omega\mu(\nabla x H) \\ -\nabla^2 E &= \omega^2\mu\varepsilon E \\ \nabla^2 E + \omega^2\mu\varepsilon E &= 0\end{aligned} \tag{2.11}$$

and similarly,

[1] $\nabla x \nabla x \vec{A} = \nabla(\nabla.\vec{A}) - \nabla^2 \vec{A}$

$$\nabla x\nabla xH = \nabla x(-j\omega\varepsilon E)$$

$$\nabla(\nabla.H) - \nabla^2 H = -j\omega\varepsilon(\nabla xE) \qquad (2.12)$$

$$-\nabla^2 H = \omega^2\mu\varepsilon H$$

$$\nabla^2 H + \omega^2\mu\varepsilon H = 0$$

In the wave equation, the quantity of $\omega^2\mu\varepsilon = k^2$. Constant $k = \omega\sqrt{\mu\varepsilon}$ is called the propagation constant (also known as the phase constant, or wave number) of the medium. So the wave equations can be written as the following expression,

$$k = \omega\sqrt{\mu\varepsilon} \qquad (2.13a)$$

$$\nabla^2 E + k^2 E = 0 \qquad \text{Helmholtz Equations} \qquad (2.13b)$$

$$\nabla^2 H + k^2 H = 0 \qquad (2.13c)$$

If the medium is conductive with a conductivity σ, a conduction current density $\vec{J} = \sigma\vec{E}$ will exist. Thus Maxwell's curl equations (2.7c and 2.7d) transforms into:

$$\nabla xE = -j\omega\mu H \qquad (2.14a)$$

$$\nabla xH = j\omega\varepsilon E + \sigma E = (\sigma + j\omega\varepsilon)E \qquad (2.14b)$$

The resulting wave equation (2.11) for $\vec{E}$ then becomes

$$\nabla^2\vec{E} + \omega^2\mu\varepsilon\left(1 - j\frac{\sigma}{\omega\varepsilon}\right)\vec{E} = 0 \qquad (2.15)$$

$$\nabla^2\vec{E} - \gamma^2\vec{E} = 0$$

When we compare this equation with the wave equation for $\vec{E}$ in the lossless case (2.11), we can see a similarity. The difference between two equations is replacing with the term of $\omega^2\mu\varepsilon$ by $-\gamma^2 = \omega^2\mu\left[\varepsilon - j(\sigma/\omega)\right]$ in (2.15). So we got complex dielectric constant (ε_c).

$$\varepsilon_c = \varepsilon - j\frac{\sigma}{\omega} \tag{2.16}$$

Then "complex propagation constant" is defined for the medium as

$$\gamma = \alpha + j\beta = j\omega\sqrt{\mu\varepsilon}\sqrt{1 - j\frac{\sigma}{\omega\varepsilon}} \tag{2.17}$$

where α is the "attenuation constant" and β is the "phase constant". In the case of $\sigma = 0$, equation (2.17) reduces to

$$\gamma = j\omega\sqrt{\mu\varepsilon} = jk = j\omega\sqrt{\mu\varepsilon'(1 - j\tan\delta)} \tag{2.18}$$

Where $\tan\delta = \varepsilon''/\varepsilon'$ is the loss tangent of the material. $\beta = 2\pi/\lambda$ is the phase change, and λ is the operating wavelength in the medium. We may rearrange complex propagation constant for high conductivity material in the case of $\sigma >> \omega\varepsilon$, which means that the conducting current is much larger than the displacement current.

$$\gamma = \alpha + j\beta = j\omega\sqrt{\mu\varepsilon}\sqrt{\frac{\sigma}{j\omega\varepsilon}} = (1 + j)\sqrt{\frac{\omega\mu\sigma}{2}} \tag{2.19}$$

The power attenuation can be expressed as "skin depth" or "penetration depth". The skin depth means decaying field by an amount e^{-1} in a distance of a skin depth of δ_s. At the high frequency or for a good conductor (metal), the skin depth is a very small distance. Because it depends inversely on the frequency (ω) and conductivity (σ). It is defined as the inverse of attenuation constant of α [101-102]:

$$\delta_s = \frac{1}{\alpha} = \sqrt{\frac{2}{\omega\mu\sigma}} \qquad \text{(skin depth)} \tag{2.20}$$

2.3. Electromagnetic Loss Mechanism

When an external field is applied any material If it has the ability to store energy, this kind of material is classified as "dielectric". We can consider any parallel plate capacitor as an example. From the Figure 2.1.a, we have a DC voltage source, parallel plate and dielectric material between two plates. If any dielectric layer is placed

between plates, more charge will be stored. When no material is between two plates, much less charge is stored than the case that a dielectric material exist.

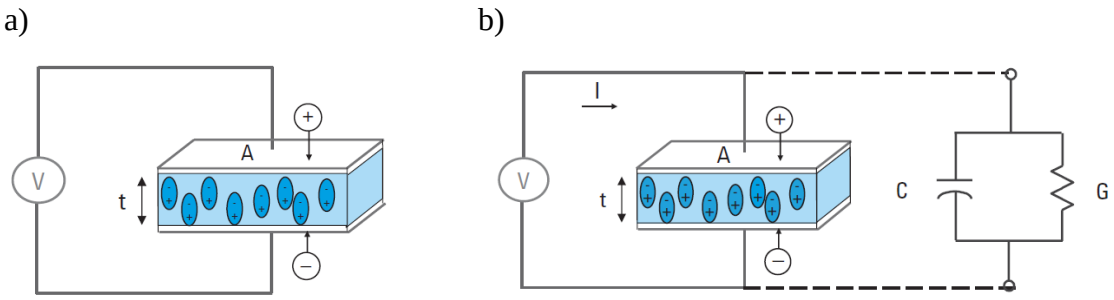


Figure 2.1. Parallel plate capacitor for illustration of electromagnetic loss in any dielectric layer, (a) DC case and (b) AC case

The capacitance of the capacitor depends on the dielectric constant:

$$C_0 = \varepsilon_0 \frac{A}{t} \qquad \varepsilon_r^{'} = \frac{C}{C_0} \tag{2.21}$$

Where C and C_0 are capacitance with and without dielectric, "t" is the distance between plates and "A" is the area of the capacitor. Dielectric material provides to storage much charge between parallel plates. In the DC voltage case, the dielectric constant $\varepsilon_r^{'}$ is real. If we consider that AC voltage is applied to the circuit, it will cause loss current. In this case, current can be separated into two parts (Equation 2.23): I_c charging current and I_l loss current. The losses in the material can be represented as a conductance G which is shown in parallel with a capacitor in Figure 2.1.b

$$Z_c = \frac{1}{j\omega C} \qquad Z_l = \frac{1}{G} \tag{2.22}$$

$$I = I_c + I_l = \frac{V}{Z_c} + \frac{V}{Z_l} = V\left(j\omega C + G\right) \tag{2.23}$$

where $G = \omega C_0 \varepsilon_r^{"}$. To represent dielectric constant $\varepsilon_r^{"}$, the double prime notation is used because of loss characteristic.

$$I = V(j\omega C_0 \varepsilon_r^{'} + \omega C_0 \varepsilon_r^{"}) = V(j\omega C_0)\left[\varepsilon_r^{'} - j\varepsilon_r^{"}\right] \qquad (2.24)$$

Therefore, the complex dielectric constant is also called "permittivity". It consists of a real part and imaginary part which is shown below in equation 2.25. Permittivity describes the interaction of a material with an electric field. The real part of permittivity ($\varepsilon_r^{'}$) is a measure of how much energy from an external electric field is stored in a material. The imaginary part of permittivity ($\varepsilon_r^{"}$) is a measure of how dissipate energy of an external electric field into heat. Thus we can say that an electric field interacts with a material in two ways, "storage" and "loss". So in the storage situation, energy may be exchanged between the field and the material. In the loss situation, energy may be permanently lost from the field, and absorbed as heat in the material.

$$\varepsilon = \varepsilon_0 \varepsilon_r = \varepsilon_0 (\varepsilon_r^{'} - j\varepsilon_r^{"}) \qquad (2.25)$$

ε_r is the relative permittivity that is the absolute permittivity (ε) relative to the permittivity of free space ($\varepsilon_0 = 8.854x10^{-12}$ F/m). Permeability describes the interaction of a material with magnetic field applied on it. For permeability similar analysis can be performed which is shown in Figure 2.2. If any core is placed in the coil, more current will be induced by inductor. So the inductance depends on the permeability of the material. The symbol of L represents the inductance with the core material, L_0 is free space inductance of the coil. The relationship between L and L_0 gives

$$\mu_r^{'} = \frac{L}{L_0} \qquad (2.26)$$

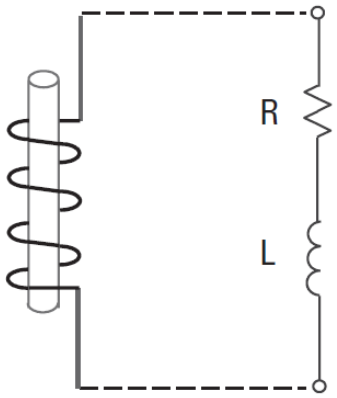


Figure 2.2. The equivalent circuit of Inductor

If AC current source is applied to the circuit, the resulting voltage will be made up of an induced voltage and a loss voltage. Therefore permeability can be expressed complex permeability. It consist of a real part ($\mu_r^{'}$) that represents the magnetic energy storage term and imaginary part ($\mu_r^{"}$) that represents the magnetic energy loss term. Relative permeability (μ_r) is the absolute permittivity (μ) relative to the permeability of free space ($\mu_0 = 4\pi x10^{-7}$ H/m).

$$\mu = \mu_0\mu_r = \mu_0(\mu_r^{'} - j\mu_r^{"}) \tag{2.27}$$

At microwave frequencies, energy loss may occur associated with the dispersion of $\varepsilon^{'}$, $\mu^{'}$ and an actual conductivity caused by migrating charge carriers [103-104]. The loss tangent ($\tan\delta$) is defined as the ratio of the imaginary part of the permittivity or permeability to the real part. Besides the loss tangent, another parameter as quality factor is often used to describe an electromagnetic material:

$$\tan\delta_e = \frac{\varepsilon_r^{"}}{\varepsilon_r^{'}} \qquad Q_e = \frac{1}{\tan\delta_e}$$
$$\tan\delta_m = \frac{\mu_r^{"}}{\mu_r^{'}} \qquad Q_m = \frac{1}{\tan\delta_m} \tag{2.28}$$

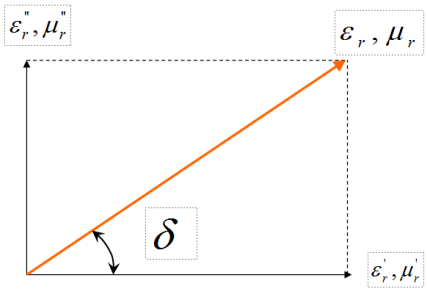


Figure 2.3. Loss tangent vector diagram

On the basis of the dielectric quality factor Q_e and magnetic quality factor Q_m , we can get the total quality factor Q of the material:

$$\frac{1}{Q} = \frac{1}{Q_e} + \frac{1}{Q_m} \tag{2.29}$$

2.4. Boundary Conditions

Consider electromagnetic fields across material boundaries (Figure 2.4). This field must satisfy boundary conditions at the interface between the two media. In order to show fields at this interface, Maxwell's equation in integral form is used. So Maxwell equation's (2.7) can also be written in the integral form as

$$\begin{aligned}
&\oiint_S \vec{D}\, d\vec{s} = \int_v \rho\, dv = Q \\
&\oiint_S \vec{B}.\, d\vec{s} = 0 \\
&\oint_C \vec{E}.\, \mathrm{d}\vec{l} = -\frac{\partial}{\partial t} \oiint_S \vec{B}.\, \mathrm{d}\vec{s} \\
&\oint_C \vec{H}.\, d\vec{l} = \oiint_S (J + \frac{\partial \vec{D}}{\partial t}).\mathrm{d}\vec{s}
\end{aligned} \tag{2.30}$$

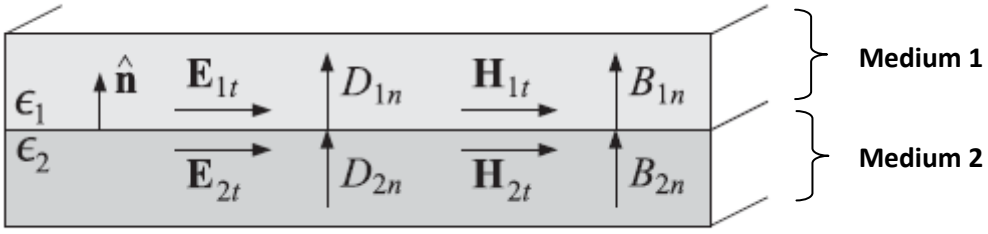


Figure 2.4. Surface charge, tangential and normal fields at an interface between two media [96]

When we apply Maxwell's equations in integral form to the boundary between medium 1 and medium 2 shown in Figure 2.4., we get:

$$\begin{aligned} n.(\vec{D}_1 - \vec{D}_2) &= \rho_s \\ n.(\vec{B}_1 - \vec{B}_2) &= 0 \\ n \text{ x } (\vec{E}_1 - \vec{E}_2) &= 0 \\ n \text{ x } (\vec{H}_1 - \vec{H}_2) &= \vec{J}_s \end{aligned} \tag{2.31}$$

Where n is the normal unit vector pointing out of the surface. As before, surface charge was mentioned in equation (2.3). In that equation, total charge current density was divided into two parts as free and bound current charge density. However, where the quantities ρ_s, J_s are any external surface charge and surface current densities on the boundary surface. Above equations reveal the state of fields at the boundary between two distinct media. We can express with words: the difference of the normal components of the electric flux density $\vec{D}$ are equal to the surface charge density. The difference of the normal components of the magnetic flux density $\vec{B}$ is continuous. The difference of the tangential components of the $\vec{H}$ field is equal to the surface current density. The difference of the tangential components of the $\vec{E}$ field is continuous across the interface [96].

Besides, boundary equations can be extracted from equation (2.31) for dielectric, perfect conductor and magnetic wall states. Table 2.1 shows the difference of the normal and

tangential components of fields and fluxes for three conditions. We know that there will be no charge or surface current density at the interface for an ordinary two dielectric material. Therefore, If we eliminate ρ_s and J_s terms in the above equations, we can find that normal components of $\vec{D}$, $\vec{B}$ and tangential components of $\vec{E}$, $\vec{H}$ are continuous across the interface. Consider a good conductor (metal), surface and charge current density must be taken into account in these boundary equations. Such materials are assumed as lossy which means that electric and magnetic field components will be attenuated by material. In the perfect conductor, while conductivity goes to infinity ($\sigma \to \infty$), we see that skin depth goes to zero at the equation 2.20. Thus, all field components will be zero inside the conducting region and will not penetrate through the material. So the electric field on one side is taken as zero at the above equations. Such a boundary is also known as an "electric wall" because the tangential components of $\vec{E}$ are "shorted out" and must vanish at the surface of the conductor. In the case of magnetic wall we have similar analogy with the electric wall, where the tangential components of $\vec{H}$ will vanish [98].

Table 2.1. Boundary equations for dielectric interface, electric and magnetic wall condition

Dielectric Interface	Perfect Conductor (Electric Wall)	Magnetic Wall
$\vec{D}_{1n} = \vec{D}_{2n}$	$n.\vec{D} = \rho_s$	$n.\vec{D} = \rho_s$
$\vec{B}_{1n} = \vec{B}_{2n}$	$n.\vec{B} = 0$	$n.\vec{B} = 0$
$\vec{E}_{1t} = \vec{E}_{2t}$	$n \times \vec{E} = 0$	$n \times \vec{E} = -\vec{M}_s$
$\vec{H}_{1t} = \vec{H}_{2t}$	$n \times \vec{H} = \vec{J}_s$	$n \times \vec{H} = 0$

2.5. REFLECTION AND TRANSMISSION

To analyze the reflection and transmission coefficients of the any single dielectric slab, we have to begin with propagation and matching matrices.

2.5.1. Propagation Matrices

We will consider uniform plane waves that moves normally on material interfaces. We separate the electric fields into two parts. While one part goes forwards, the other part goes backwards (Figure 2.5). It is linearly polarized in the x-direction and propagating along the z-direction in a lossless (homogeneous and isotropic) dielectric.

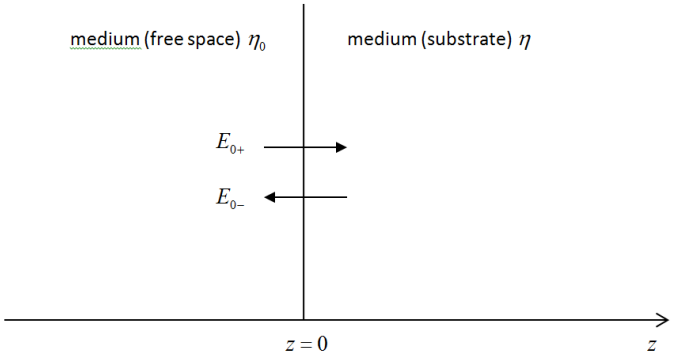


Figure 2.5. Forward and backward fields on material interface

$$E_+(z) = E_{0+}e^{-jkz} \qquad (forward)$$
$$E_-(z) = E_{0-}e^{+jkz} \qquad (backward) \tag{2.32}$$

To define the magnetic field, right-handed orthogonal system is used. The magnetic field $\vec{H}$ is perpendicular to the electric field $\vec{E}$ and the cross-product $\vec{E}x\vec{H}$ points towards the direction of propagation. Figure 2.6 depicts forward propagating wave.

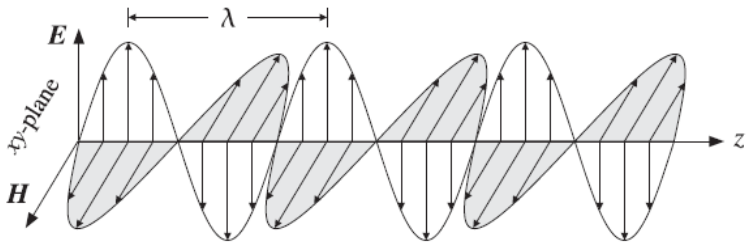


Figure 2.6. Uniform plane wave

So we can define the constant amplitude of magnetic fields:

$$\vec{H}_{0\pm} = \pm \frac{1}{\eta_0} \hat{z} \; x \; \vec{E}_{0\pm} \tag{2.33}$$

Where η_0 is the wave impedance of free space. It is effectively given by

$$\eta_0 = \frac{E_0}{H_0} = \sqrt{\frac{\mu_0}{\varepsilon_0}} \approx 377 ohms \tag{2.34}$$

We obtain total electric expressed as a superposition of forward and backward components. And we have total magnetic field using equation (2.33).

$$\begin{aligned} E(z) &= E_{0+} e^{-jkz} + E_{0-} e^{+jkz} = E_+(z) + E_-(z) \\ H(z) &= H_{0+} e^{-jkz} + H_{0-} e^{+jkz} = \frac{1}{\eta_0}[E_{0+} e^{-jkz} - E_{0-} e^{+jkz}] = \frac{1}{\eta_0}[E_+(z) - E_-(z)] \end{aligned} \tag{2.35}$$

$E_{\pm}(z)$ can be expressed in terms of $E(z)$, $H(z)$ by adding and subtracting the two equations (2.35):

$$\begin{aligned} E_+(z) &= \frac{1}{2}\left[E(z) + \eta_0 H(z)\right] \\ E_-(z) &= \frac{1}{2}\left[E(z) - \eta_0 H(z)\right] \end{aligned} \tag{2.36}$$

Total electric and magnetic field can also be written in terms of forward and backward fields in the matrix form (2.35):

$$\begin{bmatrix} E \\ H \end{bmatrix} = \begin{bmatrix} 1 & 1 \\ \eta_0^{-1} & -\eta_0^{-1} \end{bmatrix} \begin{bmatrix} E_+ \\ E_- \end{bmatrix} \tag{2.37}$$

In the same way, the forward and backward fields also can be written in terms of total fields in the matrix form (2.36)

$$\begin{bmatrix} E_+ \\ E_- \end{bmatrix} = \frac{1}{2} \begin{bmatrix} 1 & \eta_0 \\ 1 & -\eta_0 \end{bmatrix} \begin{bmatrix} E \\ H \end{bmatrix} \tag{2.38}$$

The ratio of electric and magnetic field in a medium is called "*characteristic wave impedance*" or "*intrinsic impedance*" of medium.

$$Z = \frac{E}{H} = \sqrt{\frac{\mu}{\varepsilon}} \qquad \text{wave impedance} \qquad (2.39)$$

And the reflection coefficient at position z is represented as,

$$\Gamma(z) = \frac{E_{-}(z)}{E_{+}(z)} \qquad \text{reflection coefficient} \qquad (2.40)$$

Using equation (2.36) and (2.40), we find:

$$\Gamma(z) = \frac{E_{-}(z)}{E_{+}(z)} = \frac{\frac{1}{2}(E(z) - \eta_0 H(z))}{\frac{1}{2}(E(z) + \eta_0 H(z))} = \frac{\frac{E(z)}{H(z)} - \eta_0}{\frac{E(z)}{H(z)} + \eta_0} = \frac{Z(z) - \eta_0}{Z(z) + \eta_0} \qquad (2.41)$$

Similarly, using equation (2.35) and (2.40), we have:

$$\mathrm{Z} = \frac{E}{H} = \frac{E_{+}(z) + E_{-}(z)}{\frac{1}{\eta_0}[E_{+}(z) - E_{-}(z)]} = \eta_0 \frac{1 + \frac{E_{-}(z)}{E_{+}(z)}}{1 - \frac{E_{-}(z)}{E_{+}(z)}} = \eta_0 \frac{1 + \Gamma(z)}{1 - \Gamma(z)} \qquad (2.42)$$

If we define $\Gamma(0) = \frac{E_{0-}}{E_{0+}}$ at z=0, $\Gamma(z)$ can be expressed in terms of $\Gamma(0)$:

$$\Gamma(z) = \frac{E_{-}(z)}{E_{+}(z)} = \frac{E_{0-} e^{+jkz}}{E_{0+} e^{-jkz}} = \Gamma(0) e^{2jkz} \qquad \text{propagation of } \Gamma \qquad (2.43)$$

Equation (2.42) may be solved for $Z(z)$ in terms of $Z(0)$ using equation (2.43):

$$\mathrm{Z(z)} = \eta_0 \frac{1 + \Gamma(z)}{1 - \Gamma(z)} = \eta_0 \frac{1 + \Gamma(0) e^{2jkz}}{1 - \Gamma(0) e^{2jkz}} = \eta_0 \frac{1 + \frac{Z(0) - \eta_0}{Z(0) + \eta_0} e^{2jkz}}{1 - \frac{Z(0) - \eta_0}{Z(0) + \eta_0} e^{2jkz}} \qquad (2.44)$$

$$Z(z)=\eta_0 \frac{(Z(0)+\eta_0)e^{-jkz}+(Z(0)-\eta_0)e^{jkz}}{(Z(0)+\eta_0)e^{-jkz}-(Z(0)-\eta_0)e^{jkz}} = \eta_0 \frac{Z(0)\cos kjz - j\eta_0 \sin kjz}{\eta_0 \cos kjz - jZ(0)\sin kjz} \qquad (2.45)$$

$$Z(z) = \eta_0 \frac{Z(0) - j\eta_0 \tan kjz}{\eta_0 - jZ(0)\tan kjz} \qquad \text{propagation of Z} \qquad (2.46)$$

Reflection coefficient and propagation of impedance have been shown for two medium which have different impedance. However electric-magnetic field, reflection coefficient and impedance should be analyzed at the two locations. Figure 2.7 depicts the quantities $E(z), H(z), E_+(z), E_-(z), Z(z), \Gamma(z)$ for one medium at two points z_1 and z_2 separated by a distance ($l = z_2 - z_1$). The impedance Z_2 at the point z_2 and other factors can affect the impedance Z_1 at the point z_1. Using equation (2.32), we have for the forward field at these two positions:

$$\begin{aligned} E_{2+} &= E_{0+}e^{-jkz_2} \\ E_{1+} &= E_{0+}e^{-jkz_1} = E_{0+}e^{-jk(z_2-l)} = E_{2+}e^{jkl} \end{aligned} \qquad (2.47)$$

And similarly,

$$E_{1-} = E_{2-}e^{-jkl} \qquad (2.48)$$

We can show it in matrix form:

$$\begin{bmatrix} E_{1+} \\ E_{1-} \end{bmatrix} = \begin{bmatrix} e^{jkl} & 0 \\ 0 & e^{-jkl} \end{bmatrix} \begin{bmatrix} E_{2+} \\ E_{2-} \end{bmatrix} \qquad \text{propagation matrix} \qquad (2.49)$$

It follows that the relationship between reflection coefficient Γ_1 and Γ_2 will be related by e^{-2jkl}:

$$\Gamma_1 = \Gamma_2 e^{-2jkl} \qquad (2.50)$$

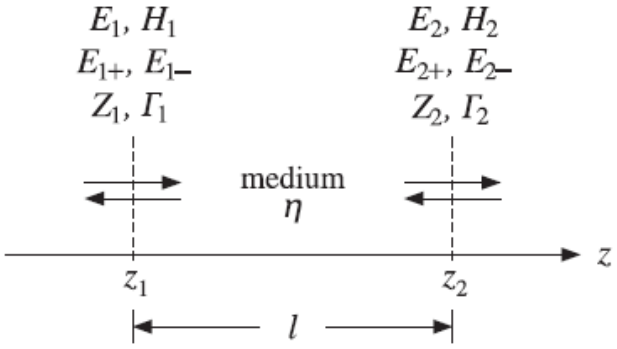


Figure 2.7. Field quantities propagated between two positions in space

In order to express the total electric and magnetic fields E_1, H_1 at position z_1 in terms of E_2, H_2 at position z_2, the previous matrix relationship (2.37) and (2.38) are used.

$$\begin{bmatrix} E_1 \\ H_1 \end{bmatrix} = \begin{bmatrix} 1 & 1 \\ \eta^{-1} & -\eta^{-1} \end{bmatrix} \begin{bmatrix} E_{1+} \\ E_{1-} \end{bmatrix} = \begin{bmatrix} 1 & 1 \\ \eta^{-1} & -\eta^{-1} \end{bmatrix} \begin{bmatrix} e^{jkl} & 0 \\ 0 & e^{-jkl} \end{bmatrix} \begin{bmatrix} E_{2+} \\ E_{2-} \end{bmatrix} \tag{2.51}$$

$$\begin{bmatrix} E_1 \\ H_1 \end{bmatrix} = \frac{1}{2} \begin{bmatrix} 1 & 1 \\ \eta^{-1} & \eta^{-1} \end{bmatrix} \begin{bmatrix} e^{jkl} & 0 \\ 0 & e^{-jkl} \end{bmatrix} \begin{bmatrix} 1 & \eta \\ 1 & -\eta \end{bmatrix} \begin{bmatrix} E_2 \\ H_2 \end{bmatrix} \tag{2.52}$$

It can be written in terms of cosine and sinus:

$$\begin{bmatrix} E_1 \\ H_1 \end{bmatrix} = \begin{bmatrix} \cos\delta & j\eta \sin\delta \\ j\eta^{-1} \sin\delta & \cos\delta \end{bmatrix} \begin{bmatrix} E_2 \\ H_2 \end{bmatrix} \tag{2.53}$$

Where δ is the propagation "phase constant", $\delta = kl = k_0 nl = 2\pi(nl)/\lambda_0$, and nl the "optical length". Equation (2.53) and (2.39) gives the wave impedance at the z_1.

$$Z_1 = \frac{E_1}{H_1} = \frac{E_2 \cos\delta + j\eta H_2 \sin\delta}{jE_2\eta^{-1} \sin\delta + H_2 \cos\delta} = \eta \frac{\frac{E_2}{H_2}\cos\delta + j\eta \sin\delta}{\eta \cos\delta + j\frac{E_2}{H_2}\sin\delta} \tag{2.54}$$

which result in:

$$Z_1 = \eta \frac{Z_2 + j\eta \tan\delta}{\eta + jZ_2 \tan\delta} \tag{2.55}$$

Using equation (2.42) and (2.50), we can express Z_1 in terms of coefficient Γ_2.

$$Z_1 = \eta \frac{1+\Gamma_1}{1-\Gamma_1} = \eta \frac{1+\Gamma_2 e^{-2jkl}}{1-\Gamma_2 e^{-2jkl}} \tag{2.56}$$

Finally, consider the propagation distance is any integral multiple of $l = \lambda/4$ and $\lambda/2$. These special cases are called the quarter-wavelength, the half-wavelength, respectively. In the half-wavelength case, we have $2kl = 2\frac{2\pi}{\lambda}\frac{\lambda}{2} = 2\pi$. It follows from equation (2.50) and (2.55) that $\Gamma_1 = \Gamma_2$ and $Z_1 = Z_2$. At the same time, this is matching condition. The reflection coefficients and impedances are equal. In the quarter-wavelength case, we have $2kl = 2\frac{2\pi}{\lambda}\frac{\lambda}{4} = \pi$. It follows from equation (2.50) and (2.55) that $\Gamma_1 = -\Gamma_2$ and $Z_1 = \frac{\eta^2}{Z_2}$. The reflection coefficients changes sign and the wave impedance inverts.

$$\begin{aligned} l &= \frac{\lambda}{2} \;\Rightarrow\; Z_1 = Z_2,\ \Gamma_1 = \Gamma_2 \\ l &= \frac{\lambda}{4} \;\Rightarrow\; Z_1 = \frac{\eta^2}{Z_2},\ \Gamma_1 = -\Gamma_2 \end{aligned}$$

2.5.2. Matching Matrices

When the electric field hit on any dielectric interface, some of electric field will reflect backwards and the remaining electric filed will transmit forwards. The interface separating two medium is planar. The reflection and transmission coefficients depend on the characteristic impedance of two media. Figure 2.8 shows two dielectric/conducting media with characteristic impedance η, η'. In the figure, the electric fields is considered to move on the interface from two directions. Because

the field reflected from the second interface goes through the first interface. The incident electric field from left to the right direction is E_+. The incident electric field from right to the left direction is $E_-^{'}$. The reflection electric field from right to the left direction is E_-. The reflection electric field from left to the right direction is $E_+^{'}$. According to the continuous rule, total electric and magnetic fields must be equal across the two sides.

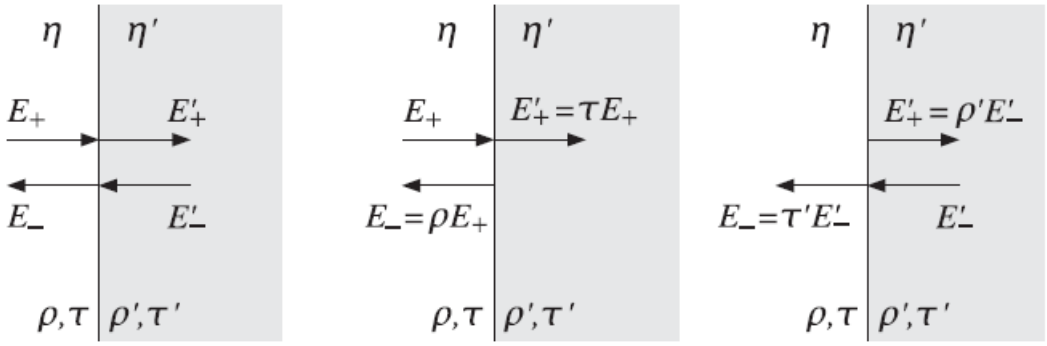


Figure 2.8. Field across an interface

$$E = E^{'} \;\Rightarrow\; E_+ + E_- = E_+^{'} + E_-^{'}$$

(continuity across interface) (2.57)

$$H = H^{'} \;\Rightarrow\; \frac{1}{\eta}(E_+ + E_-) = \frac{1}{\eta^{'}}(E_+^{'} - E_-^{'})$$

The incident electric field on the left side can be written in terms of electric field on right side:

$$E_+ = E_+^{'}(\frac{\eta^{'} + \eta}{2\eta^{'}}) + E_-^{'}(\frac{\eta^{'} - \eta}{2\eta^{'}}) \qquad (2.58)$$

It is convenient at this point to determine the elementary reflection and transmission coefficient ρ and τ, respectively. Where the elementary reflection ρ is equal to

$\frac{\eta^{'}-\eta}{\eta^{'}+\eta}$. It is similar to $\Gamma=\frac{Z-\eta_0}{Z+\eta_0}$ in equation (2.41). The equation (2.58) can be written in terms of ρ and $\tau=\frac{2\eta^{'}}{\eta^{'}+\eta}$:

$$E_{+}=E_{+}^{'}(\frac{\eta^{'}+\eta}{2\eta^{'}})+E_{-}^{'}(\frac{\eta^{'}-\eta}{\eta^{'}+\eta})(\frac{\eta^{'}+\eta}{2\eta^{'}})=E_{+}^{'}\frac{1}{\tau}+E_{-}^{'}\rho\frac{1}{\tau} \qquad (2.59)$$

In the same way, reflected electric field on the left side can be found similarly:

$$E_{-}=E_{+}^{'}(\frac{\eta^{'}-\eta}{2\eta^{'}})+E_{-}^{'}(\frac{\eta^{'}+\eta}{2\eta^{'}})$$

$$E_{-}=E_{+}^{'}(\frac{\eta^{'}-\eta}{\eta^{'}+\eta})(\frac{\eta^{'}+\eta}{2\eta^{'}})+E_{-}^{'}(\frac{\eta^{'}+\eta}{2\eta^{'}})=E_{+}^{'}\rho\frac{1}{\tau}+E_{-}^{'}\frac{1}{\tau} \qquad (2.60)$$

The fields $E_{\pm}$ on the left side can be written in terms of the fields $E_{\pm}^{'}$ on the right side using Equation (2.59 and 2.60) in a matrix form:

$$\begin{bmatrix}E_{+}\\E_{-}\end{bmatrix}=\frac{1}{\tau}\begin{bmatrix}1&\rho\\\rho&1\end{bmatrix}\begin{bmatrix}E_{+}^{'}\\E_{-}^{'}\end{bmatrix} \qquad \text{(matching matrix)} \qquad (2.61)$$

and inversely, the fields $E_{\pm}^{'}$ on the right side can be represented by the fields $E_{\pm}$ on the left side:

$$\begin{bmatrix}E_{+}^{'}\\E_{-}^{'}\end{bmatrix}=\frac{1}{\tau^{'}}\begin{bmatrix}1&\rho^{'}\\\rho^{'}&1\end{bmatrix}\begin{bmatrix}E_{+}\\E_{-}\end{bmatrix} \qquad (2.62)$$

Where $\rho^{'}$ and $\tau^{'}$ are the elementary reflection and transmission coefficients from the right of the interface as shown in Figure 2.8, defined in terms of $\eta,\ \eta^{'}$ as follows:

$$\rho^{'}=\frac{\eta-\eta^{'}}{\eta^{'}+\eta},\quad \tau^{'}=\frac{2\eta}{\eta^{'}+\eta} \qquad (2.63)$$

Figure 2.8 shows that normally incident field are tangential to the interface plane. According to equation (2.31) and Table 2.1, total electric and magnetic field must be continuous across the two sides of the interface. This causes that the wave impedance is continuous across the interface (Eq. 2.64). Using this rule, it can be shown that reflection coefficients match with relationship which is more complicated.

$$\begin{aligned} Z &= Z' \\ \frac{E}{H} &= \frac{E'}{H'} \end{aligned} \tag{2.64}$$

Equation (2.42) is relationship between Z and Γ. When this equation is applied on the left and right side of the interface, we have:

$$\eta \frac{1+\Gamma}{1-\Gamma} = \eta' \frac{1+\Gamma'}{1-\Gamma'} \tag{2.65}$$

which can be solved to get the reflection coefficient Γ :

$$\begin{aligned} &(1+\Gamma)(1-\Gamma')\eta = \eta'(1+\Gamma')(1-\Gamma) \\ &\eta - \eta\Gamma' + \eta\Gamma - \eta\Gamma\Gamma' = \eta' - \eta'\Gamma + \eta'\Gamma' - \eta'\Gamma\Gamma' \\ &\Gamma(\eta - \eta\Gamma' + \eta' + \eta'\Gamma') = \eta' + \eta'\Gamma' - \eta + \eta\Gamma' \\ &\Gamma = \frac{(\eta' - \eta) + \Gamma'(\eta' + \eta)}{(\eta' + \eta) + \Gamma'(\eta' - \eta)} \end{aligned} \tag{2.66}$$

If the term on the right is divided to $(\eta' + \eta)$, using the equation $\rho = (\eta' - \eta)/(\eta' + \eta)$ it reduces to :

$$\Gamma = \frac{\rho + \Gamma'}{1 + \Gamma'\rho} \quad \leftrightarrow \quad \Gamma' = \frac{\rho' + \Gamma}{1 + \Gamma\rho'} \tag{2.67}$$

Thus, the matching conditions for Γ and Γ' are derived with above result. Next, we consider that there are two special cases, illustrated in Figure 2.8. The first case $E_-' = 0$: the incident field from the right is absent. The second case $E_+ = 0$: the

incident field from the left is absent. For the first case, $\Gamma' = E_-'/E_+' = 0$, which the equation (2.65) turns out:

$$Z = Z' = \eta' \frac{1+\Gamma'}{1-\Gamma'} = \eta' \tag{2.68}$$

and equation (2.67) turns out :

$$\Gamma = \frac{\rho + \Gamma'}{1+\Gamma'\rho} = \rho \tag{2.69}$$

Equation (2.59) and (2.60) implies in this case (for $E_-' = 0$):

$$E_+ = E_+' \frac{1}{\tau} \text{ and } E_- = E_+' \rho \frac{1}{\tau} \tag{2.70}$$

To show the reflection and transmission coefficients for left incident fields, E_-, E_+' are expressed in terms of E_+ :

$$\begin{aligned} E_- &= \rho E_+ \\ E_+' &= \tau E_+ \end{aligned} \quad \text{(left-incident fields)} \tag{2.71}$$

For the second case, $\Gamma = E_-/E_+ = \infty$, which implies :

$$Z = Z' = \eta \frac{1+\Gamma}{1-\Gamma} = -\eta \tag{2.72}$$

and equation (2.67) turns out :

$$\Gamma' = \frac{\rho' + \Gamma}{1+\Gamma\rho'} = \frac{1}{\rho'} \tag{2.73}$$

Equation (2.59) and (2.60) implies in this case (for $E_+ = 0$) :

$$E_+' = (-\rho)E_-' \quad \text{and} \quad E_- = E_+' \rho \frac{1}{\tau} + E_-' \frac{1}{\tau} \tag{2.74}$$

To show the reflection and transmission coefficients for right incident fields, E_-, E_+' are expressed in terms of E_-' with the help of $\rho = -\rho'$ and $(1-\rho^2) = \tau\tau'$:

$$E_+^{'} = \rho^{'} E_-^{'}$$
$$E_- = \tau^{'} E_-^{'} \qquad \text{(right-incident fields)} \qquad (2.75)$$

For instance, when we apply two port measurements with network analyzer and two ports are excited as source, incident fields from both sides will take place. Then, the two right–hand side of equation (2.71,left-incident fields) and (2.75,right-incident fields) are added to obtain the transmission fields $(E_+^{'}, E_-)$ in terms of the incident ones $(E_+, E_-^{'})$.

$$E_- = \rho E_+ + \tau^{'} E_-^{'}$$
$$E_+^{'} = \tau E_+ + \rho^{'} E_-^{'} \qquad (2.76)$$

This gives the "scattering matrix" relating the transmission fields to the incident ones:

$$\begin{bmatrix} E_- \\ E_+^{'} \end{bmatrix} = \begin{bmatrix} \rho & \tau^{'} \\ \tau & \rho^{'} \end{bmatrix} \begin{bmatrix} E_+ \\ E_-^{'} \end{bmatrix} \qquad (2.77)$$

2.5.3. Single Dielectric Slab

Reflectivity and transmission of a single dielectric slab can be thought as reflectivity and transmission from an interface and propagation between two positions in a medium. That is why propagation and matching matrices have been derived in the previous chapter. For example, Figure 2.9 shows that a dielectric slab with impedance η_1 separates the semi-infinite media of η_a and η_b. The electromagnetic field propagating along the right direction passes through three medium which is coded I, II and III from left to right, respectively. In this case, we have two planar interfaces. There is only one incident field in medium I that propagates from left to the planar interface. In medium II, there is forward and backward field due to the reflections between planes. In medium III, there is only a forward wave because incident field from right to the second interface is absent.

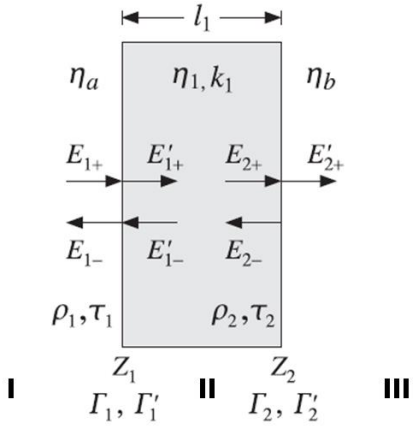


Figure 2.9. Single dielectric slab

Where l_1 is the width of the slab, $k_1 = \omega/c_1$ is the propagation wavenumber, $\lambda_1 = 2\pi/k_1$ and λ_0 are the corresponding wavelength within the slab and the free-space wavelength, respectively. To determine the reflection coefficient Γ_1 at the medium I, equation (2.67) and (2.50) need to be used together. Firstly, reflection coefficient Γ_1 is determined in terms of $\Gamma_1^{'}$. Then, it is propagated to the left of the second interface.

$$\Gamma_1 = \frac{\rho_1 + \Gamma_1^{'}}{1 + \Gamma_1^{'}\rho_1} = \frac{\rho_1 + \Gamma_2 e^{-2jk_1l_1}}{1 + \rho_1\Gamma_2 e^{-2jk_1l_1}} \tag{2.78}$$

There is no backward field in medium III. So we have $\Gamma_2^{'} = 0$. Thus, Γ_2 reduces :

$$\Gamma_2 = \frac{\rho_2 + \Gamma_2^{'}}{1 + \rho_2\Gamma_2^{'}} = \rho_2 \tag{2.79}$$

We finally find Γ_1 with the substitution $\Gamma_2 \to \rho_2$:

$$\Gamma_1 = \frac{\rho_1 + \rho_2 e^{-2jk_1l_1}}{1 + \rho_1\rho_2 e^{-2jk_1l_1}} \tag{2.79}$$

It is useful in transforming this expression into impedance form. So the wave impedance at the left-side of both interface is $Z_2 = Z_2^{'} = \eta_b$ *and* $Z_1 = Z_1^{'}$. Thus, we can obtain the wave impedance at the first interface with the help of the equation (2.55):

$$Z_1 = \eta_1 \frac{\eta_b + j\eta_1 \tan k_1 l_1}{\eta_1 + j\eta_b \tan k_1 l_1} \tag{2.80}$$

For a single dielectric slab, the overall transmission response is considered to be related the passing electric field from medium I to medium III. So the transmission and reflection coefficients are :

$$\begin{aligned} T &= \frac{E_{2+}^{'}}{E_{1+}} \\ R &= \frac{E_{1-}}{E_{1+}} \end{aligned} \tag{2.81}$$

The ratio of the transmitted to incident field is called transmission coefficient and the ratio of the reflected to the incident field is called the reflection coefficient. To get these quantities for such dielectric slab, we must apply the method which works again with the matching and propagation matrices. Firstly applying the matching matrices in Eq. 2.61 to get electric field term at the right-side of the first interface and secondly the propagation matrices in Eq. 2.49 is used to propagate the electric field to the left-side of the second interface. And then using the matching matrices is used again to pass through the third medium.

$$\begin{bmatrix} E_{1+} \\ E_{1-} \end{bmatrix} = \frac{1}{\tau_1}\begin{bmatrix} 1 & \rho_1 \\ \rho_1 & 1 \end{bmatrix}\begin{bmatrix} E_{1+}^{'} \\ E_{1-}^{'} \end{bmatrix} = \frac{1}{\tau_1}\begin{bmatrix} 1 & \rho_1 \\ \rho_1 & 1 \end{bmatrix}\begin{bmatrix} e^{jk_1 l_1} & 0 \\ 0 & e^{-jk_1 l_1} \end{bmatrix}\begin{bmatrix} E_{2+} \\ E_{2-} \end{bmatrix}$$

$$\begin{bmatrix} E_{1+} \\ E_{1-} \end{bmatrix} = \frac{1}{\tau_1}\begin{bmatrix} 1 & \rho_1 \\ \rho_1 & 1 \end{bmatrix}\begin{bmatrix} e^{jk_1 l_1} & 0 \\ 0 & e^{-jk_1 l_1} \end{bmatrix}\frac{1}{\tau_2}\begin{bmatrix} 1 & \rho_2 \\ \rho_2 & 1 \end{bmatrix}\begin{bmatrix} E_{2+}^{'} \\ 0 \end{bmatrix}$$

$$\begin{bmatrix} E_{1+} \\ E_{1-} \end{bmatrix} = \frac{1}{\tau_1\tau_2}\begin{bmatrix} e^{jk_1 l_1} & \rho_1 e^{-jk_1 l_1} \\ \rho_1 e^{jk_1 l_1} & e^{-jk_1 l_1} \end{bmatrix}\begin{bmatrix} 1 & \rho_2 \\ \rho_2 & 1 \end{bmatrix}\begin{bmatrix} E_{2+}^{'} \\ 0 \end{bmatrix}$$

$$\begin{bmatrix} E_{1+} \\ E_{1-} \end{bmatrix} = \frac{1}{\tau_1\tau_2}\begin{bmatrix} e^{jk_1l_1} + \rho_1\rho_2 e^{-jk_1l_1} & \rho_2 e^{jk_1l_1} + \rho_1 e^{-jk_1l_1} \\ \rho_1 e^{jk_1l_1} + \rho_2 e^{-jk_1l_1} & \rho_1\rho_2 e^{jk_1l_1} + e^{-jk_1l_1} \end{bmatrix}\begin{bmatrix} E'_{2+} \\ 0 \end{bmatrix} \tag{2.82}$$

where we take $E'_{2-} = 0$,because of no incident field in third medium. Multiplying the matrix factors out, we obtain the fields on the left side of the slab related to the field at the right side:

$$\begin{aligned} E_{1+} &= \frac{e^{jk_1l_1}}{\tau_1\tau_2}\left(1 + \rho_1\rho_2 e^{-2jk_1l_1}\right)E'_{2+} \\ E_{1-} &= \frac{e^{jk_1l_1}}{\tau_1\tau_2}\left(\rho_1 + \rho_2 e^{-2jk_1l_1}\right)E'_{2+} \end{aligned} \tag{2.83}$$

Eventually, we find reflection and transmission response using equation (2.81) and (2.83).

$$\begin{aligned} R_{tot} &= \frac{E_{1-}}{E_{1+}} = \frac{\rho_1 + \rho_2 e^{-2jk_1l_1}}{1 + \rho_1\rho_2 e^{-2jk_1l_1}} \\ \mathrm{T}_{tot} &= \frac{E'_{2+}}{E_{1+}} = \frac{\tau_1\tau_2 e^{-jk_1l_1}}{1 + \rho_1\rho_2 e^{-2jk_1l_1}} \end{aligned} \tag{2.84}$$

If we represent the reflection and transmission in terms of power, we have to define "Poynting vector" that is the power flow density of the electromagnetic wave which is expressed by the equation (2.85).

$$\vec{\mathrm{P}} = \vec{E} \times \vec{H} \qquad \text{Poynting Vector} \tag{2.85}$$

$$\vec{\mathrm{P}} = \frac{1}{2}\mathrm{Re}\left(\vec{E} \times \vec{H}\right) \qquad \text{Time-Averaged Poynting Vector} \tag{2.86}$$

Using the equation (2.33), the time-averaged Poynting vector can be written as $\mathrm{P} = (1/2\eta)|E|^2$. There is continuity equations at the interface in Figure 2.8. However, Poynting vector is conserved across the interface. So the reflected power will be equal to the transmitted power (assuming $E'_{-} = 0$):

$$\frac{1}{2\eta}\left(\left|E_{+}\right|^{2}-\left|E_{-}\right|^{2}\right)=\frac{1}{2\eta^{'}}\left|E_{+}^{'}\right|^{2} \tag{2.87}$$

Using the transformation of (2.71) we find:

$$\frac{1}{2\eta}\left|E_{+}\right|^{2}\left(1-\left|\rho\right|^{2}\right)=\frac{1}{2\eta^{'}}\left|E_{+}\right|^{2}\left|\tau\right|^{2} \tag{2.88}$$

$$\frac{1}{\eta}\left(1-\left|\rho\right|^{2}\right)=\frac{1}{\eta^{'}}\left|\tau\right|^{2} \tag{2.89}$$

Similarly, for the lossless dielectric slab, Poynting vector is conserved across the dielectric slab which can be proved using (2.84):

$$\frac{1}{\eta_{a}}\left(1-\left|R_{tot}\right|^{2}\right)=\frac{1}{\eta_{b}}\left|\mathrm{T}_{tot}\right|^{2} \tag{2.90}$$

And the fractions of power:

$$\frac{\mathrm{P}_{reflected}}{P_{incident}}=\frac{\frac{1}{2\eta_{b}}\left|E_{1-}\right|^{2}}{\frac{1}{2\eta_{a}}\left|E_{1+}\right|^{2}}=\left|R_{tot}\right|^{2}$$

$$\frac{\mathrm{P}_{transmitted}}{P_{incident}}=\frac{\frac{1}{2\eta_{b}}\left|E_{2+}^{'}\right|^{2}}{\frac{1}{2\eta_{a}}\left|E_{1+}\right|^{2}}=\frac{\eta_{a}}{\eta_{b}}\left|T_{tot}\right|^{2} \tag{2.91}$$

Now, we consider that medium I and III are same and the free space. In this assumption, the characteristic impedances are taken to be $\eta_{a}=\eta_{b}=\eta_{0}$. Many expressions , such as $\rho_{1},\rho_{2},\tau_{1},\tau_{2},\square,\mathrm{T}$, transform into:

$$\rho_1 = \frac{\eta_1 - \eta_0}{\eta_1 + \eta_0}, \quad \rho_2 = \frac{\eta_0 - \eta_1}{\eta_1 + \eta_0}, \tau_1 = 1 + \rho_1, \tau_2 = 1 - \rho_1$$

$$\rho_1 = -\rho_2 \quad ; \quad \tau_1 \tau_2 = 1 - \rho_1^2$$

$$R_{tot} = \frac{\rho_1 \left(1 - e^{-2jk_1 l_1}\right)}{1 - \rho_1^2 e^{-2jk_1 l_1}} \tag{2.92}$$

$$\mathrm{T}_{tot} = \frac{\left(1 - \rho_1^2\right) e^{-jk_1 l_1}}{1 - \rho_1^2 e^{-2jk_1 l_1}}$$

and power expression for the transmitted field :

$$\frac{\mathrm{P}_{transmitted}}{P_{incident}} = \left|T_{tot}\right|^2 \tag{2.93}$$

We can take $e^{-jk_1 l_1}$ as T, so the total reflection and transmission relationships take the simplified forms [100] :

$$R_{tot} = \frac{\rho_1 \left(1 - \mathrm{T}^2\right)}{1 - \rho_1^2 \mathrm{T}^2}$$
$$\mathrm{T}_{tot} = \frac{\left(1 - \rho_1^2\right) \mathrm{T}}{1 - \rho_1^2 \mathrm{T}^2} \tag{2.94}$$

2.6. Types of Microwave Absorbing Material

Radar cross section (RCS) is a measure of scattered of electromagnetic wave by any object. It is a function of direction, frequency and polarization of the incident wave. It depends on the type, shape and size of the target object. Moreover, it is related to the size of the target object relative to the wavelength and angle of the incident wave with it. To minimize the electromagnetic wave reflected from the material, it must have the low RCS level. That is why the reflection loss of the materials are maximized by designing various shapes that scatter the electromagnetic waves to the different directions [105].

The radar absorbing materials can be mainly classified into two groups: Graded dielectric (or impedance matching absorber) and resonant absorber. The reflection loss of the electromagnetic wave is proportional to the magnitude of the impedance difference between incident and transmitting media. The absorption property of the microwave absorber material depends on the temperature of the media, the dielectric/magnetic constant, dimensions, geometry, impedance of the absorber [106-108]. For a good absorption performance, both of the impedance of the transmitting and incident media must be matched. The graded absorbers are used to reduce the impedance step between two media. Graded dielectric absorbers have been mainly developed using three kinds of impedance matching methods which are pyramidal, tapered and matching. The main principle of them is gradual impedance transition from the free space to absorbing material to reduce the reflection as shown in Figure 2.10. Physical graded dielectric absorbers can offer high performance providing EMI (Electromagnetic Interference) absorption levels of –40 dB (99.99% absorbed) to –50 dB (99.999% absorbed). These absorbers have impedance at the front plane close to 377 Ω/square of free space, which decreases gradually to the back surface.

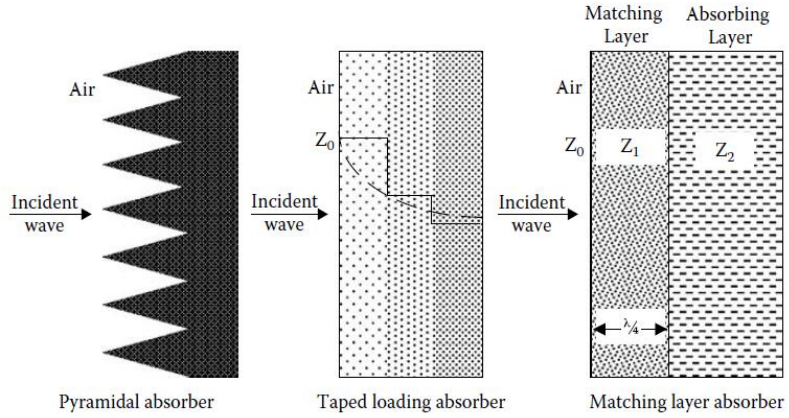


Figure 2.10. Graded dielectric absorbers by impedance matching [90]

Pyramidal absorber is well known examples of graded dielectric absorbers. Pyramidal absorber typically consist of base and pyramid structure as shown in Figure 2.11.

These structures arranged in regularly spaced pattern. When the wavelength of the incident wave is longer or the structure is smaller, the wave will experience a more abrupt change in the impedance. That is why the height and periodicity of the pyramid should be on the order of one wavelength. In other words, these absorbers have a minimum operating frequency which is constrained by the length of the pyramid. If the frequency is higher than the minimum operating frequency, it provides high attenuation and becomes the best performance for absorber. For any absorber material, its reflection loss level must be at least -10 dB. For any pyramidal microwave absorber, the desired minimum value of reflection loss is to be below -30 dB. However, in the case that the height of the absorber is much longer than the operating wavelength, the absorption level higher than 50 dB can be obtained. Although pyramidal absorbers have the best absorption performance, wide frequency and angle range at the higher than operating frequency, their thickness and fragility are the disadvantage of the pyramidal absorbers.

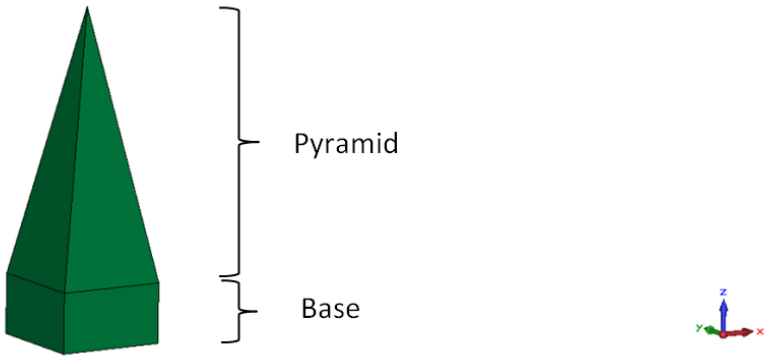


Figure 2.11. Illustration of Single pyramidal absorber

As shown in Figure 2.10, the tapered loading absorber is typically a slab composed of low loss and lossy material. Note that lossy component is increasing along the direction of propogation of the incident wave in the material. But it is homogenous along the surface. This type absorber can be produced by immersing open cell foam to the lossy material. However, by using this production method it is difficult to make

gradually impedance transition. Although the tapered loading absorber becomes thinner, its absorption performance is less than the others.

The matching layer absorber is similar to the tapered loading absorber. It may be thought as the tapered loading absorber with two transition form as shown in Figure 2.10. The layer between air and absorbing media is called the matching layer whose impedance value is between the impedances of the absorbing layer and air. So that, the incident wave matches with the absorber without any reflection. The idea is to have the combined impedance from the first and second layers to equal to the impedance of the incident medium. This event occurs only when the thickness of the matching layer is equal to the one quarter of a wavelength of the radiation in the layer. That is why the operating band of matching layer absorber is narrow because it is only possible that the thickness of the matching layer equal to the optical thickness [90].

Pyramidal absorbers are usually preferred because of its good absorption performance. There are various types of pyramidal absorber whose base can be triangle, square and hexagonal [106,108,109]. The absorbers based on different base shape may give different absorption rate. The literature reveals that the pyramidal absorber based on isosceles triangle with dielectric constant of $\varepsilon_r = 2$ has about -47 dB reflection loss at the frequency range between 5-10 GHz . However the reflection loss for square base with same dielectric constant at the same frequency range gives about -44 dB [109].

The truncated pyramidal absorber is created by chopping the top off the pyramid. The normal, coated, hollow absorbers with the same shape and dielectric material exhibit different reflection losses [108]. The distance between pyramid structures play an important role in increasing the reflection loss level as the effect of pyramid shapes. According to the literature, for instance, the double pyramidal absorber whose pyramids are closer to each other gives better reflection loss level than the case that pyramids are away from each other [110]. As you know that the reflection loss performance can be increased by shape effect of pyramid, another way of enhancing the reflection loss performance is to use the resistive sheet called FSS (Frequency-Selective Surface). The reflection loss level and absorption frequency of composite

absorber can be improved by changing the type/shape/ size/thickness of FSS [107]. At the same time, the type of the nanopowders used in the absorber is the one of the parameter that determines the absorption frequency and bandwidth. For instance, while the pyramidal absorber of granular Ni-Zn ferrite performs low reflectivity at low frequency, the pyramidal absorber of carbonyl iron powders performs low reflectivity at high frequency. Briefly, different microwave absorbing material used in the absorber leads to the shifting the absorbing frequency. Additionally, the mixture of these two materials gives the wider absorption bandwidth [112].

Another most common absorber is wedge absorber. There are many types of wedge absorber: oblique, truncated, hollow, corrugated and coated wedge absorber. The wedge absorber which is the length of the upper edge shorter than the length of the base edge is called the "oblique wedge absorber". Such microwave absorbers can be installed in the anechoic chamber. They can be arranged in various patterns such as W, X, Y and Z to increase the surface area contacted the electromagnetic wave [113]. The wedge absorbers can be created by cutting top off the wedge as well as pyramidal absorbers. This kind of absorber is called truncated wedge absorber. The reflection loss varies little in this case that the top of the wedge absorber coated with extra layer. Of course, this depends on the absorption property of the coated layer. The truncated wedge absorber which is hollow out inside it is not enough good over the wide bandwidth. But it performs high reflection loss peak at specific frequency points [108]. Another type of absorber exist that its surface is designed as square corrugated [114]. Additionally to these, the shape effects of microwave absorbers can be modeled by using the software such as CST Microwave Studio [106–110].

Another type of absorber is "resonant absorber". It may be mainly grouped into Dallenbach (Tuned) Layer, Salisbury Screen and Jaumann Layers which are the oldest and elementary absorbers. In this class of materials the fundamental principle is to utilize the destructive interference of propagation electromagnetic waves. As shown in Figure 2.12, a Dallenbach Layer is composed of two layers which are homogeneous lossy absorber and metal. The incident wave is reflected by first and second layer. So that a destructive interference occurs at the first interface between incident and absorbing media If it satisfies the quarter wavelength condition mentioned in the previous section (2.5.1). But no all power of the incident wave is

absorbed because of the impedance mismatching between two media. In order to enhance the absorption characteristics, the real and complex permittivity ($\varepsilon', \varepsilon''$), the real and complex permeability (μ', μ'') and thickness of layer have to be adjusted. At this point, we can use equation (2.80) to obtain impedance equation for Dallenbach layer. It can be written in the phase form using equation 2.18:

$$Z_1 = \eta_1 \frac{Z_{load} + j\eta_1 \tan \gamma t}{\eta_1 + jZ_{load} \tan \gamma t} \tag{2.95}$$

Where impedance of metal used as load is $Z_{load} = 0$ and the propagation constant $\gamma = j\omega\sqrt{\mu\varepsilon}$ is complex. We rearrange the above impedance equation and it is reduced like that:

$$Z_1 = \eta_1 j \tan \gamma t \tag{2.96}$$

When the effective impedance of the layer is equal to impedance of air 377 Ω/square and the magnitude of waves reflected from absorber interface and metal equal each other, total reflected intensity is zero.

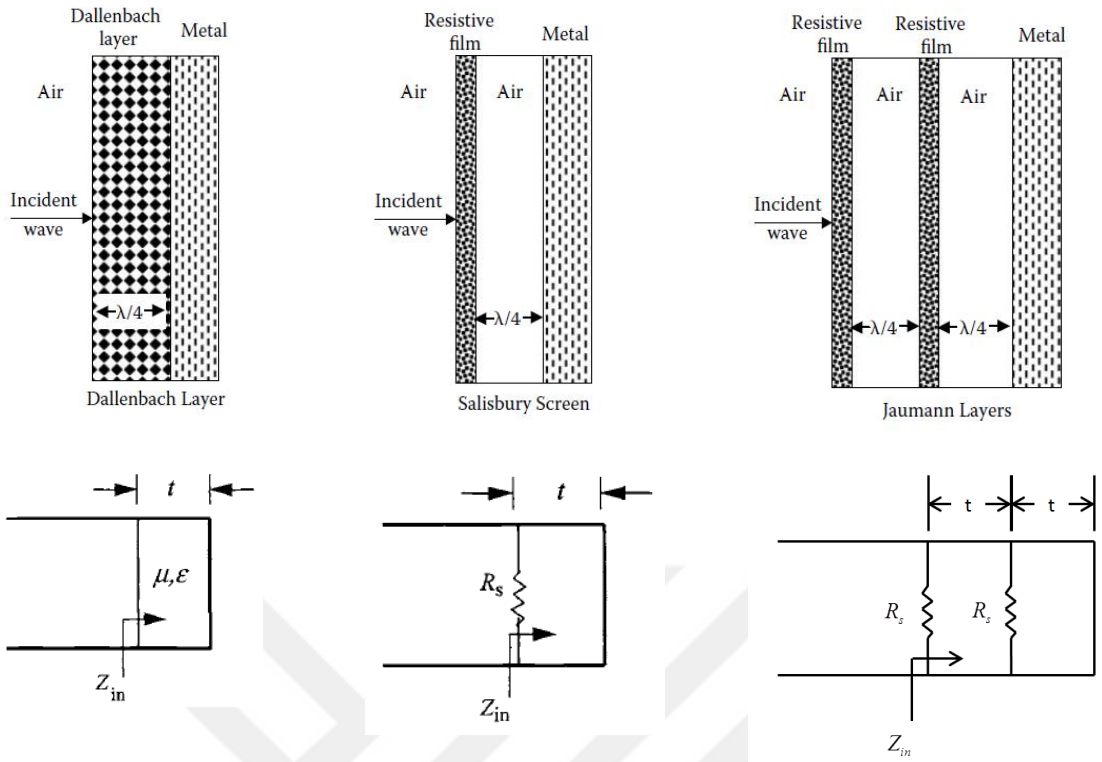


Figure 2.12. Basic Resonant absorbers and their transmission equivalent circuits [90,115]

Salisbury Screen can be thought as another form of Dallenbach layer. Instead of bulk layer, the Salisbury Screen has a resistive sheet to adjust the effective impedance. The resistive sheet is placed $\lambda/4$ distance away from the metal. The media between metal and resistive sheet is usually air gap. According to the transmission line theory, in the case of the quarter wavelength the open circuit condition is observed at the input of the structure. So that The Salisbury Screen can function as "*a perfect absorber*". However, short circuit condition reappears when the half wavelength condition occurs by placing resistive sheet $\lambda/2$ distance away from the metal. So the structure can function as "*a perfect reflector*". The impedance can be found using the transmission line equivalent circuit for open circuit condition as shown in Figure 2.12. The input impedance of Salisbury Screen becomes:

$$\frac{1}{Z_{in}} = \frac{1}{R_s} + \frac{1}{\infty} = \frac{1}{R_s} \tag{2.97}$$

So the effective impedance of the Salisbury Screen transforms into the sheet resistance (R_s). To obtain good impedance matching, the thin sheet resistance is chosen as 377 (Ω/square). However, the disadvantage of it is to operate only at a single frequency. Because, one layer allows the cancellation of reflection waves for only one frequency. Due to the narrow bandwidth of single-layer or single-sheet absorber, the multilayer dielectric absorbers are required in military applications to improve the operation frequency bandwidth. The Jaumann absorber is a type of multilayer resonant absorber. The first device is formed by two resistive sheets and spacers. It is a modification of The Salisbury Screen. The purpose of using the Jaumann absorber is to increase the bandwidth of the Salisbury Screen. Much sheets used lead to increasing the bandwidth as shown in Figure 2.13. For this illustration, the gap between sheets is taken as 0.75 cm. We see that for one sheet the fractional bandwidth is 0.27 while it is 1.16 for four sheets [116].

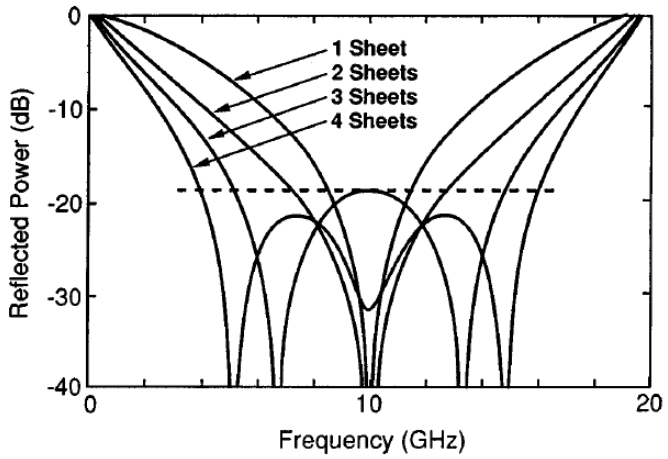


Figure 2.13. Reflection performance of Jaumann absorber for different number of sheets [116]

2.7. Anechoic Chamber

EMC or antenna test is conducted by using the anechoic chamber if OATM is not possible because of different noise sources [117]. A typical anechoic chamber consists of antenna system, shielded room, DUT (Device under test) and RAM

installed on the wall, ceiling and floor as shown in Figure 2.14. Usually, the pyramidal, wedge and flat absorbers are used in the anechoic chamber [118]. The electromagnetic wave caused by inner reflection in the chamber is eliminated by absorber materials. And the noise coming from environment is shielded with grounding the metallic room to simulate the OATM [115]. The pyramidal absorber among the microwave absorbing materials is preferred often in the application of anechoic chamber design because of its wide absorption bandwidth [120].

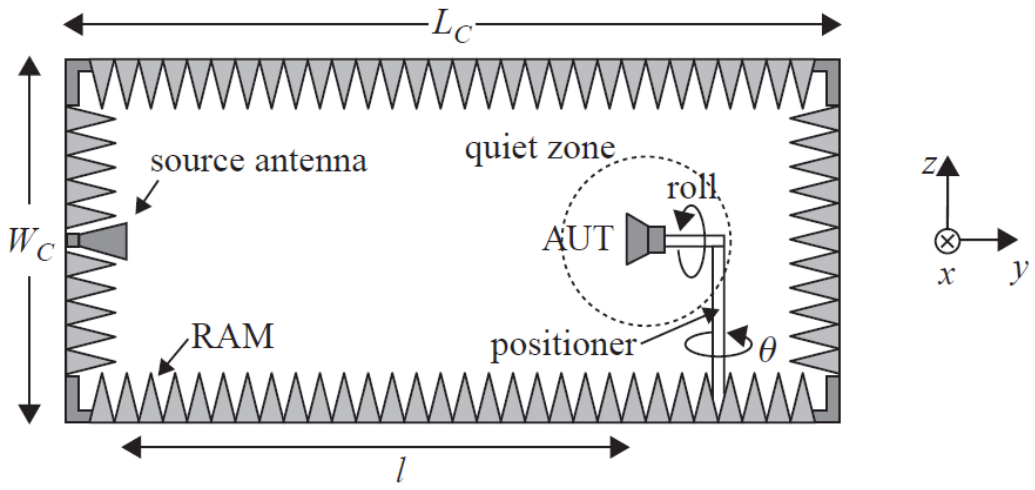


Figure 2.14. Representation of typical Anechoic Chamber [121]

There exists wide range of anechoic chamber from small dimension to large one as long as aircraft shed. Because, the size of the anechoic chamber depends on the size of DUT and operating frequency range [122]. In the perspective of microwave engineering, the anechoic chamber can behave like a cavity resonator and cause the resonances at the some region. In addition to this, the strength of the backscatter signal and absorption level in the anechoic chamber should be considered. The EMC test of anechoic chamber must have the absorption characteristic of the electromagnetic wave which is higher than 20 dB over the 30 MHz–18 GHz frequency range to provide international standards [123]. Before the electromagnetic wave reaches the quiet zone, it must be uniform plane wave to perform precise

measurement. Otherwise, the ripple occurs at the quiet zone due to the multi-path [118]. The measurement is performed in the quiet zone where the backscattering signal may experience destructive interference. The transmitted wave from the source antenna and reflected wave from the absorber on the walls overlap in this zone. And it can affect the measurement accuracy as long as there is wave reflected from absorber. So the absorption performance of the microwave absorbers is so important. At the same time, the propagating wave radiated from the source antenna firstly is in the spherical form. While it moves away the transmitted antenna, the spherical wave transform into uniform plane wave. In practice, it is difficult to get uniform plane wave in the quiet zone. In order to accept approximately uniform plane wave, the phase difference ϕ between spherical and plane wave at the AUT (Antenna under test) must be $\frac{\pi}{8}$ or less than $\frac{\pi}{8}$, as shown in Figure 2.15. This is one of the far-field conditions. In this way, minimum distance to far field (D_{Max}) can be obtained by using the phase requirement [117,120]:

$$R_{\min} = \frac{2D_{\max}^2}{\lambda} \tag{2.98}$$

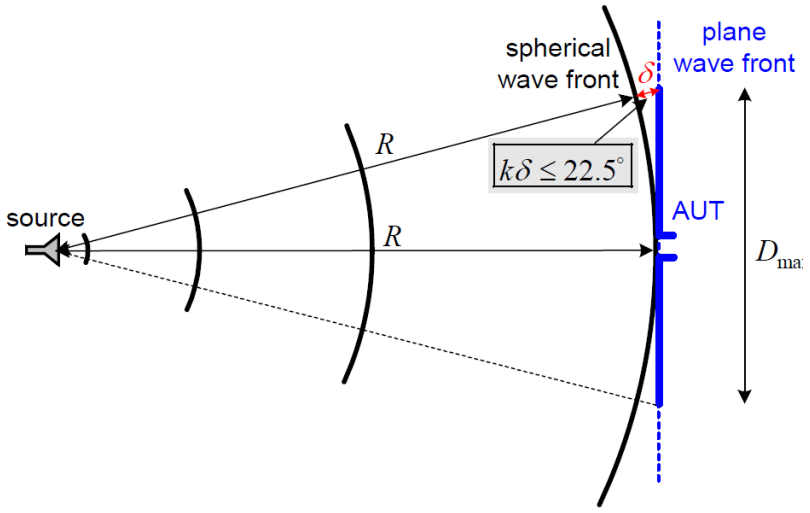


Figure 2.15. Representation of phase between spherical and plane wave [124]

2.8. NRW Calculation and Reflection Loss

The sample inserted in a piece of transmission line separate the medium into three part, as shown in Figure 2.16. This situation results in impedance step between mediums. When the electromagnetic wave reaches the sample, it is reflected and transmitted. According to the transmission/reflection method, the properties of the sample such as dielectric or magnetic constants are derived from the transmission and reflection coefficient of material. Where the reflection coefficient S11 is the ratio of the reflected wave from sample to the incident wave and the transmission coefficient S21 is the ratio of the transmitted wave through the sample to the incident wave. All the four scattering parameter can be get with the help of this method. These parameters such as transmission and reflection coefficients can be obtained from the measurement result of the VNA (Vector Network Analyzer). In a transmission/reflection method the transmission line may be waveguide or coaxial line. The sample in the transmission line affects the impedance of the system. So that the impedance of the transmission line with the sample is different from that of the transmission line without the sample. This difference results in the change of reflection and transmission coefficients [103].

Nicolson, Ross and Weir developed a procedure which calculates the permittivity and permeability using the scattering parameters mentioned above. This calculation method is known as NRW algorithm [125-126].

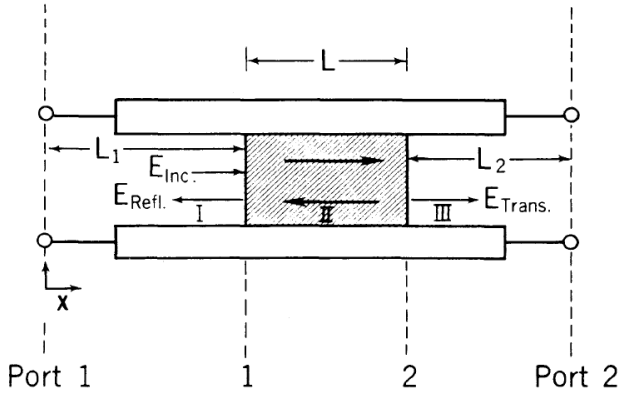


Figure 2.16. Transmission line with the sample and three regions

In the previous chapter, we derived scattering parameter for single layer. Using the equation (2.94) we get the explicit expressions :

$$S_{11} = \frac{\rho(1-T^2)}{1-\rho^2T^2}$$

$$S_{21} = \frac{T(1-\rho^2)}{1-\rho^2T^2} \qquad (2.99)$$

where,

$$T = e^{-\gamma L} = e^{-j\frac{2\pi}{\lambda_0}\sqrt{\mu_r\varepsilon_r}L} \qquad (2.100)$$

$$\rho = \frac{\eta_1 - \eta_0}{\eta_1 + \eta_0} = \frac{\sqrt{\frac{\mu_r}{\varepsilon_r}} - 1}{\sqrt{\frac{\mu_r}{\varepsilon_r}} + 1} \qquad (2.101)$$

In Equation (2.100), the propagation constant of the sample is related to the permittivity and permeability:

$$\gamma = j\frac{2\pi}{\lambda_0}\sqrt{\varepsilon_r\mu_r} = \gamma_0\sqrt{\varepsilon_r\mu_r} \qquad (2.102)$$

To find the ρ and T, in equation (2.99) S_{11} and S_{21} are added and subtracted:

Equation 1: $$S_{11} + S_{21} = \frac{T + \rho - \rho T(T+\rho)}{1-\Gamma^2T^2} \qquad (2.103)$$

Equation 2: $$S_{21} - S_{11} = \frac{T - \rho + \rho T(T-\rho)}{1-\rho^2T^2} \qquad (2.104)$$

Equation 3: $$S_{21}^2 - S_{11}^2 = \frac{T^2 - \rho^2}{1-\rho^2T^2} \qquad (2.105)$$

We define K parameter and it is obtained using above equations:

$$K = \frac{S_{11}^2 - S_{21}^2 + 1}{2S_{11}} = \frac{1 - \rho^2 T^2 - T^2 + \rho^2}{2(1 - T^2)\Gamma} = \frac{1 + \rho^2}{2\rho} \tag{2.106}$$

From this result, the second order equation $\rho^2 - 2\rho K + 1 = 0$ is obtained. The solution of this equation gives the reflection coefficient:

$$\rho = K \pm \sqrt{K^2 - 1} \tag{2.107}$$

In this equation, the correct root of ρ is determined by the condition of $|\rho| \leq 1$. With knowing the reflection coefficient ρ allows us to obtain the transmission coefficient of T from the equation (2.108):

$$T = \frac{S_{11} + S_{21} - \rho}{1 - (S_{11} + S_{21})\rho} \tag{2.108}$$

Using the equation (2.101), $\sqrt{\mu_r / \varepsilon_r}$ is obtained in terms of reflection coefficient ρ :

$$\sqrt{\frac{\mu_r}{\varepsilon_r}} = \frac{(1+\rho)}{(1-\rho)} \tag{2.109}$$

At this point, the complex permittivity ε_r and permeability μ_r can be determined by using Equation (2.108). Substituting $\sqrt{\mu_r} = \frac{\gamma}{\sqrt{\varepsilon_r}\gamma_0}$ into the equation (2.109), we find :

$$\varepsilon_r = \frac{\gamma}{\gamma_0}\frac{(1-\rho)}{(1+\rho)} \tag{2.110}$$

$$\mu_r = \frac{\gamma}{\gamma_0}\frac{(1+\rho)}{(1-\rho)} \tag{2.111}$$

In order to ε_r and permeability μ_r can extract from experimental values, the propagation constant have to be determined with (Eq. 2.100) transmission coefficient of T :

$$\gamma = \frac{\ln(1/T)}{L} \tag{2.112}$$

We note that T is complex number. When it is written in the magnitude and phasor form, the propagation constant that changes depending on the phase angle is seen better.

$$T = |T| e^{j\phi} \tag{2.113}$$

$$\gamma = \frac{\ln(1/|T|)}{L} + j\left(\frac{2\pi n - \phi}{L}\right) \tag{2.114}$$

By using $\ln z = \ln|z| + j(\theta + 2\pi n)$, where $n = 0, \pm 1, \pm 2, ...$ the number of roots in imaginary part are obtained. But the real part of propagation constant γ has single value that doesn't change. From equation (2.17), we know that the phase constant is equal to the imaginary part of the propagation constant:

$$\beta = \frac{2\pi}{\lambda_m} = \mathrm{Im}(\gamma) \tag{2.115}$$

λ_m is the wavelength in the test sample. To define to ε_r and μ_r precisely the thickness of sample should be chosen to be less than λ_m.

$$\frac{L}{\lambda_m} = n - \frac{\phi}{2\pi} \tag{2.116}$$

Three processes occur when the electromagnetic wave illuminates the microwave absorbing material with metal backing. The first is the reflection, transmission and scattering on the surface. The second, the absorption takes place in the lossy medium. The third is the second reflection from the metal backing the absorber and propagation through the lossy medium [127]. The reflection loss equation can be found by using (Eq. 2.96) the complex permittivity and permeability with the expressions [128-129]:

$$Z = \frac{Z_{in}}{Z_0} = \sqrt{\frac{\mu_r}{\varepsilon_r}} \tanh\left(j\frac{2\pi t}{\lambda}\sqrt{\mu_r \varepsilon_r}\right) \tag{2.117}$$

$$RL(dB) = 20\log\left|\frac{Z-1}{Z+1}\right| \qquad (2.118)$$

3. EXPERIMENTAL AND CHARACTERIZATION

The Figure 3.1 shows the synthesis procedure of preparation of nano hexaferrite particles using PMMA polymers. The nanoparticles $MFe_{12}O_{19}$ (M^{+2}=Ba, Sr, Pb) were prepared by using sol-gel process together PMMA. For initial solution, nitrate salts of Ba(II)/Sr(II)/Pb(II)/Fe(III) metals are used in stoichiometric ratio according to the formulas of $BaFe_{12}O_{19}$, $SrFe_{12}O_{19}$ and $PbFe_{12}O_{19}$. The nitrate salts are dissolved in distilled water at a concentration of 0.03M before the citric acid is added to the solution. M^{2+}: Fe^{3+}: citric acid ratio is taken to be 1:11.6:13. The pH value of solution is fixed at 7 by means of ammonia. At this point, the last solution obtained is heated up to the temperature of 80 °C. So that it evaporates slowly until achieving gel state. Then PMMA polymer is added to the prepared sol-gel solution in the ratios of PMMA/ $MFe_{12}O_{19}$: 20/80, 40/60 and 60/40. This sol-gel solution which is stirred with the help of the ultrasonic vibration in 10 minutes is evaporated until it transforms to the viscose residue. This gel form is dried and dehydrated at 110 °C. Then it is allowed to calcinate without any shrinking and crushing at 850 °C during 1 hour. After all these process are achieved, the new samples with PMMA polymer at 20/40/60 percent are synthesized [130].

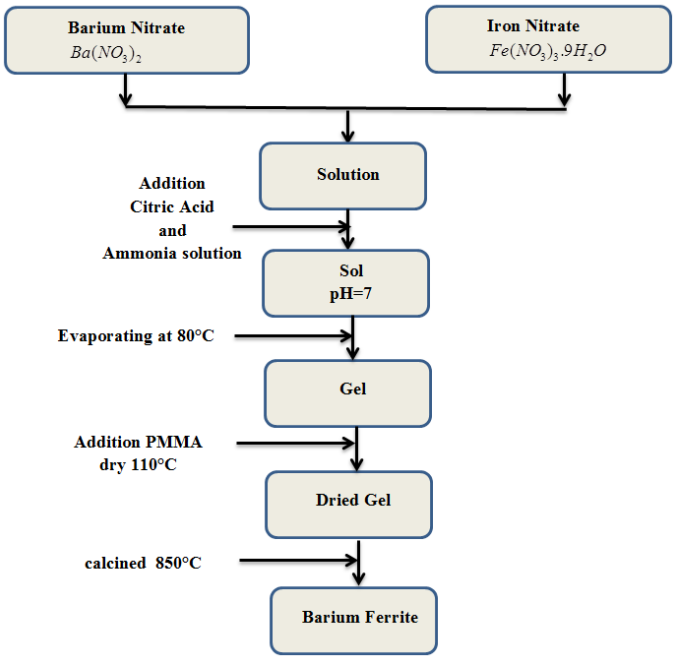


Figure 3.1. Flow chart of sol-gel method for synthesizing barium hexaferrite

3.1. BaM Nanopowders Coated with PMMA

3.1.1. XRD Analysis

X-ray diffraction pattern for BaM hexaferrite with 20/40/60 PMMA ratio is shown in Figure 3.2. It can be seen explicitly that the new synthesized BaM hexaferrites are in the structure of $BaFe_{12}O_{19}$ (ICDD- 39-1433). According to the mentioned figure, the (hkl) indices of the samples are: (101), (110), (008), (112), (107), (200), (108), (203), (205), (206), (011), (110), (209), (300), (217), (0014), (304), (2011), (1112), (218), (2212), (1015), (220), (2013), (2014), (228), (317) and (403) .

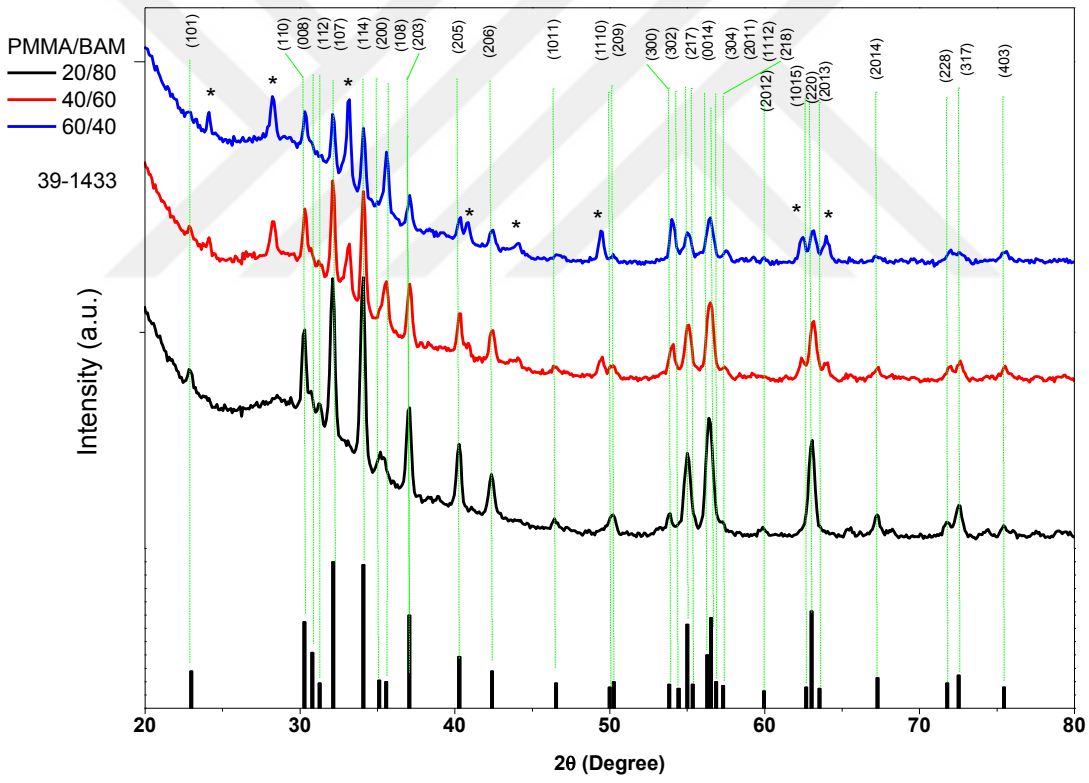


Figure 3.2. XRD pattern of BaM hexaferrites with 20/40/60 PMMA ratios

The peaks marked with "*" symbol indicates different phase structure from the hexaferrite. These peaks are caused by other ferrite structure which are $BaFe_2O_4$ and α-Fe_2O_3 [131]. It is observed that the increasing PMMA ratio arises different phases.

In other words, the sample having least amount of PMMA has less different phase than the others. In this process, hexaferrite powders are mixed with PMMA after they synthesized by sol-gel. Then the resulting gas mixture during the evaporation of PMMA breaks the micro scaled hexaferrite powders down and enable to reduce nano-size [132]. This means that the great amount of PMMA causes dense gas outlet with high energy around the hexaferrite particles and turns the spinel formation. Because hexaferrite crystal structure contains other ferrite structures. Using the "Bragg Law" ($n\lambda = 2d\sin\theta$), the d distance between hkl planes is calculated and listed Table 3.1.

Table 3.1. 2θ values, (hkl) indices and the calculated distance between planes obtained XRD profile for BaM hexaferrite powders.

h	k	L	2θ	d (Å)
1	1	0	30,31	2,95
1	0	7	32,14	2,78
1	1	4	34,25	2,62
2	0	0	35,27	2,54
2	0	3	37,01	2,43
2	0	5	40,22	2, 4
2	0	6	42,43	2,13
2	0	9	5 ,22	1,82
2	1	7	55,09	1,67
2	0	11	56,47	1,63
2	2	0	63,08	1,47
3	1	7	72,53	1,30

The cell parameter "a" and "c" are obtained with applying the Least Square Method to equation (3.1) and (3.2):

$$\frac{1}{d^2} = \frac{4}{3}\frac{h^2 + k^2 + hk}{a^2} + \frac{l^2}{c^2} \qquad (3.1)$$

$$n\lambda = 2d\sin\theta \quad (3.2)$$

So, the unit volume of cell can be calculated using Eq. 3.3:

$$V = \frac{\sqrt{3}}{2}a^2c \quad (3.3)$$

Where λ is the wavelength of X-ray which is 1.5405 Å and θ is the half of angle where observed in strong XRD peak. The measurement and calculation results for all hexaferrites are listed in Table 3.2. According to the information given in the literature, the crystal structure of $BaFe_{12}O_{19}$ (ICDD- 39-1433) is hexagonal and its cell parameters a, b and c are 5.8945, 5.8945 and 23.2150 Å, respectively. The difference between the cell parameter of experiment and literature [133] is so small enough to be ignored and it may be seen from Table 3.2.

Table 3.2. Calculated cell parameters and unit volume from the XRD profile

	a A°)	c (A°)	V (10^{-28} m^3)
Ba	5.8895	23.2564	6.9860
Sr	5.8851	22.9585	6.8862
Pb	5.8887	23.1172	6.9423

3.1.2. SEM Analysis

The sizes and morphological structures of particles are determined by SEM images belonging to nanosized BaM hexaferrite samples. BaM hexaferrites synthesized at different PMMA/BaM ratios are shown in Figure 3.3. A slight PMMA polymers that not burned during the preparation of samples was observed. *The samples prepared using small amount of PMMA has a rod-shaped structure. They have around 200 nm in length and 40-50 nm in width*. While the amount of PMMA used during the reduction of Hexaferrite from micro to nanosize increases, the particles with mixed and different morphology arises. For instance, as PMMA/BaM ratio is 40/60, the

particles in the form of the rod and hexagonal plate structure are seen. The hexagonal plate structure has been found to be more dominant in the case of PMMA polymers used where the most intense. The synthesis condition is known that effects on the crystal growth at the hexaferrite samples. Where the gases are released by burning PMMA polymers. These releasing gases affects the shape, size and fragmentation of the BaM structure. The use of small amount of PMMA polymer lead the crystals having rod shaped nanoparticles that oriented with the c axis parallel to the plane of the grain. The orientation in the perpendicular direction of c axis occurred with increasing the PMMA polymer. This caused to create the product in the form of the hexagonal plate.

a) PMMA/BaM: 20/80 b) PMMA/BaM: 40/60 c) PMMA/BaM: 60/40

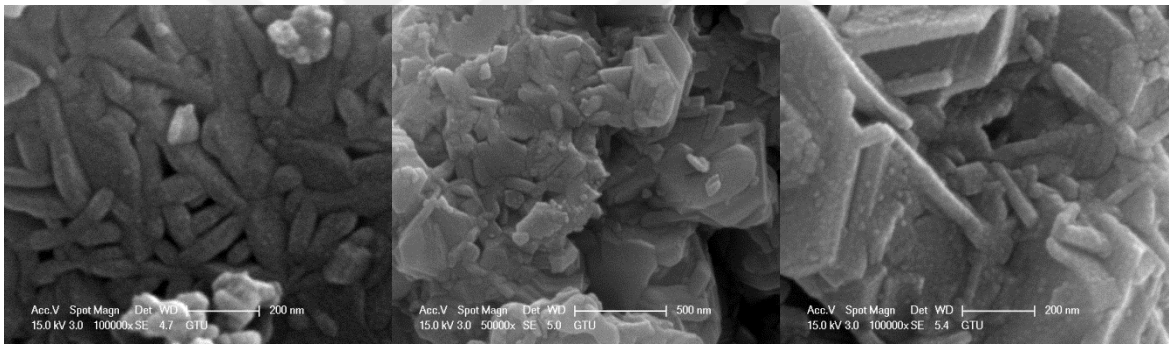


Figure 3.3. SEM images of samples prepared at different PMMA/BaM ratios.

3.1.3. VSM Analysis

The magnetic M-H (Magnetization-Magnetic Field) hysteresis loop related BaM hexaferrite nanoparticles are obtained by SQUID magnetometer at room temperature (shown in Figure 3.4). None of these curves could reach directly the saturation magnetization, despite applying high field magnetization such as 15 kOe. To obtain saturation magnetization, the extrapolation of these curves are used as 1/H goes to zero. Table 3.3 lists the values of saturation magnetization for PMMA/BaM Hexaferrites under 20/80, 40/60, 60/40 ratios: 67.79, 44.88 and 30.77 emu/g. (The material code for barium, strontium and lead hexaferride are given in Table 3.4.) The theoretical value of saturation magnetization M_s for BaM Hexaferrite is 72 emu/g

[134]. The most importance reason that the measured saturation magnetization smaller than 72 emu/g is related directly to their composition. While the amount of PMMA increases in the composition, the samples having lower specific saturation magnetization and coercivity are obtained.

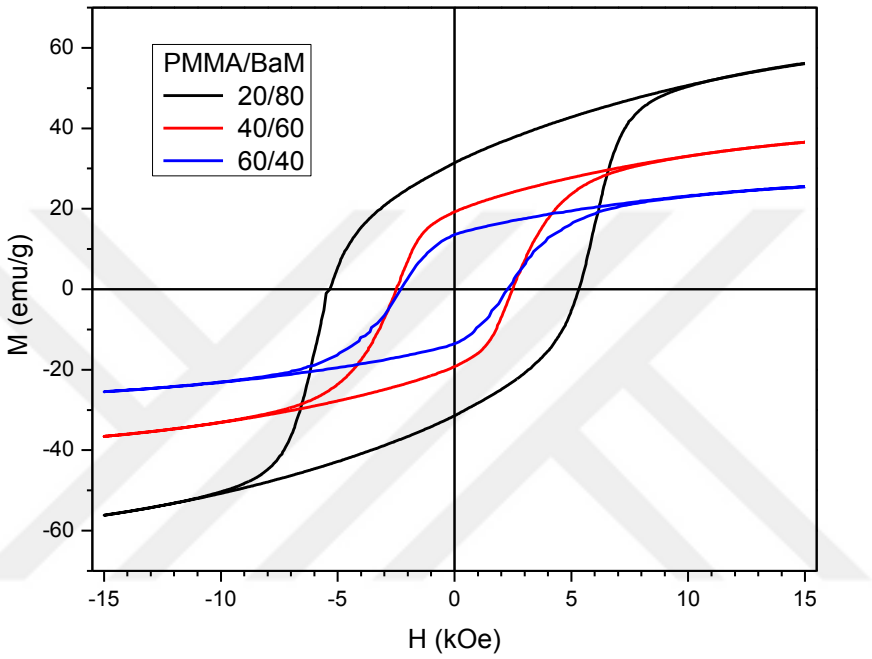


Figure 3.4. Hysteresis loop of produced BaM hexaferrites at room temperature.

According to the XRD and VSM datas, It is understood that the different phases are resulting from doped PMMA and these phases lead to poor magnetic properties .The presence of antiferromagnetic $BaFe_2O_4$ and non-ferromagnetic α-Fe_2O_3 peaks can be detected from the Figure 3.2 [135]. It can be understood that other ferrites occurred after the combustion process has an impact of reducing the total saturation magnetization and coercivity. The positive contribution of these different particle size and mixed phase to the microwave absorption performance will be discussed in the next sections. The different phases cannot be observed at the low PMMA/BaM ratios. Furthermore, the reason for not reaching the saturation magnetization in spite of high magnetic field can be expressed by Core/Shell dual structure. Because it is observed

that the core having magnetic properties is covered by non-magnetic thin shell. Thus, it becomes difficult to reach the saturation magnetization.

Table 3.3. Calculated $H_c, M_s, M_r, M_r/M_s$ values for BaM,SrM and PbM Hexaferrites with different PMMA ratios

	Hc (Oe)	Ms (emu/g)	Mr (emu/g)	Mr/Ms
Ba1	5321	67.79	36.55	0.46
Ba2	2490	44.88	23.68	0.42
Ba3	2271	30.77	16.52	0.43
Sr1	3493	40.29	21.89	0.45
Sr2	3662	37.68	20.67	0.45
Sr3	3377	23.52	13.45	0.44
Pb1	2077	51.43	26.75	0.42
Pb2	1160	34.94	18.05	0.39
Pb3	1154	27.77	14.46	0.36

Table 3.4. Material codes of synthesized hexaferrites and their PMMA ratios

Material Code		PMMA/Hexaferrite
Ba1	BaFe12O19	20/80
Ba2		40/60
Ba3		60/40
Sr1	SrFe12O19	20/80
Sr2		40/60
Sr3		60/40
Pb1	PbFe12O19	20/80
Pb2		40/60
Pb3		60/40

Figure 3.5 shows the graph of the saturation magnetization M_s , permenant magnetization M_r , coercive field H_c and squareness ratio M_r/M_s for each

synthesized hexaferrites. The x axis shows the PMMA ratio in terms of percentage. From the figure, we see that the saturation magnetization value decreases with increasing PMMA ratio. The coercivity decreases rapidly except for SrM hexaferrite. However, coercive field decreases slowly after %40 amount of PMMA. The permanent magnetization has a decreasing trend for all samples. BaM and SrM samples have larger the squareness ratio. They nearly doesn't change with increasing the amount of PMMA. But the squareness ratio of PbM sample decreases linearly.

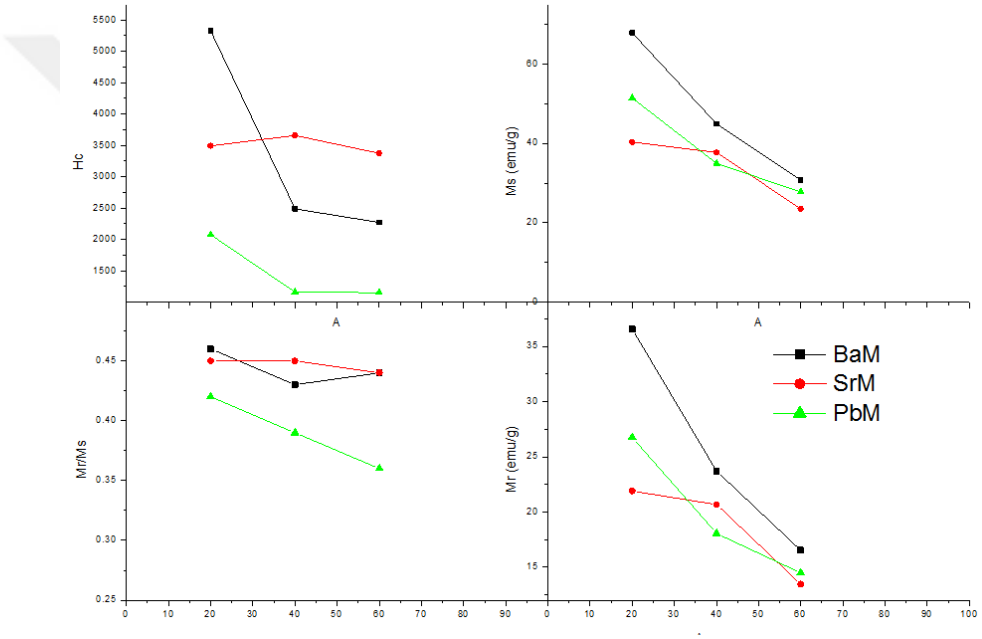


Figure 3.5. Plots of the saturation magnetization M_s, permenant magnetization M_r, coercive field H_c and squareness ratio M_r/M_s for each type hexaferrite samples

3.1.4. FMR Results

Figure 3.6 shows the FMR spectra of BaM hexaferrite nanopowders. The spectrum of sample Ba1 and Ba3 shows a symmetrical and intense FMR line with a resonance field at $H_r = 13763, 13232$ Oe, respectively. The peak-to-peak linewidth ΔH_{pp} is

3635 and 3916 Oe. The FMR line of Ba2 is found to be relatively low. The FMR values of Ba2 are 13813 Oe for H_r and 3575 Oe for ΔH_{pp}.

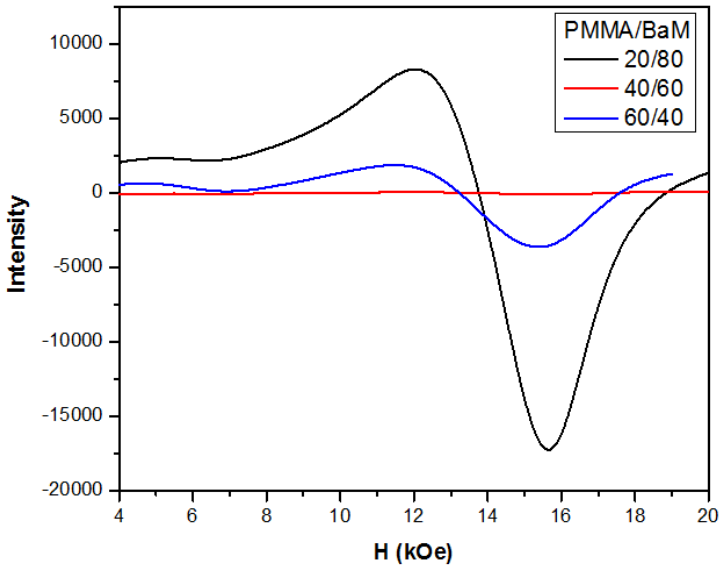


Figure 3.6. FMR curves of BaM Hexaferrite powders

3.1.5. Microwave Dielectric and Magnetic Properties

The frequence dependence of complex permittivity ε and permeability μ is observed for the BaM composites with 20/40/60 PMMA ratio, as shown in the Figure 7-8-9. The frequence dependence graph of $BaFe_{12}O_{19}$ is given in the literature [136]. In our study, they were investigated in the frequency range of 2-18 GHz. The thickness of Ba1, Ba2 and Ba3 sample is 3mm. The left and right side in these figures shows permittivity and permeability curves, respectively. Each samples exhibits dielectric resonance behavior at around 15 GHz. It can be seen that the resonance peaks for ε' and ε'' corresponds to the same frequency point. As the concentration of PMMA increases, the resonance frequency doesn't shift to lower or higher frequency. But the magnitude of resonance peak is large in the case of much PMMA. The real permittivity of Ba1 sample slowly decreases with the function of frequency and its complex permittivity is almost constant except for the point of resonance frequency.

For all of BaM samples, the real part of permittivity and permeability are much larger than the imaginary parts in the whole frequency range. Except for the resonance frequency, the real permittivity of Ba2 and Ba3 sample remains almost constant. In general, the real permittivity ε' decreases slightly while the concentration of PMMA increases. The sample of Ba3 exhibits dramatic increase in imaginary permittivity. For all sample, the imaginary part of permeability possess little fluctuation. The imaginary permeability of Ba2 and Ba3 is relatively high at frequencies between 3 and 4 GHz and then it decreases slowly. The resonance peaks are occurring at higher frequency for Ba3 sample.

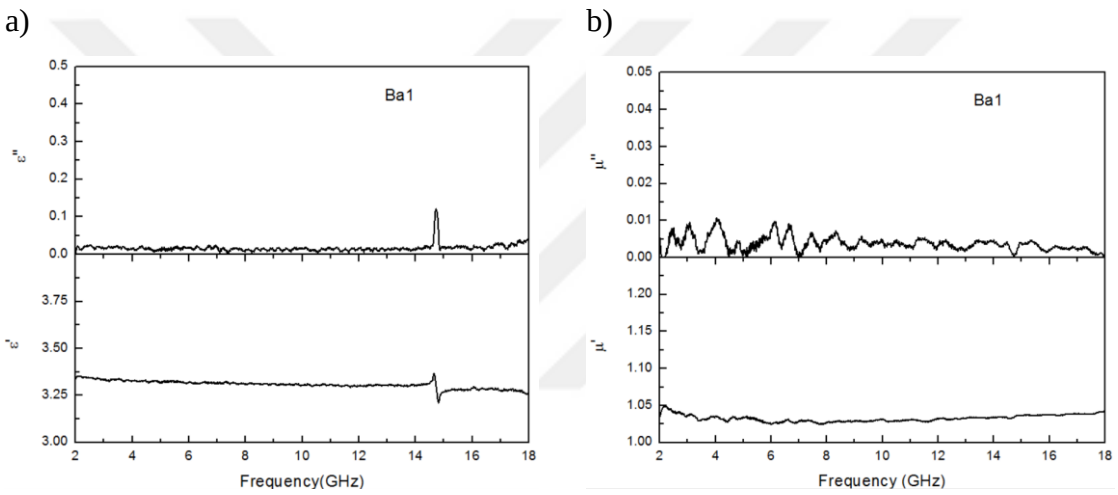


Figure 3.7. Dielectric permittivity (a) and magnetic permeability (b) curves of Ba1

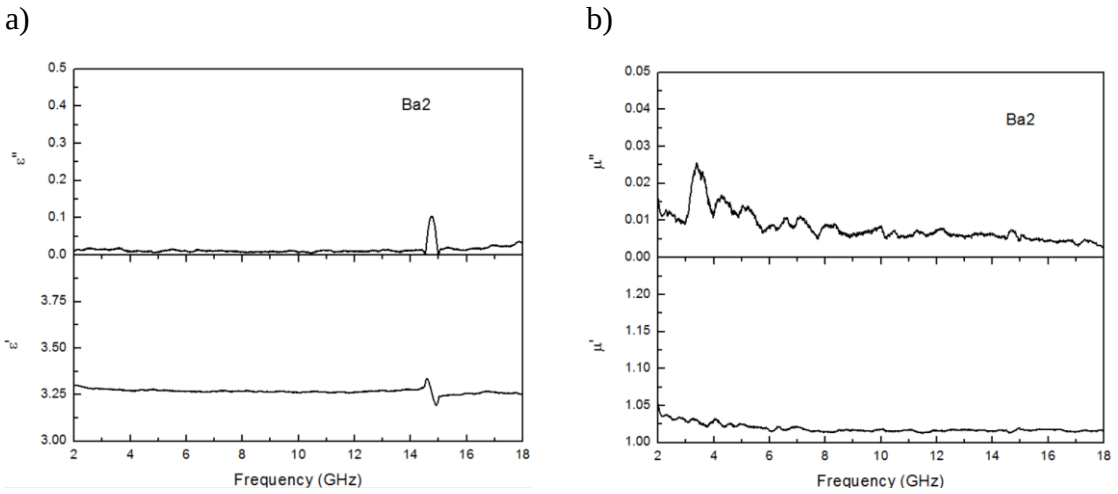


Figure 3.8. Dielectric permittivity (a) and magnetic permeability (b) curves of Ba2.

a) b)

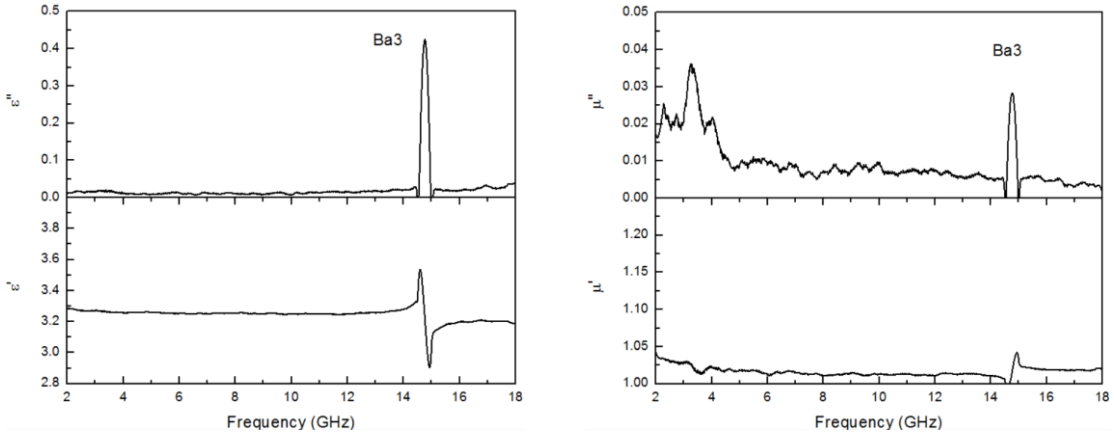


Figure 3.9. Dielectric permittivity (a) and magnetic permeability (b) curves of Ba3.

The scattering parameter of S11 and S21 of all BaM toroidal samples were measured by PNA E8364B vector network analyzer. Figure 3.10 shows the scattering parameter of S11 with black line and the scattering parameter of S21 with red line. The behavior of scattering parameter of three samples is similar. The small resonance peak occurs at around 14.75 GHz. This resonance peak is compatible with the one occurred at the permittivity and permeability curve. That is, the scattering parameter, the permittivity and permeability plots have the resonance frequency at the same point of frequency. At the beginning, the parameter S11 increases up to 14 GHz and then it decreases up to 18 GHz. On the contrary, the parameter S21 decreases up to 14 GHz and then it increases up to 18 GHz. It can be seen clearly, the parameter S11 and S21 have the opposite tendency. While the parameter S11 increases, the parameter S21 decreases. However, the linewidth and magnitude of resonance peak occurred at between 14-15 GHz is very small. The resonance frequency shifts slightly to the high frequency and the magnitude of peak are getting strong while the concentration of PMMA increases.

a) b) c)

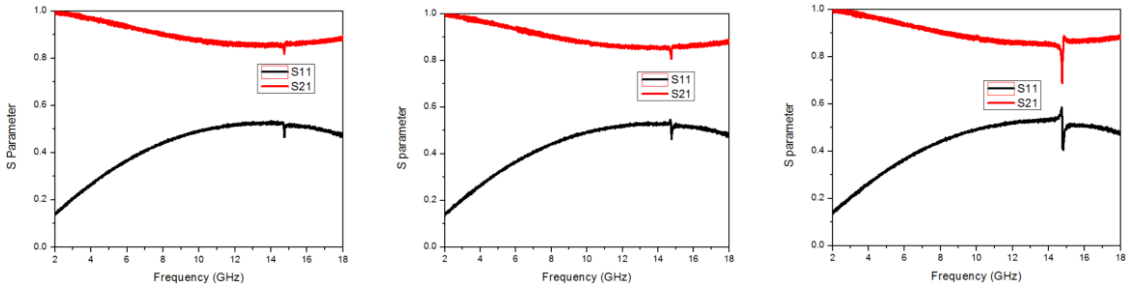


Figure 3.10. Scattering parameters S11, S21 for Ba1 (a) , Ba2 (b), Ba3 (c) in the frequency range between 2-18 GHz.

The reflection ($R=|S11|^2$) and transmission ($T=|S21|^2$) coefficient are calculated from the scattering parameter and given below in Figure 3.11. For all samples, the reflection coefficient is around a percentage of 28 at 14 GHz and the transmission coefficient is around a percentage of 72 at 14 GHz. The absorption coefficient ($A=1-R-T$) calculated from the reflection (R) and transmission (T) coefficient is nearly zero except for the frequency at resonance. At the resonance frequency, the percentage of absorption for Ba1, Ba2 and Ba3 is 11.3, 12.8 and 28 ,respectively.

a) b) c)

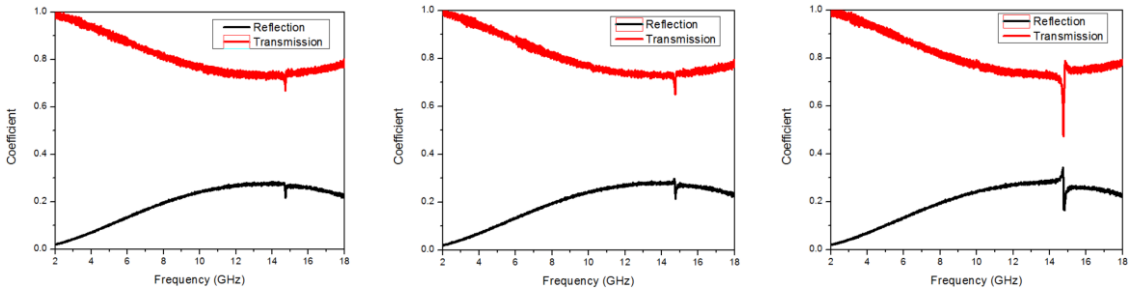


Figure 3.11. Reflection (R) and Transmission (T) coefficients for Ba1 (a) , Ba2 (b), Ba3 (c) in the range frequency range between 2-18 GHz.

3.2. SrM Nanopowders Coated with PMMA

3.2.1. XRD Analysis

The XRD profiles of produced SrM hexaferrites show that their crystal structure are consistent with $SrFe_{12}O_{19}$ (ICDD-33-1340) structure. Figure 3.12 gives the miller indices (hkl): (006), (110), (008), (107), (114), (200), (201), (108), (203), (116), (205), (206), (1011), (2010), (300), (0014), (304), (2011), (1112), (218), (2012), (220), (2014), (1017), (228) ve (317). The peaks marked with "*" indicates the presence of different phase structure. The same process used in the previous section is applied on the SrM hexaferrites. The hexaferrite powders synthesized using sol-gel method are mixed with PMMA polymer. These polymers are added to the SrM hexaferrites at the percent of 20, 40, 60 ratios. It is observed that the different phases occur obviously with increasing amount of PMMA. These phases are resulting from the antiferromagnetic $SrFe_2O_4$ and non-ferromagnetic α-Fe_2O_3 structures. We can say that the PMMA polymers exploded by heating process causes to reduce the micro size hexaferrite particle to the nano size [132].

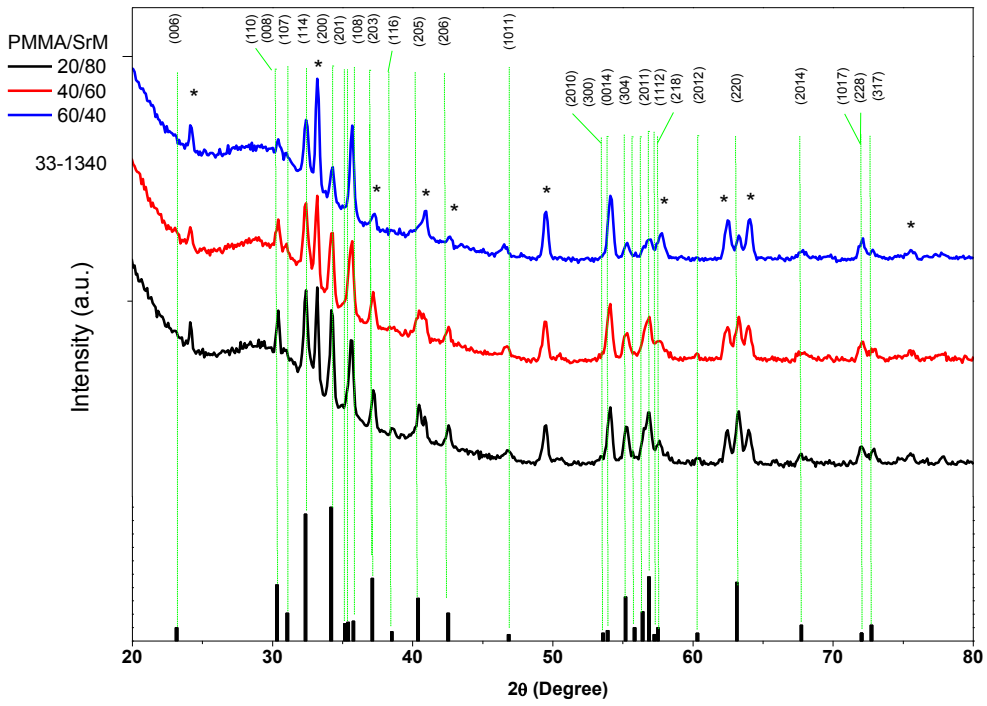


Figure 3.12 XRD pattern of SrM hexaferrites with 20/40/60 PMMA ratios.

Table 3.5. 2θ values, (hkl) indices and the calculated distance between planes obtained XRD profile for SrM hexaferrite powders

h	k	l	2θ	d (Å)
0	0	7	32,32	2,77
1	1	4	34,23	2,62
2	0	3	37,16	2,42
2	0	5	40,45	2,23
1	0	11	46,84	1,94
2	1	7	55,2	1,66
2	0	11	56,88	1,62
2	2	0	63,29	1,47
2	0	14	67,73	1,38
1	0	17	72,08	1,31

The (hkl) indice values of SrM nanohexaferrite powder and the diffraction angles are given in Table 3.5. The cell parameters and unit volume of SrM hexaferrite are calculated and listed in Table 3.2. The crystal structure of $SrFe_{12}O_{19}$ (ICDD-33-1340) is hexagonal and its cell parameters a, b and c are 5.8868, 5.8868 and 23.0370 Å, respectively. Because the small difference between experiment and literature cell parameters, these experimental values can be acceptable to belong to cell of SrM hexaferrite particle. While the amount of PMMA increases, the other ferrites such as magnetite and maghemite occur.

3.2.2 SEM Analysis

The geometric size and morphological dimension of particles are determined by evaluating the SEM images (Figure 3.13). The result from the images indicates: the sample which has 20/80 of PMMA/SrM ratio is the mixed structure as spherical, rod and hexagonal. The SEM image for sample SrM hexaferrite having 40/60 ratio shows two types of shape such as spherical and hexagonal. In addition to these, the size of these particles changes with increasing PMMA ratio and exhibits cluster and

agglomerate morphology. The hexagonal structure is also dominant at the sample contained the much PMMA.

a) PMMA/SrM: 20/80 b) PMMA/SrM: 40/60 c) PMMA/SrM: 60/40

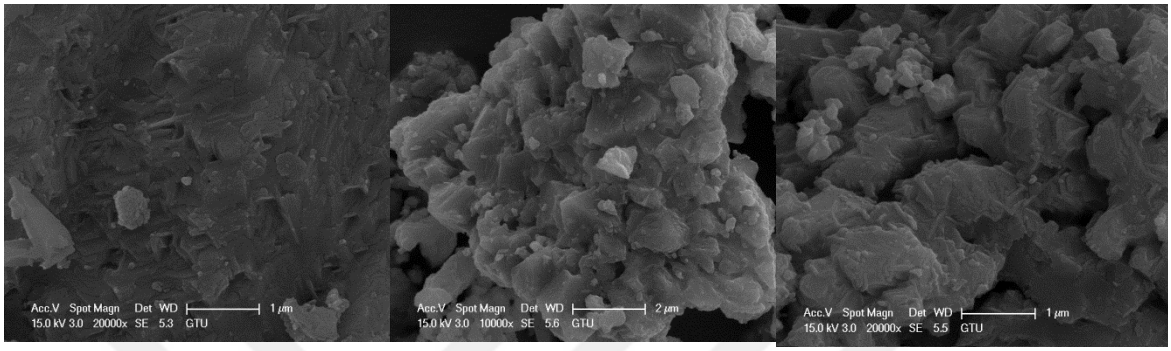


Figure 3.13. SEM images of samples prepared at different PMMA/SrM ratios.

3.2.3 VSM Analysis

The DC magnetic characteristics of bulk nanohexaferrite SrM at room temperature are examined by using SQUID magnetometer in the range ±15 kOe. The hysteresis loop is shown in Figure 3.14. The saturation magnetization M_s calculated from the extrapolation that 1/H goes zero are 40.29, 37.68 and 23.52 emu/g. In the literature, the values of saturation magnetization of single crystal SrM hexaferrite are in the range from 74.3 to 92.6 emu/g [137]. The decreasing the saturation magnetization is seen in the same way as the sample of BaM hexaferrites. The reason for decreasing in the magnetization may be that it depends on the composition. Thus, it cannot reach the saturation magnetization, despite the high magnetic field such as 15 kOe. The other magnetic properties obtained from the hysteresis curve are listed in Table 3.3. It can be seen from the table, as the permanent magnetisation M_r , the saturation magnetization M_s and the squareness ratio M_r/M_s values decreases with increasing PMMA ratio, the coercive field H_c is larger for Sr2 sample. The coercive field value is proportional to the particle size and it has very high value of about 3.5 kOe. This value points out that the particle size is smaller than 1 μm that is the limit of single domain particle [138]. Furthermore, the results found in BaM hexaferrite and XRD

profile show that the presence of different structures such as Sr spinel ferrite and hematite diminish the saturation magnetization significantly.

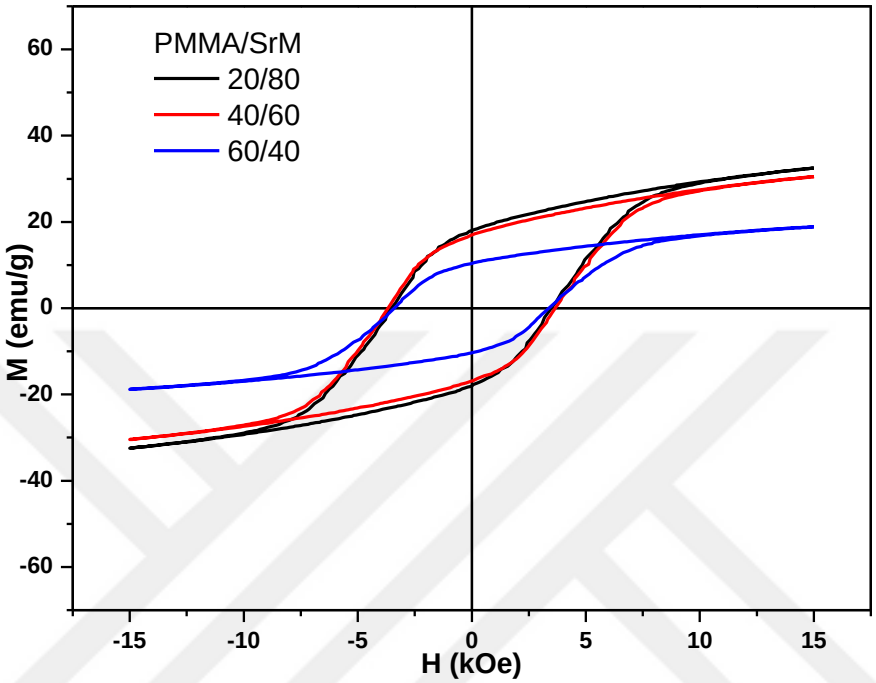


Figure 3.14. Hysteresis loop of produced SrM hexaferrites at room temperature.

3.2.4. FMR Results

Figure 3.15 shows the FMR spectra of SrM hexaferrite nanopowders. The spectrum of sample Sr1 presents a symmetrical and intense FMR line. The resonance fields of all sample (Sr1, Sr2, Sr3) are H_r =15465, 15639, 15777 Oe, respectively. The peak-to-peak linewidth ΔH_{pp} are 4299, 4197 and 4335 Oe. The peak of linewidth is strong in the case of small additions of PMMA. When the ratio of PMMA increases, the peak intensity decreases dramatically.

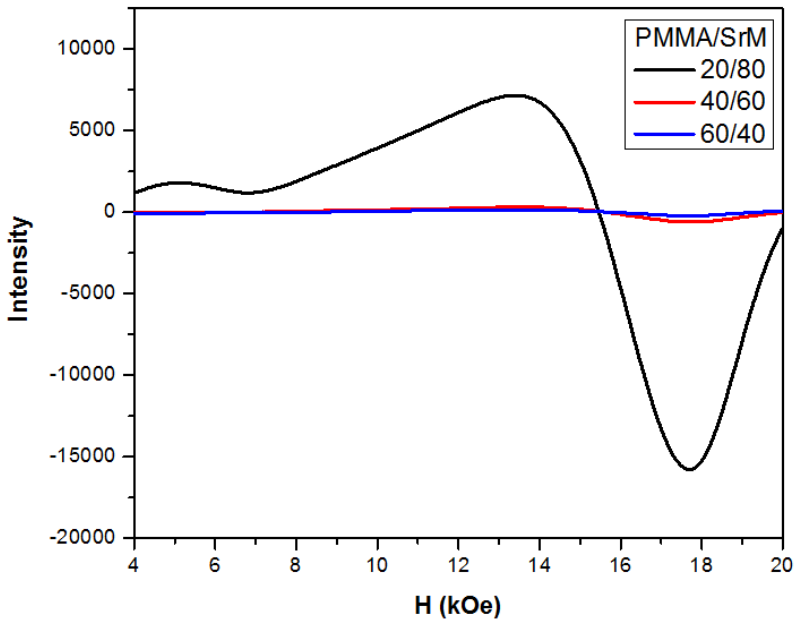


Figure 3.15. FMR curves of SrM Hexaferrite powders

3.2.5. Microwave Dielectric and Magnetic Properties

The microwave absorption properties were investigated in the frequency range 2-18 GHz for Sr1, Sr2 and Sr3 samples, as shown in Figure 3.16. The thickness of samples is 3mm and they made of the mixture of SrM nanopowder and paraffin wax as toroid shape. The left side of Figure 3.16 shows the dielectric permittivity and right side shows the magnetic permeability. Each sample exhibits the dielectric and magnetic resonance at around 14 GHz. The values of frequency corresponding to the resonance peak of ε' and ε'' are same. We look Figure 3.16 (a) and (b), the magnitude of peak for real and imaginary part becomes larger relatively when the concentration of PMMA is %20. But it diminishes dramatically in the case of Sr3 sample. The resonance peak of real part and imaginary part of it is very little. However the frequency is almost same with the one observed in Sr1 and Sr2 sample. The values of permittivity and permeability belonging to all samples are almost constant with increasing frequency except for the peak of resonance. We see that the real and imaginary part of permeability are almost flat in the all frequency range, as shown in Figure 3.16 (f).

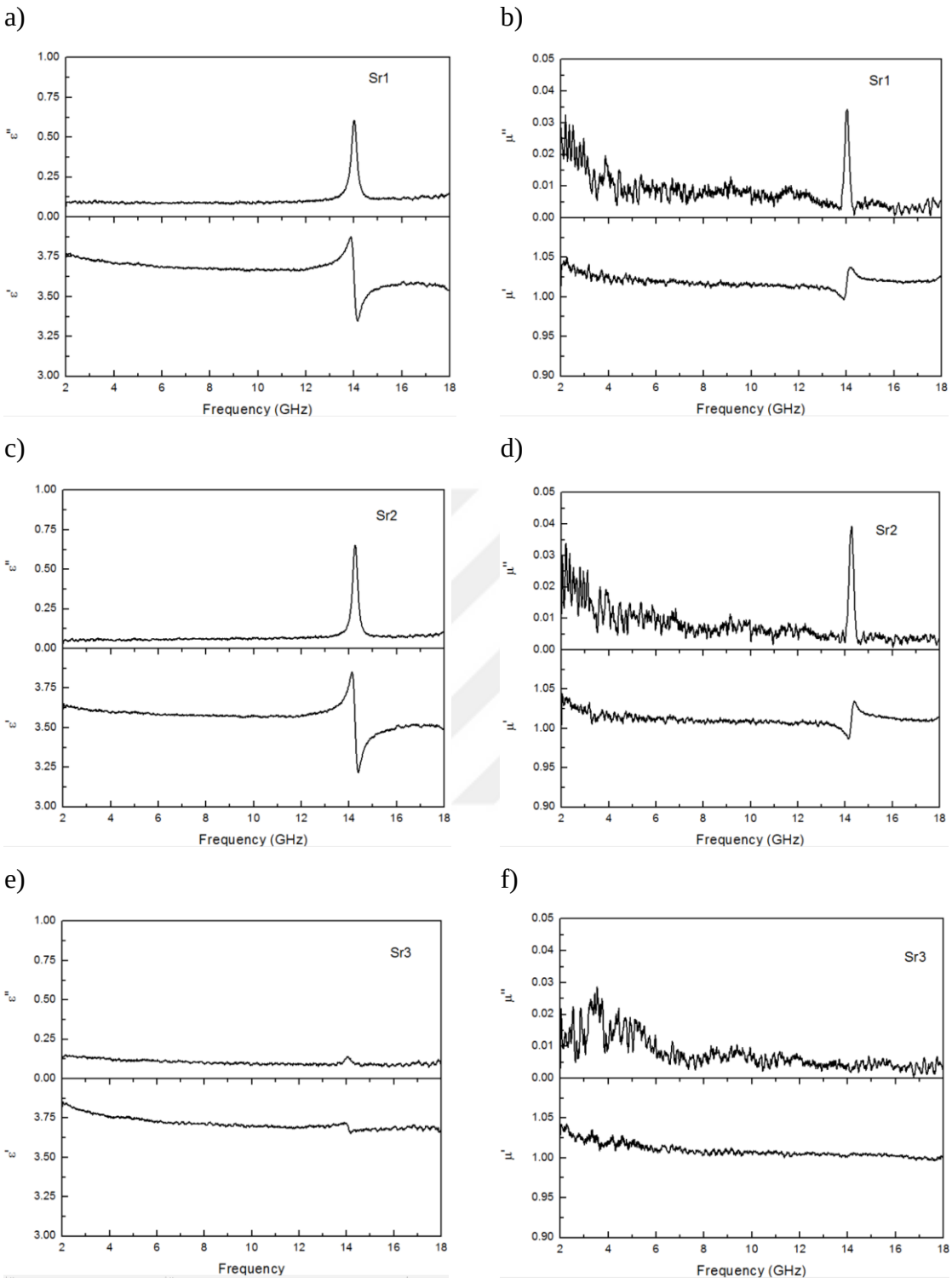


Figure 3.16. Complex dielectric permittivity and permeability including real and imaginary part. The permittivity (a) and permeability (b) for Sr1, permittivity (c) and permeability (d) for Sr2, permittivity (e) and permeability (f) for Sr3.

Figure 3.17 shows the scattering curve of SrM samples measured with PNA vector network analyzer. Except for the Figure 3.17 (c), these plots have a small resonance peak. The values of scattering parameters of Sr1, Sr2 and Sr3 are close to each other. The S parameters of SrM sample behaves very similar to the one of BaM samples. It can be seen that the resonance peak occurs at around 14 GHz for first two samples. From Sr1 to Sr2, the frequency of resonance shifts slightly to high frequency. However, the sample Sr3 has no resonance peak. In generally, we can say for all samples that the parameter S21 decreases up to near 14 GHz and then it increases up to the end point of spectrum. On the contrary, the parameter S11 increases up to near 14 GHz and then it decreases generally up to 18 GHz.

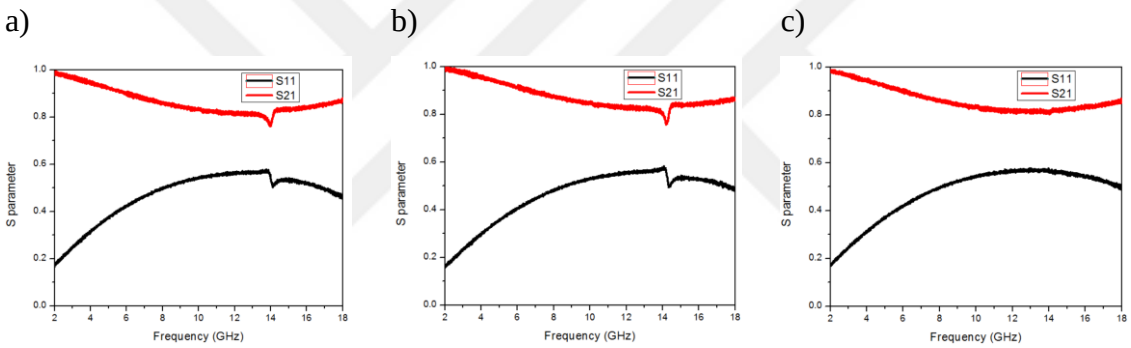


Figure 3.17. Scattering parameters S11, S21 for Sr1 (a), Sr2 (b), Sr3 (c) in the range frequency range between 2-18 GHz.

The reflection (R) and transmission (T) coefficient of SrM samples are given in Figure 3.18. Taking into account Sr1 sample, the percentage of transmission coefficient (T) is 58 and the percentage of reflection coefficient (R) is 28 at the resonance point. Therefore, the percentage of the absorption is 14 at this point. For other frequency poinst, its percentage ranges over the interval (%1-5). Comparing with R/T coefficients of BaM and SrM samples, the largest absorption rate is obtained with Sr3 sample. We observe that the percentages of absorption of first and second sample are almost same. However, the absorption rate increases in the third sample.

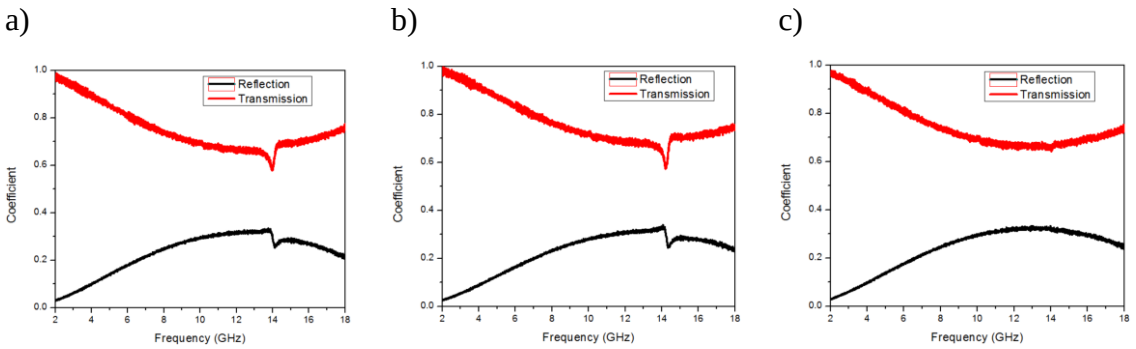


Figure 3.18. Reflection (R) and Transmission (T) coefficients for Sr1 (a), Sr2 (b), Sr3 (c) in the range frequency range between 2-18 GHz.

3.3. PbM Nanopowders Coated with PMMA

3.3.1. XRD Analysis

The X-ray diffraction belonging to $PbFe_{12}O_{19}$ hexaferrite series are shown in Figure 3.19. It is identified that the observed peaks are compatible with $PbFe_{12}O_{19}$ (ICDD–41-1373) datas. All miller indices are (006), (104), (110), (008), (112), (107), (114), (200), (108), (202), (109), (205), (206), (1011), (209), (300), (217), (303), (0014), (302), (2011), (1012), (220), (1015), (308), (2014) and (317). As we mentioned earlier, the marked peak "*" identify to exist different phases such as $PbFe_2O_4$ and α-Fe_2O_3. It can be seen from the figure, these phases arises apparently as the amount of PMMA increases. The positions of these peaks are compatible with each other. Table 3.6 shows the calculated distance between planes and the angle 2θ where the XRD peaks are strong. The cell parameter (a, c) and unit volume of PbM hexaferrite were listed in Table 3.2. In the literature, the crystal structure of $PbFe_{12}O_{19}$ (ICDD – 41-1373) is given in the hexagonal structure. Its cell parameter a, c and volume are 5.8945, 5.8945 and 23.0900 Å, respectively.

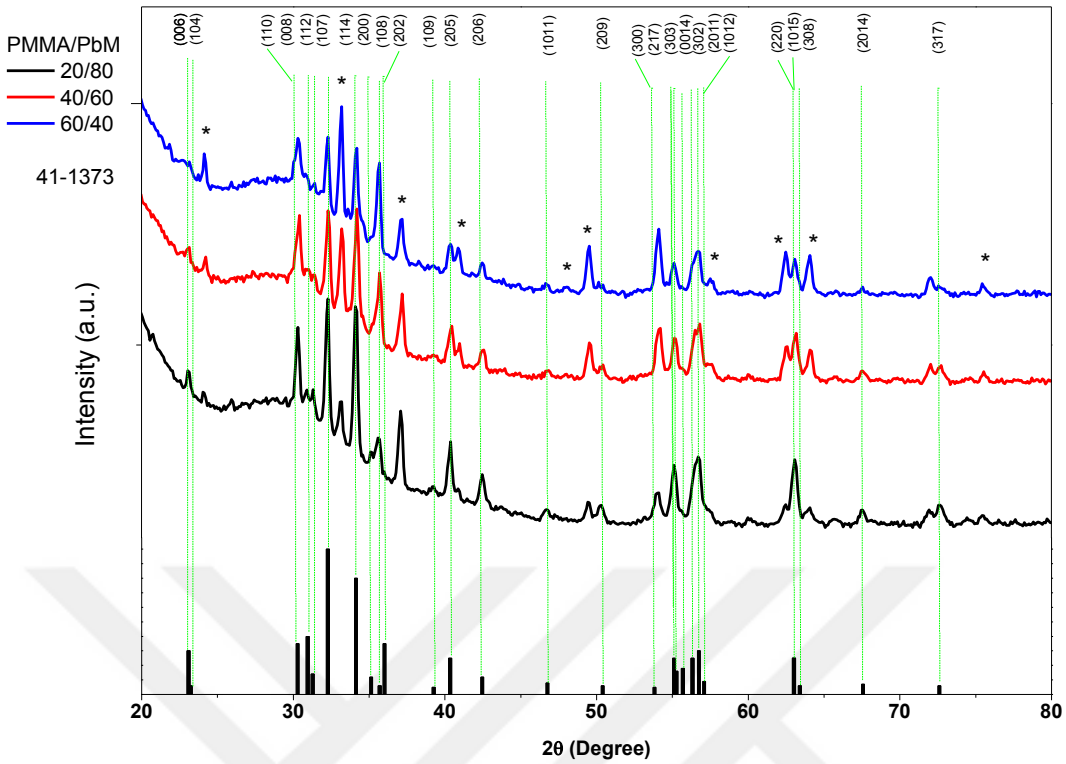


Figure 3.19. XRD pattern of PbM hexaferrites with 20/40/60 PMMA ratios.

Table 3.6. 2θ values, (hkl) indices and the calculated distance between planes obtained XRD profile for PbM hexaferrite powders

	k	l	2θ	d (Å)
0	0	6	23,06	3,85
1	1	0	30,35	2,94
1	0	7	32,31	2,77
1	1	4	34,09	2,63
1	0	8	35,65	2,52
2	0	5	40,40	2,23
2	0	6	42,45	2,13
2	1	7	55,11	1,67
2	0	11	56,70	1,62
2	2	0	63,08	1,47
2	0	14	67,53	1,39
3	1	7	72,68	1,30

3.3.2 SEM Analysis

The morphology and size of the PbM nanohexaferrite are determined by their SEM images which are given in Figure 3.20. It is observed that some parts of PMMA polymer has not fired. The size of particle for Pb1 sample is about 100-400 nm. There is the mixture structure of rod and spherical shape in it. As the ratio of PMMA/PbM value is 40/60, the hexagonal and rod shaped structure emerge. As this ratio is 60/40, it is observed that the hexagonal plate is dominant. It is not possible to mention about a certain morphology because of the broad particle size, clustering and diversity of particle.

a) PMMA/PbM: 20/80 b) PMMA/PbM: 40/60 c) PMMA/PbM: 60/40

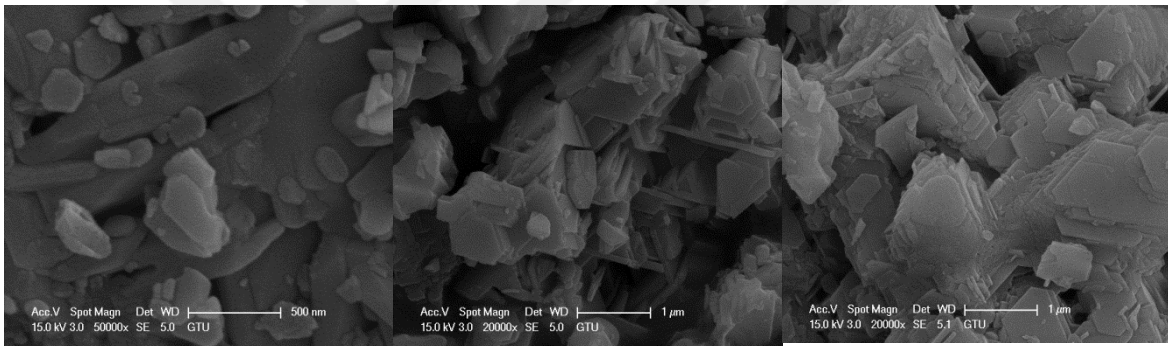


Figure 3.20. SEM images of samples prepared at different PMMA/PbM ratios.

3.3.3. VSM Analysis

The hysteresis curves of PbM hexaferrite powder are shown in Figure 3.21. The SQUID magnetometer are used in room temperature to get the VSM datas. The curves cannot reach the saturation magnetization, as can be seen from the figure. The different phases such as antiferromagnetic $PbFe_2O_4$ and non-ferromagnetic α-Fe_2O_3 structures occur and PMMA polymer causes to form diamagnetic shell on the surface. So that they are preventing it to reach the saturation magnetization. The value of saturation magnetization M_s obtained from the extrapolation as 1/H goes to zero are 51.43, 34.94 and 27.77 emu/g. The saturation magnetization becomes less, as the PMMA ratio is increased further. The saturation magnetization is less than the value

of 54 emu/g [139] having pure PbM hexaferrite because it depends on the composition.

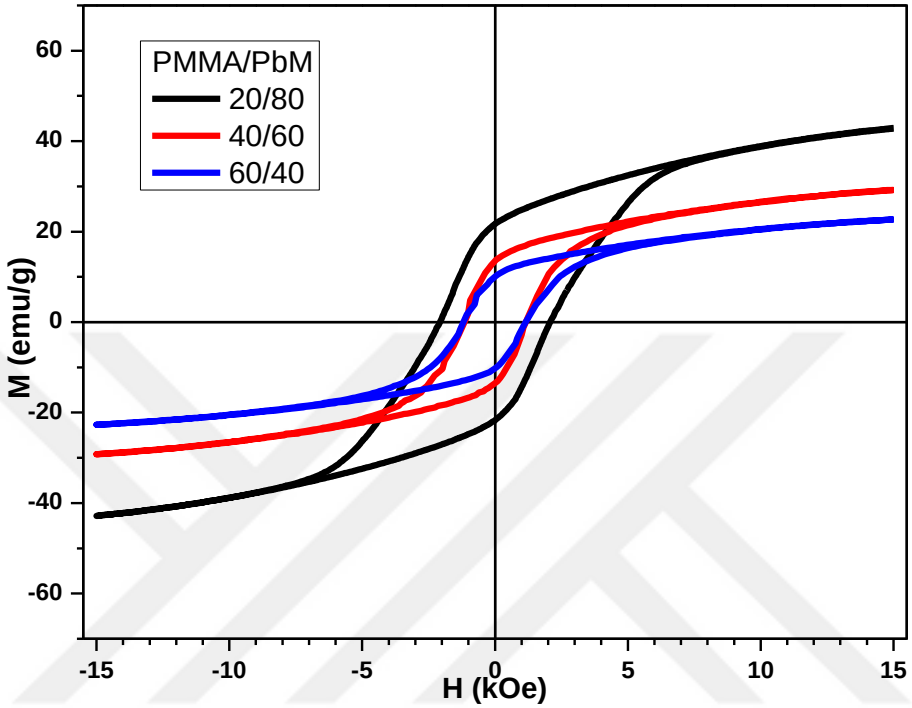


Figure 3.21. Hysteresis loop of produced PbM hexaferrites at room temperature.

3.3.4. FMR Results

Figure 3.22 shows the FMR spectra of PbM hexaferrite nanopowders. The spectrum of all sample shows a symmetrical and intense FMR line .The magnitude of Pb1 peak is quite strong. The resonance fields are $H_r = 13598,\ 13518,\ 13594$ Oe, respectively. The peak-to-peak linewidth ΔH_{pp} are 3125, 4008 and 3752 Oe. As can be seen from the figure, the ΔH_{pp} expands on the Pb2 sample. But their resonance fields are almost the same. As before, the peak of linewidth are strong in the case of small additions of PMMA. When the ratio of PMMA increases, the peak intensity decreases.

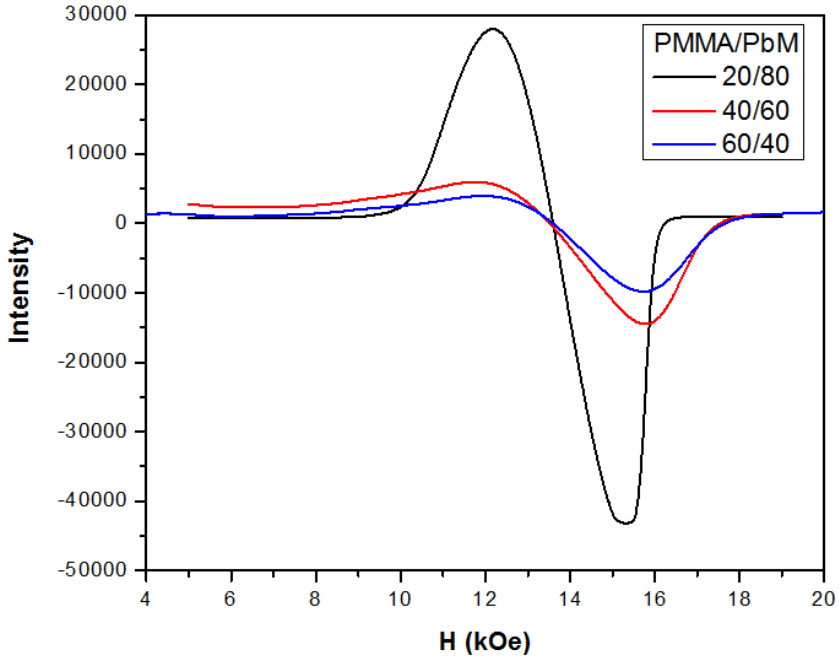


Figure 3.22. FMR curves of PbM Hexaferrite powders

3.3.5. Microwave Dielectric and Magnetic Properties

The complex permeability and permittivity belonging to PbM sample were investigated in the frequency range 2-18 GHz, as shown in Figure 3.22-3.23-3.24. Each plot contains real and imaginary part of permeability or permittivity. The resonance peak of real or imaginary part occurs at around 14 GHz. The maximum peak-to-peak amplitude of real part of the permittivity for Pb1, Pb2 and Pb3 are approximately 2.5, 0.3 and 1.1, respectively. As the peak-to-peak amplitude is maximum in the case of 20/80 of PMMA/PbM ratio, it becomes to minimum for the sample which has 40/60 of PMMA/PbM. The linewidth of permittivity for PbM series are 23, 12 and 16 MHz at around 14 GHz. Similarly, as the linewidth is maximum for Pb1 sample, it becomes to minimum for Pb2 sample. However, when the PMMA ratio increases, the permittivity curves show the resonance toward to higher frequencies. Therefore, except for the resonance frequencies, the values of permittivity decrease with increasing the PMMA/PbM ratio. The frequency corresponding to resonance peak of imaginary part at the permittivity plot coincide with the one of real part. As the resonance peak is very strong at the Pb1 sample, it is very weak at the Pb2 sample. It can be seen from Figure 3.23-24-25(b), the real and

imaginary part perform fluctuation at the beginning of the spectrum. Then they perform relatively smooth curve up to the resonance. The resonance peaks of Pb1 sample is larger than the others. This can cause the reflection loss to be maximum at the resonance frequency. The permittivity ε_r is much larger than permeability μ_r in the same way as in the case of BaM and SrM series. This causes that the small part of electromagnetic wave can enter form air to inside of absorber. To maximize the electromagnetic wave entered inside the absorber, the values of permittivity and permeability must be close each other [140].

a) b)

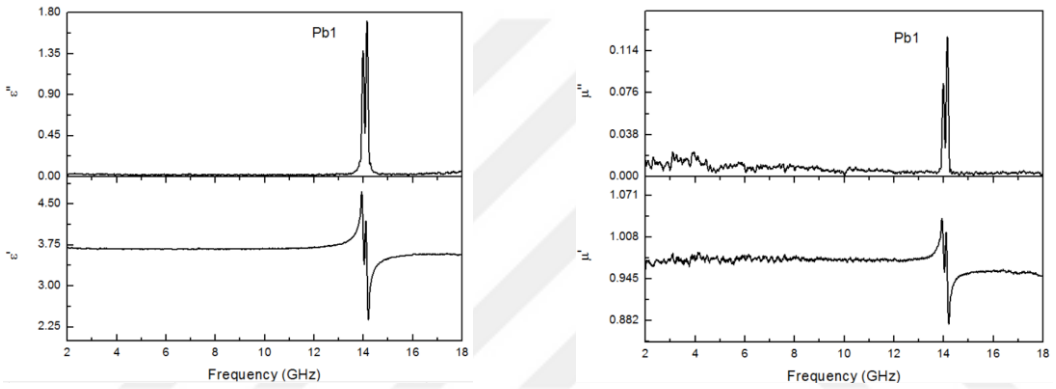


Figure 3.23. Complex dielectric permittivity (a) and permeability (b) of Pb1 including real and imaginary part.

a) b)

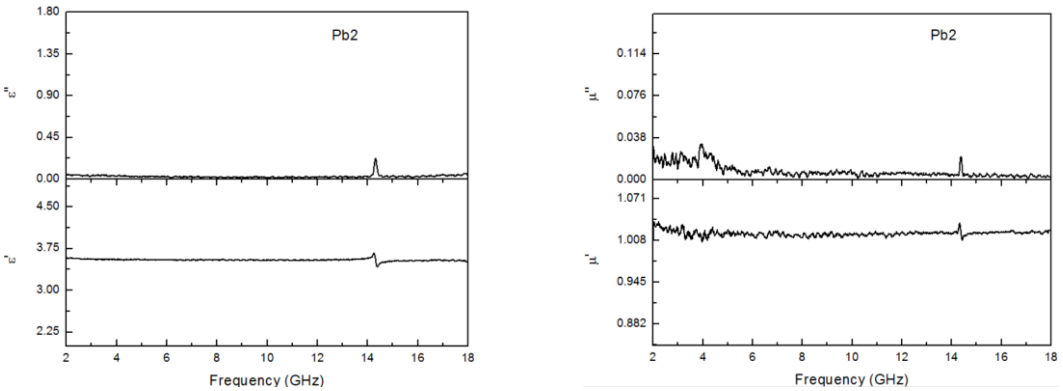


Figure 3.24. Complex dielectric permittivity (a) and permeability (b) of Pb2 including real and imaginary part.

a) b)

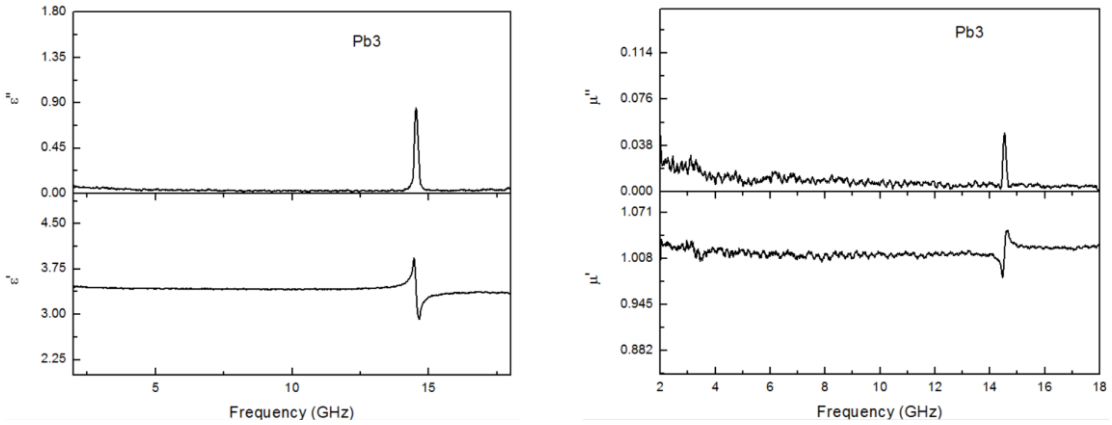


Figure 3.25. Complex dielectric permittivity (a) and permeability (b) of Pb2

The scattering parameter of S11 and S21 for PbM series were measured in the range of 2-18 GHz, as shown in Figure 3.26. As expected, the Pb1 sample has the lowest value of S11 and S21 at the resonance frequency because of its dielectric and magnetic behavior. In general, we can say for all plot of S parameter: the parameter S21 decreases from 2 to 14 GHz and increases from 14 to 18 GHz. On the contrary, the parameter S11 increases from 2 to 14 GHz and decreases from 14 to 18 GHz. The plot of Pb2 sample has very small resonance as expected for dielectric and magnetic parameter. Because these parameters are derived from the parameter of S11 and S21.

a) b) c)

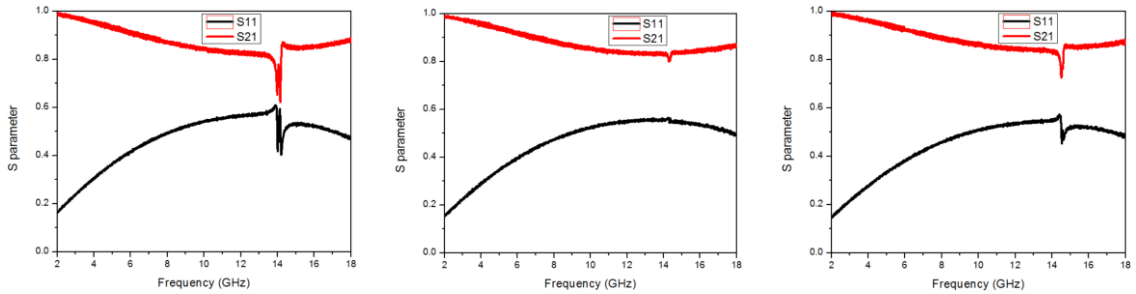


Figure 3.26 Scattering parameters S11, S21 for Pb1 (a) , Pb2 (b), Pb3 (c) in the range frequency range between 2-18 GHz.

The reflection (R) and transmission (T) coefficient of PbM series are shown in Figure 3.27. Total number of point in the measurement is 1601. There exists small split in the

resonance curve of Pb1 sample because of using much measurement points. We note that the parameter of S11 and S21 fall sharply at the same time. Table 3.7 shows the absorption rate in terms of percentage. The absorption rate doesn't change linearly with PMMA ratio. At the Pb1 sample, it has the largest value. But it has the lowest value for Pb2 sample.

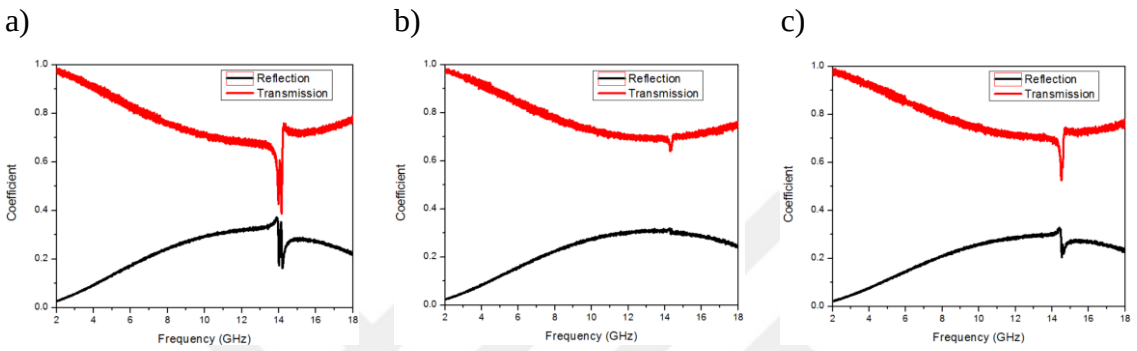


Figure 3.27. Reflection (R) and Transmission (T) coefficients for Pb1 (a) , Pb2 (b), Pb3 (c) in the range frequency range between 2-18 GHz.

Table 3.7. Absorption rate in terms of percentage and the resonance frequency of PbM series

	Pb1	Pb2	Pb3
Absorption rate (%)	34.4	6	25
The resonance frequency (GHz)	14	14.32	14.53

3.4 Micro-Sized Magnetic and Non-magnetic Powder

3.4.1 Bulk Rectangular Sample

The frequency dependence between 12.4 and 18 GHz on the real part of permittivity and loss tangent of C, CFeNi, Fe, FeNi, Ni micropowder samples are sown in Figure 3.28. As the value of ε' of C, CFeNi, FeNi, Ni samples decrease gradually with

increasing frequency, the ε' of Fe sample remain almost constant over the whole measured frequency. The ε' of Ni shows a faster decrease between 12.4 and 13.5 GHz and then it decrease gradually with frequency. The dielectric constant ε' value of C, Fe, Ni range between 4.8 and 2.3, 7.55 and 7.5, 17.4 and 10.1, respectively. However, the ε' value of CFeNi mixture ranges between 26.5 and 24. It is obviously that mixing the materials of C, Fe and Ni effect to increase the real part of permittivity. The sample of CFeNi exhibits higher value of ε' than the other samples in the frequency range between 12.4 and 18 GHz. As shown in Figure 3.28, the FeNi sample takes dielectric constant value between that of Ni and Fe. However, the value of ε' of FeNi comes close to Fe sample at the high frequency.

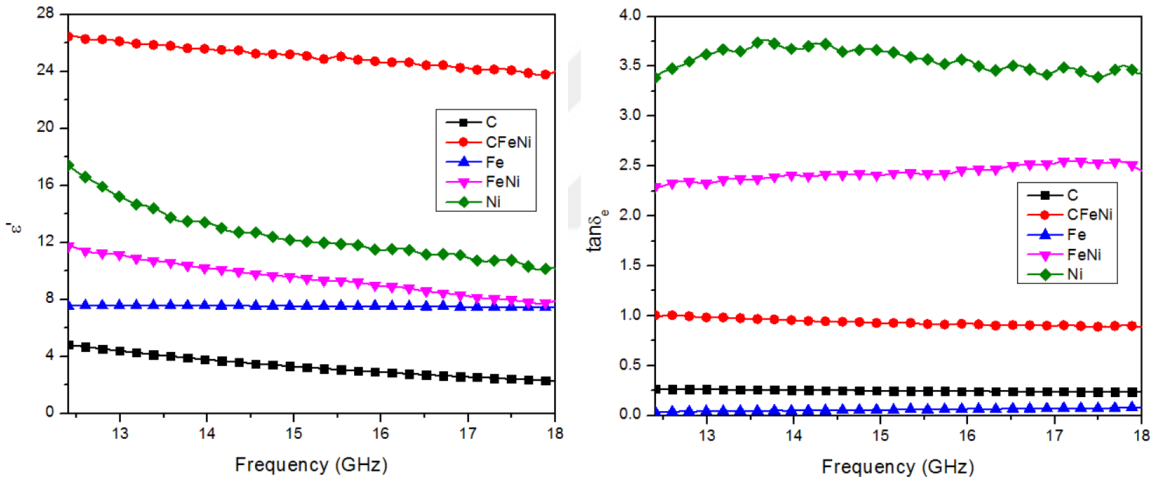


Figure 3.28. Real part of permittivity and dielectric loss tangent of C, CFeNi, Fe, FeNi, Ni micropowder samples.

The dielectric loss tangent of micropowder sample is shown in Figure 3.28. The Ni sample has high dielectric loss tangent and the Fe sample has less dielectric loss tangent. We see that the dielectric loss tangent of FeNi mixture is between Fe and Ni. The dielectric loss tangent of C and Fe is almost constant at P band (12.4-18 GHz). The dielectric loss tangent of CFeNi sample is 1 at the 12.4 GHz and then it decreases slightly with increasing frequency.

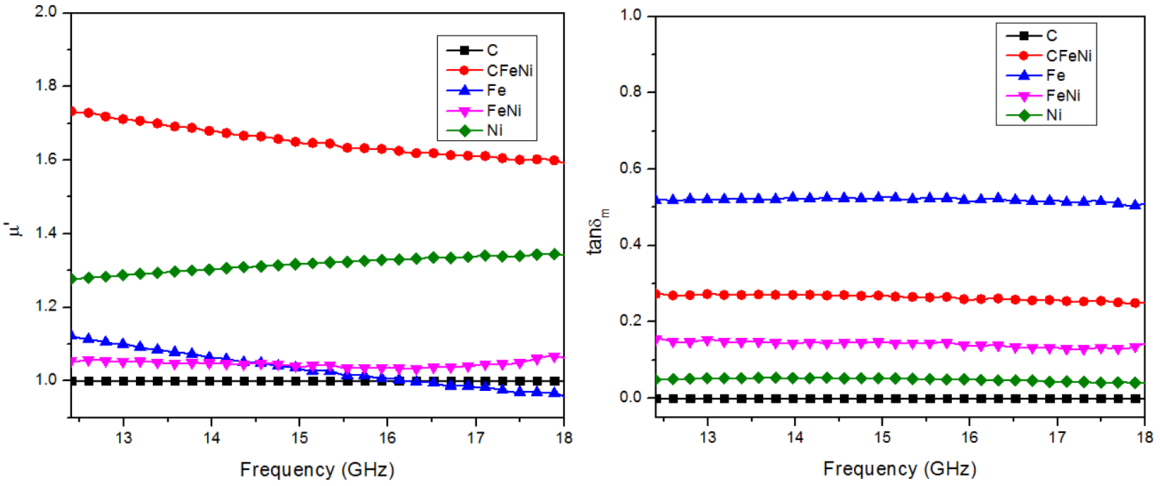


Figure 3.29. Real part of permeability and magnetic loss tangent of C, CFeNi, Fe, FeNi, Ni micropowder samples.

The real part of permeability and magnetic loss tangent of C, CFeNi, Fe, FeNi and Ni sample is shown in Figure 3.29. The values of real part of permeability vary between 1 and 1.8. The real part of magnetic permeability of CFeNi and Fe sample decline gradually. It is observed from the figure, the values of Fe and FeNi sample are close to each other as well as the electric permittivity. The real permeability of C sample is given as 1 by the software, because of its non-magnetic structure. The plot of FeNi sample is between the plot of Fe and Ni sample at the higher frequency. But it has lower μ' than the sample Fe at between 12.4 and 14 GHz. It is observed from the figure, the real part of permittivity and permeability increases when the C, Fe and Ni sample has mixed. All sample show almost flat magnetic loss tangent curve. Due to the C sample has no magnetic absorption, its magnetic loss tangent is zero. Ni, FeNi and CFeNi has larger dielectric loss tangent than the magnetic loss tangent. Conversely, the Fe sample has larger magnetic loss tangent than dielectric loss tangent. So we can say that for Fe sample, most of the absorption results from the magnetic loss tangent rather than dielectric loss tangent. For other sample, the dielectric loss is dominant property to absorb the electromagnetic wave.

For 12.4 and 18 GHz range, the scattering parameter of S11 and S21 of micropowder sample in dB are shown in Figure 3.30. By mixing the Fe, C and Ni powder, the

sample which has lower reflection coefficient is obtained. For whole spectra, while the S11 parameter of Fe has the smallest value, its S21 parameter has the largest value. Conversely, the S11 values of sample C close to -1 dB and its S21 parameter is about -40 dB. The reflection ($R = |S11|^2$) and transmission ($T = |S21|^2$) [141] are calculated from the reflection parameter (S11) and transmission parameter (S21), as shown in Figure 3.31. As expected, Fe sample reflects less electromagnetic wave relative to the other sample. However, it transmits much electromagnetic wave relative to the others. The calculated reflection-R of Fe sample is between %20-40 and the transmission-T is about %11 in whole frequency range. The transmission-T of C, CFeNi,FeNi and Ni is nearly zero. These sample can be considered to be very reflective. The most of incident wave is reflected by the surface and the remaining wave is absorbed inside it. Therefore, the electromagnetic wave cannot transmit to the back surface.

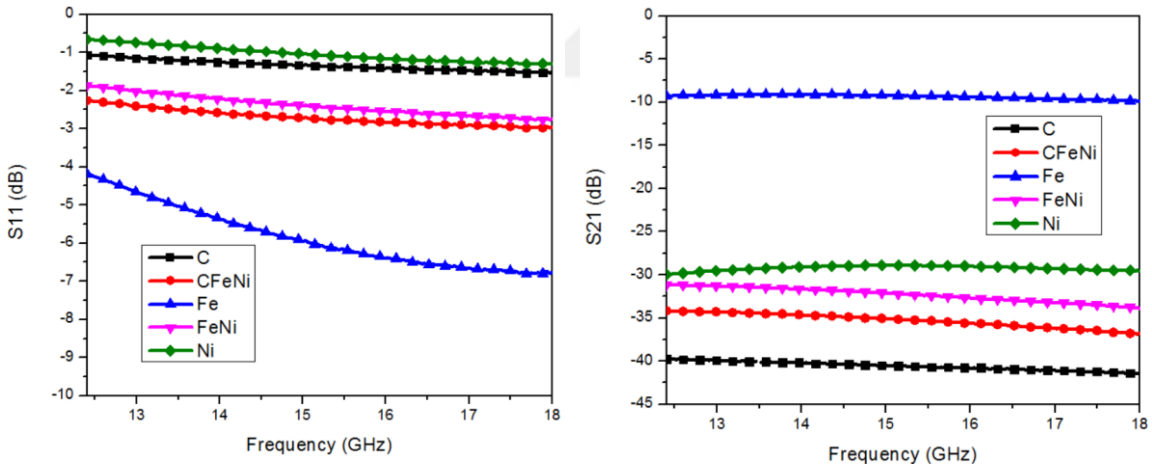


Figure 3.30. Scattering parameters S11 and S21 of C, Fe, Ni, FeNi and CFeNi samples

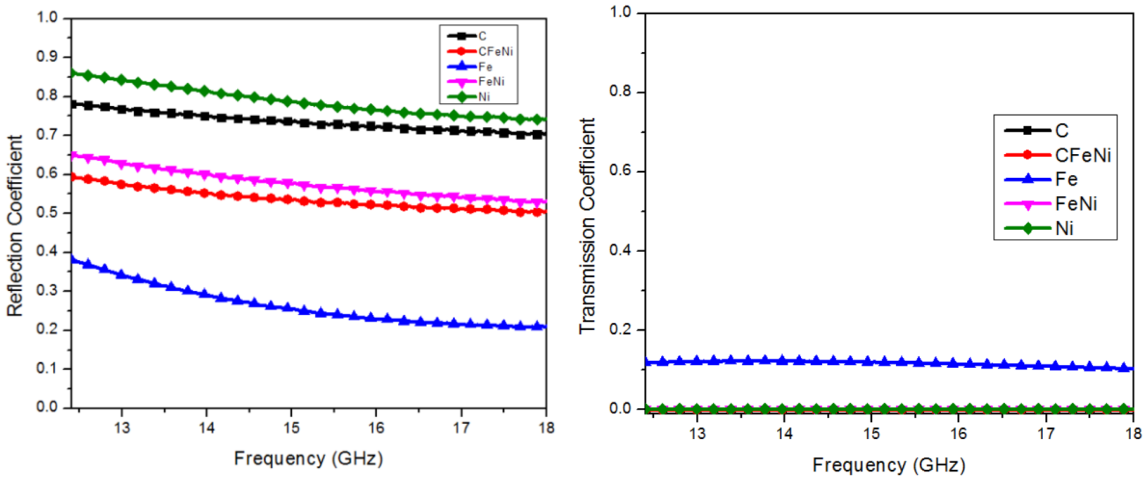


Figure 3.31. Reflection (R) and Transmission (T) of C, Fe, Ni, FeNi and CFeNi samples

The absorption rate of all micropowder sample increases with frequency, as shown in Figure 3.32. The Fe sample exhibit high absorption property that is between %50 and %69. The Ni sample has low absorption rate which ranges between %13 and 26. The sample FeNi occurred by mixing Ni with Fe sample decline the absorption rate of Fe to %40. The absorption rate of C, FeNi, CFeNi and Ni sample mainly depends on the reflection-R because they have almost no transmission-T. It is observed that the C sample has high reflection and low absorption rate which is between % 20-30. So it has best shielding effectiveness (SE).

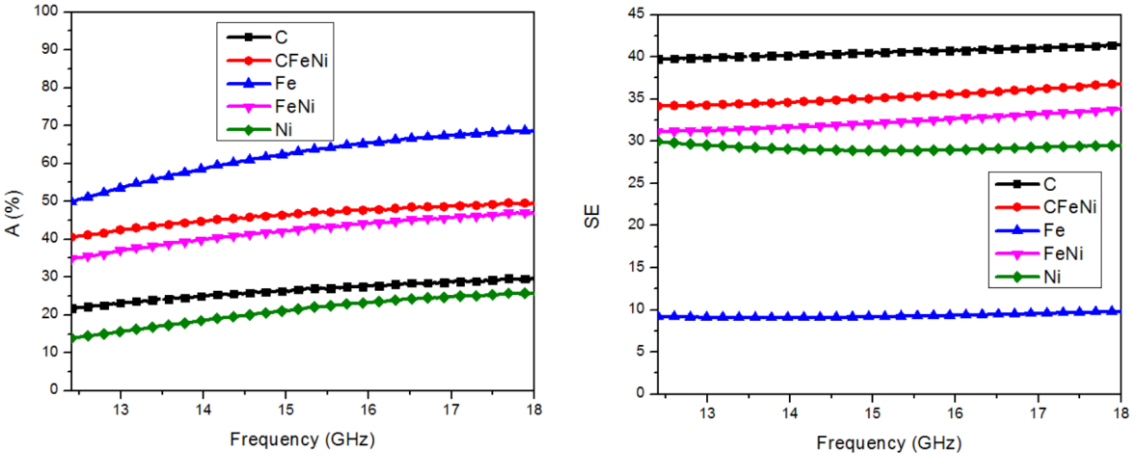


Figure 3.32 Absorption (A) and Shielding Effectiveness (SE) of C, Fe, Ni, FeNi and CFeNi samples

3.4.2. Rectangular Shaped Foam Sample

In this section, the small samples are firstly analyzed to possible to simulate the large sample such as pyramidal absorber, as given in Section 4.2. The small pieces are cut from the produced pyramidal absorber made from C, Fe and Ni. They are taken from the surface of pyramidal absorber due to the surface interacts directly with the electromagnetic wave. They have the rectangular shape that can put into the P and X band sample-holder. So the dimensions of sample are (15.79mm x 7.89mm or 22.86mm x 10.16mm). These cutting samples are different from the bulk samples (expressed in Section 3.4.1 and 4.1). Because they are porous rather than the bulk structure. Then the scattering parameter S11 and S21 are measured with PNA network analyzer. The dielectric and magnetic constants of ε, μ are calculated by using the scattering parameter with the help of the software. The foam samples of Ci Fe and Ni will only compare and examine with the bulk sample in this section.

The dielectric constant ε', magnetic constant μ', dielectric loss tangent $\tan\delta_e$ and magnetic loss tangent $\tan\delta_m$ plots are shown in Figure 3.33. For all sample, the real part of permittivity ε' have low values as compared to bulk sample which is given in previously section. The real part of permittivity ε' of all sample have the values of between 1.4 and 1.8. They are almost flat in all frequency range. Fe sample has low value of real permittivity ε' relative to the others. The permittivity of C and Ni sample are very close to each other. The dielectric and magnetic loss tangent depends on the real part of permittivity and permeability, as given in Eq. 2.28. The C sample has large dielectric loss tangent. It decreases up to 15 GHz and almost flat between 15 and 18 GHz. The Fe sample has the lowest value of dielectric loss tangent. But it is larger than the limit value of 0.01 at between 13 and 18 GHz. It can be seen the comparison between rectangular bulk and foam sample that the dielectric loss tangent of C sample increased and the loss tangent of Fe sample decreased dramatically when the Figure 3.33 and Figure 3.28 are compared each other. The reason for changing loss tangent may be result from the porous medium. In the bulk case, the reflectivity of C sample is much. The loss occurred in the material decreases because less electromagnetic wave can enter into the sample. In the porous medium, If the wave pass through the sample, the particles of sample can interact with the wave to loss it.

For the same reason, the loss tangent of Ni sample decreases in the case of porous medium as compared bulk one.

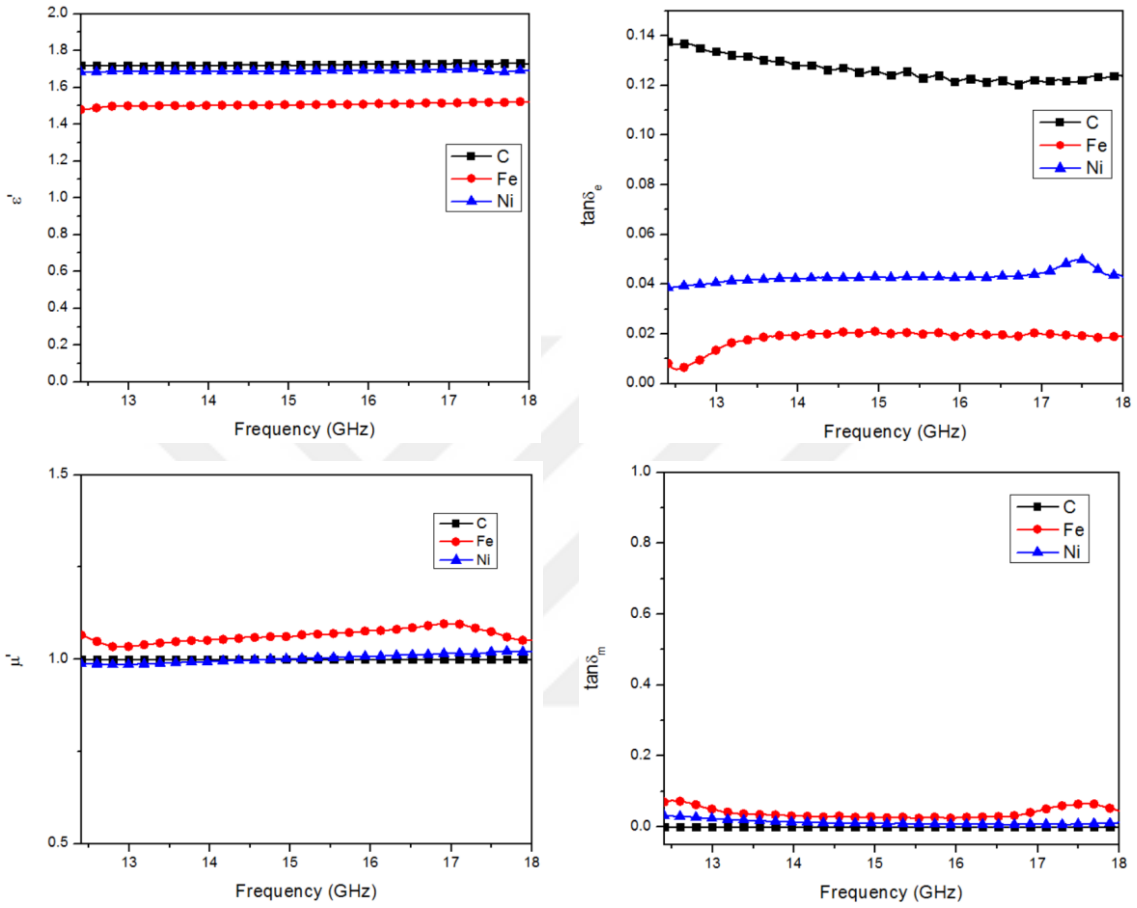


Figure 3.33. Real part of permittivity, permeability and dielectric loss tangent, magnetic loss tangent plots of rectangular shaped foam samples of C, Fe, Ni.

When we compare the result of sample cut from the pyramidal absorber with the bulk sample, we see that the magnetic loss tangent of Fe remains the same at the lower frequencies and it changes little at the higher frequencies. However, the magnetic loss tangent of Fe decreases dramatically in the case of foam sample. The foam sample cut from pyramidal absorber have air inside the porous. That is why the amount of micropowder per same volume reduces. So it may cause the dielectric parameter to change the small value. There is a large difference between the dielectric

loss tangent and magnetic loss tangent. So the most of the absorption can be result from the dielectric loss tangent. However, the ratio of dielectric and magnetic loss tangent of foam sample decreases by comparing with the one of the bulk sample.

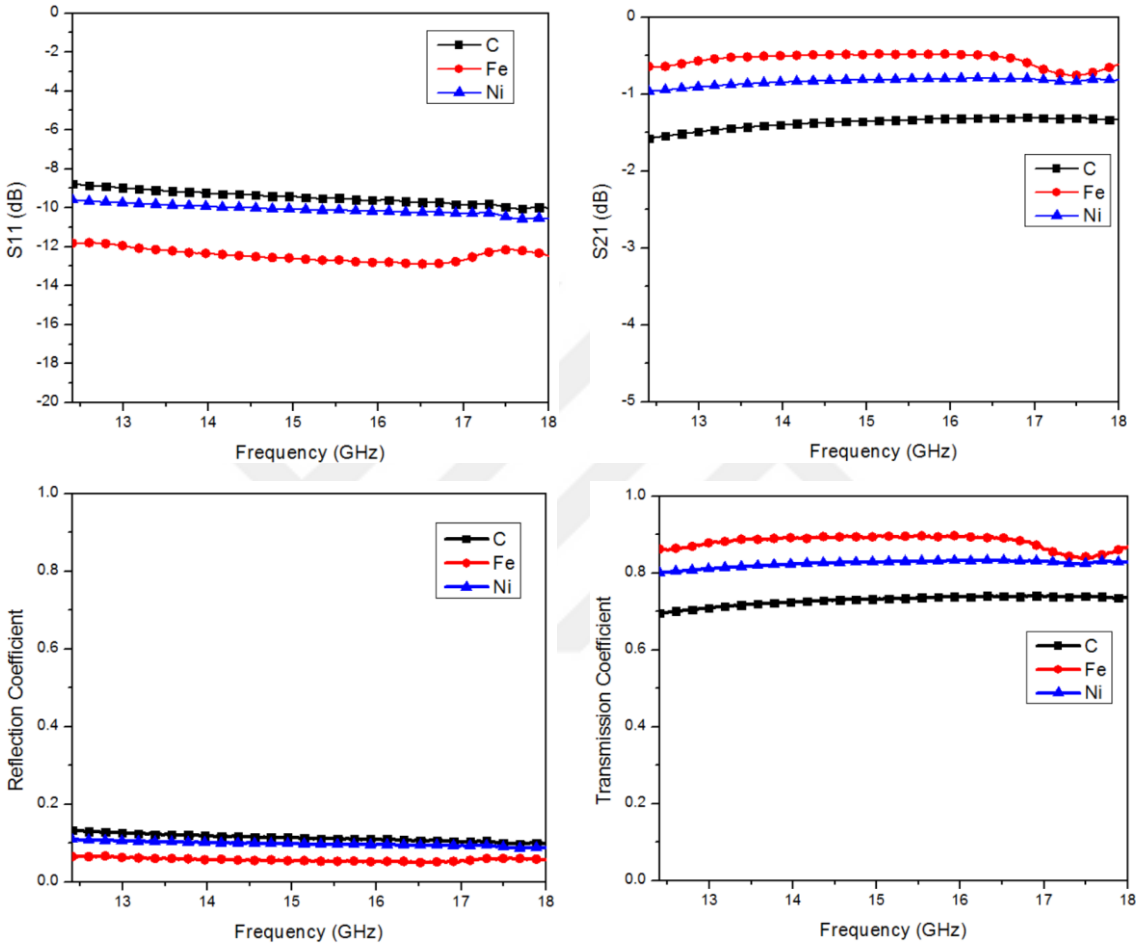


Figure 3.34. Scattering parameters S11,S21, reflection (R) and transmission (T) of C, Fe, Ni, FeNi and CFeNi foam samples

The Figure 3.34 shows the scattering parameter (S11,S21), R-reflection and T-transmission. The value of S11 parameter of C, Fe and Ni sample vary between -8 and -13 dB and have small R-reflection relative to the bulk sample. However, they have high S21 parameter and T-transmission due to its porous structure. The maximum R-reflection value for C, Fe and Ni is % 13, 6.8 and 11, respectively. The maximum T-transmission value for C, Fe and Ni is % 74, 79 and 83, respectively. From the Figure

3.34, the small peak is seen at 17 GHz for magnetic permeability μ' plot and at 17.5 GHz for the magnetic loss tangent ($\tan\delta_m$) plot. When we examine the R-reflection and T-transmission, we see the little curve at 17.5 GHz for R-reflection plot and large dip at 17.5 GHz for T-transmission plot.

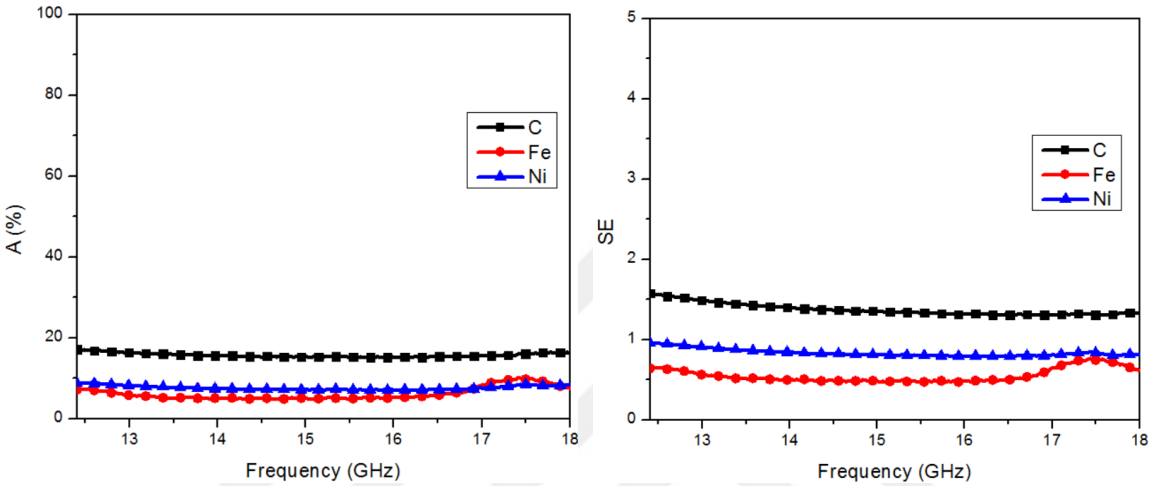


Figure 3.35. Absorption (A) and Shielding Effectiveness (SE) of foam samples of C, Fe, Ni.

The absorption rate and shielding effectiveness are shown in Figure 3.35. Although the SE (Shielding Effectiveness) of C sample is larger than the others, it has the highest absorption rate. All absorption rate of the foam sample have lower values relative to the bulk one. Because the porous medium and the amount of micropowder effect the absorption. In the sample cut by pyramid, as the permittivity and permeability values closes to each other, according to the Eq. 2.39 and 2.68 the matching condition occurs. Therefore the reflection of electromagnetic wave decreases relative to the bulk sample. In addition to this, the transmission coefficient increases because of decreasing the content of micropowder and porous structure. We observe that the absorption rate decreases that may be result from mentioned reasons.

4. PRODUCTION OF MICROWAVE ABSORPTION MATERIAL

The production of microwave absorber can be classified two type such as small and pyramidal absorber. While small samples are fabricated to fit the waveguide measurement tool, the pyramid absorbers are tested with antenna measurement. The below rectangular samples include carbonyl iron (Fe), nickel (Ni) and activated carbon (C) powder. The particle size of nickel powder is 2.5 μm. Activated carbon has 4-12 mesh granular. The ingredient and particle size of carbonyl iron powder is given in Table 4.1.

Table 4.1. Content in weight ratio and particle size of carbonyl iron powder.

	Particle size (μm)	**Fe (%)**	**Ni (%)**	**C (%)**	**O (%)**
Carbonly iron	4-6	> 99.5	< 0.01	≤ 0.04	< 0.2

4.1 Small sample

Two kind of small sample is produced to characterize the microwave absorption properties: rectangular and toroid. The small sample of rectangular shape composed of microparticles and the manufactured samples are shown in Figure 4.1. The microparticles such as C, Fe and Ni are mixed in a ratio as mass to produce new sample, as shown in Table 4.2. To combine the particles together the paraffin wax ($\varepsilon = 2.2 + 0i$, $\mu = 1 + 0i$) is added in a ratio of w/w=1. Then they are pressed as pellets with dimensions 15.8 mm x 7.9 mm for P-band with a thickness of 3mm to determine the microwave parameters.



Figure 4.1. The manufactured rectangular small samples of C, Fe, Ni, FeNi, CFeNi.

The dielectric and magnetic parameters of nanoparticle hexaferrites (Ba1, Ba2, Ba3, Sr1, Sr2, Sr3, Pb1, Pb2, Pb3) and microparticles (C, Fe, Ni) are determined using coaxial line technique (85050C APC7). The toroid manufacturing tools and the produced samples are shown in Figure 4.2. Each sample contains one kind of nanoparticle and are prepared by stirring the paraffin wax (powder:paraffin=1) on the hot plate device. During this process, the hot plate is adjusted to 90 °C and they are stirred approximately 5 minutes.

Table 4.2. Mixture ratio and codes of samples.

	Carbon	**Nickel**	**Carbonyl Iron**
Fe	---	---	1
Ni	---	1	---
C	1	---	---
FeC	1/2	---	1/2
FeNi	---	1/2	1/2
NiC	1/2	1/2	---
FeNiC	1/3	1/3	1/3

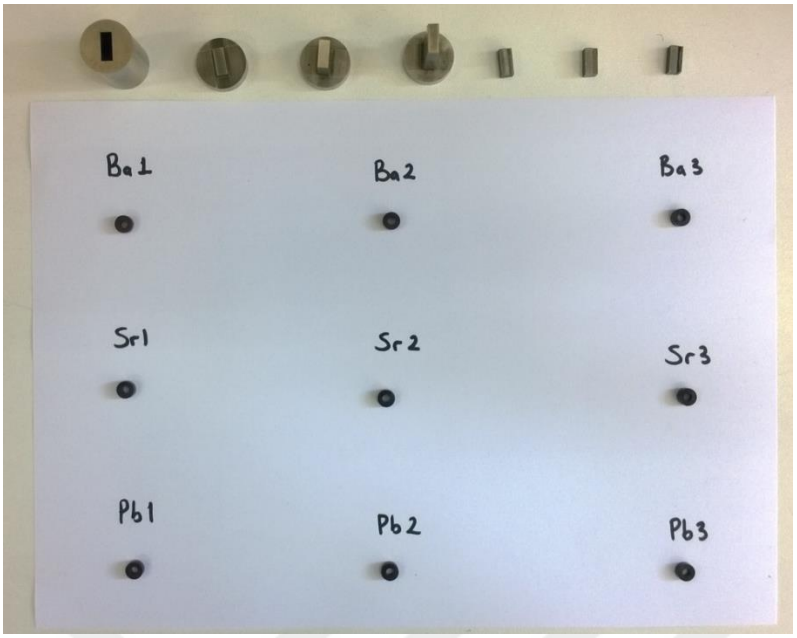


Figure 4.2. Toroid small sample and its manufacturing tool.

Other type of small sample is the rectangular foam sample that is obtained from pyramidal absorbers, as shown in Figure 4.3. These pieces were cut from the surface of the C, Fe and Ni pyramidal absorber surface where the electromagnetic waves contacts firstly. However, they are measured with rectangular waveguide technique.

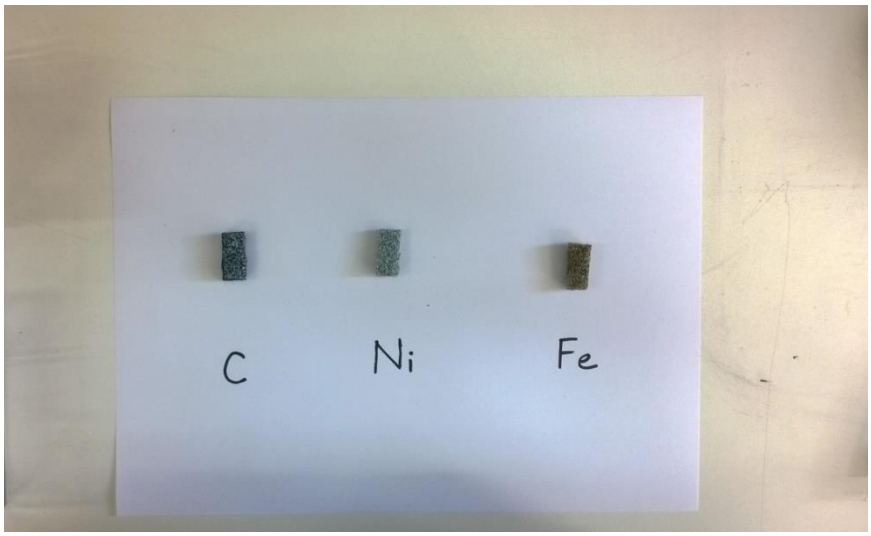


Figure 4.3. Rectangular foam samples containin C,Ni and Fe micropowder.

4.2. Pyramidal absorber

4.2.1 Conventional Design

The conventional pyramidal microwave absorbers are produced based on the features of ETS-Lindgren EHP-8PCL Absorber [142]. The dimension of the conventional pyramidal absorbers is given in Figure 4.4.a. The EHP-8PCL Absorber has 64 pyramids. This absorber isn't preferred due to its larger size. The 36 pyramids are preferred for our produced absorber to get smaller the structure. However, the physical specification of one pyramid is the same with the one of the EHP-8PCL Absorber. For the single pyramid, the overall height is 21.6 cm and the height of the base and single pyramid are 5.1 and 16.5cm, respectively. The pyramid base dimension is 7.625cmx7.625cm.

a) b)

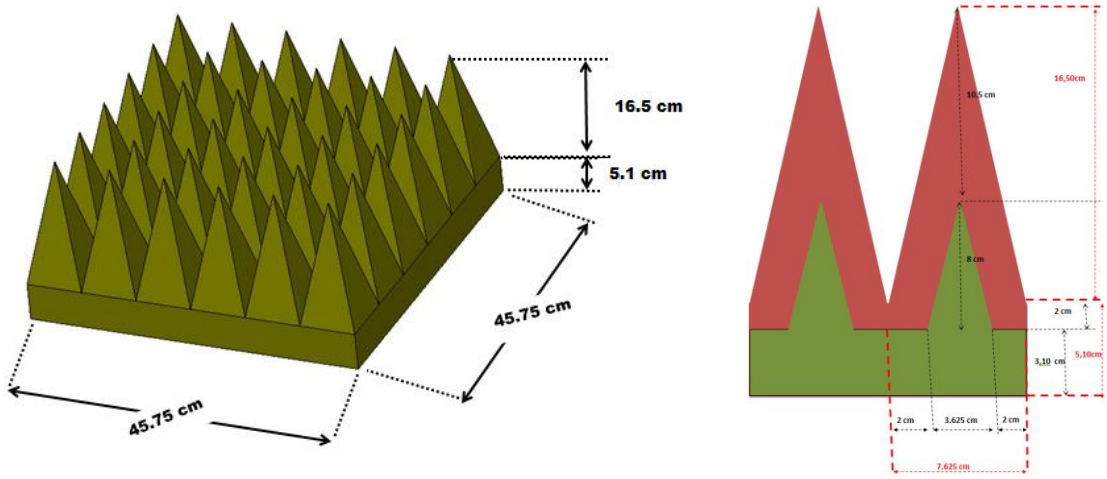


Figure 4.4. Dimensions of conventional (a) and double design pyramid absorber (b).

Firstly, The C/Fe/Ni microparticle are mixed with anti-fire solution in the container. Then the pyramid shaped foam is dipped into the container to impregnate with this mixture. The mixture ratio of microparticle is accomplished by using equal volume, as given in Table 4.2. For Fe, Ni and C, a scale has 800g, 600g and 200g,

respectively. Each pyramidal structure contains the anti-fire solution of 800ml. The pyramidal absorber with “Fe” code contains 800mg Fe microparticle and 800ml anti-fire solution. The pyramidal absorber with “FeNi” code includes 400mg Fe and 300mg Ni and 800ml anti-fire solution. The reason for using anti-fire solution is to prevent the damage form the lamp light and/or sunlight and the degradation with time. In addition to this, to minimize the degradation and increase the resistant across the fire, the anti-fire paint is sprayed on the pyramid structures by using compressor machine. Figure 4.5 shows all conventional pyramidal absorber which are produced with the expressed method before they are painted with anti-fire paint.

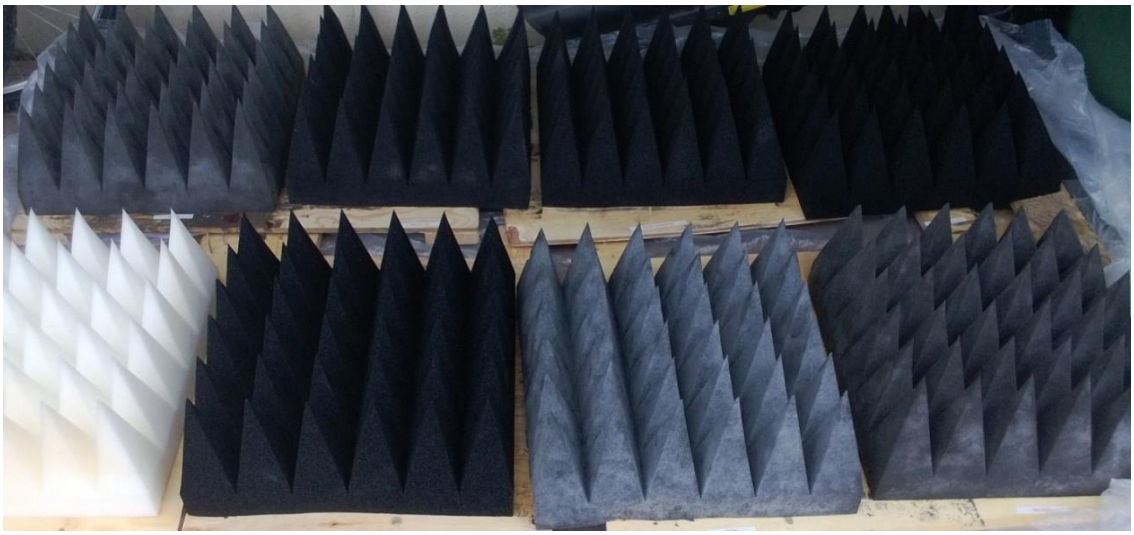


Figure 4.5. Appearance of pyramidal absorber before painting with anti-fire paint.

4.2.2. Double Design (original)

In this section, to prepare the pyramidal absorbers, the new design method is presented. The side view of this design pyramid is shown in Figure 4.4.b. In general, the dimension of new absorber is the same with the conventional absorber which is explained in the previous section. However the new absorber has a triangular hollow at the surface of the pyramid. Firstly, the foam is cut with hot wire machine applying zigzag path to form pyramid shape. In this way, the new absorber is produced so that it consists of two parts which is bottom and upper, as shown in Figure 4.6. The bottom part has the small pyramid that its height and dimension of base is 8 cm and 3.625 cm x 3.625 cm, respectively. The upper part is composed of the hollow pyramid structures. It is cut to form the triangular space at the side face of each

pyramid in the upper part. The purpose of making of two parts is to confine the much electromagnetic wave at between pyramids. So it is possible the electromagnetic wave hit the wall of the pyramid and then it can pass the triangular space where it can die out.



Figure 4.6. Appearance of pyramidal microwave absorbers after they have been painting with anti-fire paint.

4.3 NRL Arch Test Fixture and Measurement

The NRL Arch setup is a kind of free space measurement system. It is used to test the reflectivity of absorbing materials for a given frequency band. It was originally designed at the Naval Research Laboratory (NRL) [143]. The receiver and transmitter antenna are located on the curve of the Arch setup and connected to the network analyzer. The measuring angular-dependent can be realized while the antennas move on the opposite position of the arch. When the antennas are close to each other as possible as, the measurement of normal incidence is nearly realized. The absorber which can be flat [144-146] or pyramidal [147-148] is placed at the center of the arch to test its reflectivity. The Figure 4.7 illustrates Arch measurement setup. In this case, the size of the DUT depends on the focusing of antenna and the selection frequency. Because the diffraction and scattering of the incident wave occur at the edge of the sample, so called “edge effect” [149]. To minimize the edge effect, the size of the sample should be chosen to be as large as possible. Furthermore, the radiation pattern

of antenna should project onto the whole sample. Therefore, the spot-focusing horn lens antennas may be used to focus most of the energy on the sample [150]. At the same time, the distance between sample and antenna must allow the Far Field conditions which are described by Equation (2.98). The value of Far Field for the various antennas is given in Appendix B. For a given typical test sample, it defines the size of the arch and the radiation pattern of the source. The size of the pyramidal absorber in this study is given in Figure 4.4. For this sample, the Figure 4.8 illustrates the size of the arch and the far field distance. However, it shows only the position of stick and antenna that works at X and P band although it can be used to test all band from Ka to R (Appendix B) At the same time, these arch fixtures enable all bands between frequencies of 1.7–40 Ghz via using the long stick. By moving stick up and down, the far field distance of the desired band can be adjusted. Here, PNR 90-441-6 and PNR 62-441-6 model of ATM standard gain horn antenna is considered. They have the gain of 15 dB and approximately 30° angle for 3 dB E-field Beamwidth. The another criterion of ideal size of the sample is that the length should be greater than three times 3-dB E-plane beamwidth of the antenna to neglect the diffraction at the edges [150]. The result of calculation for the antenna used in our study point out that this type antenna is appropriate to measure the reflectivity in the Arch setup.

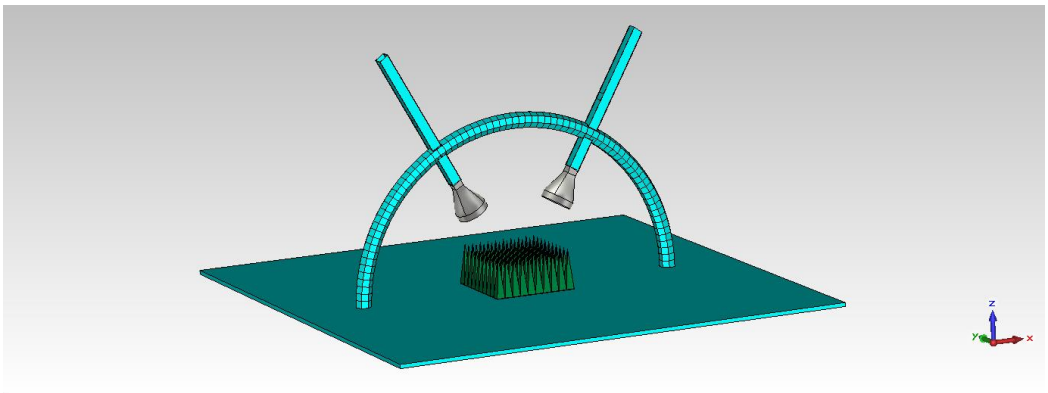


Figure 4.7. Illustration of Arch measurement setup with pyramidal microwave absorber.

The reflectivity of the fabricated pyramidal absorber which are conventional and new design are measured with the new Arch measurement setup, as shown in Figure 4.9. The dimension of an arch is illustrated in Figure 4.10.a. The arch having these dimensions can be operated at X, P, K and Ka band. The Arch, test table and other equipment are made of polyamide to reduce the reflections. Even, the components are connected to each other via the plastic screw instead of metal. There is four type of undesired reflection in such setup: direct horn to horn coupling, arch structure scattering, surrounding environment scattering and standing wave generation. In the commercial NRL Arch, the arch and other equipment made of metal that causes much reflection and signal error in the measurement. When the polyamide material is used instead of the metal, we expect that the arch structure scattering and measurement error caused by reflection will reduce.

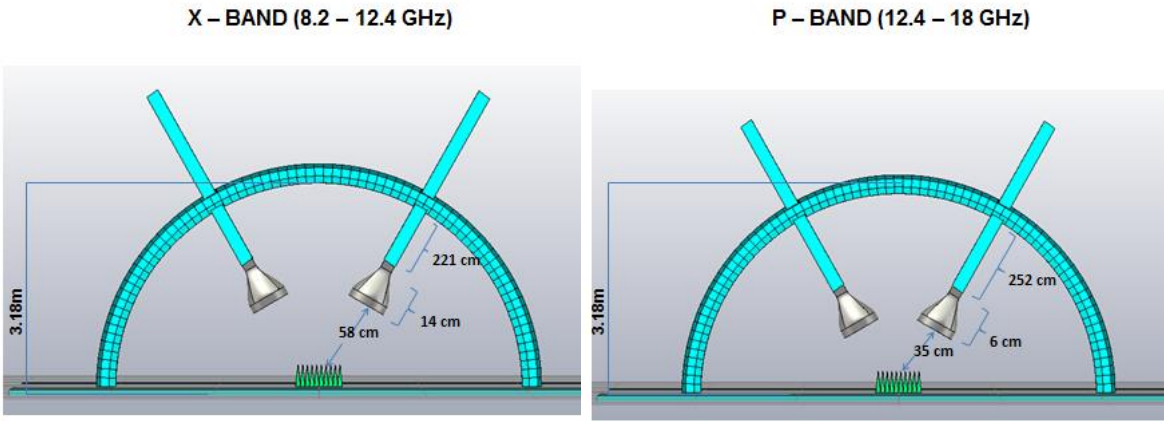


Figure 4.8. Dimensions and Far-field distances of Arch measurement setup for X and P band.

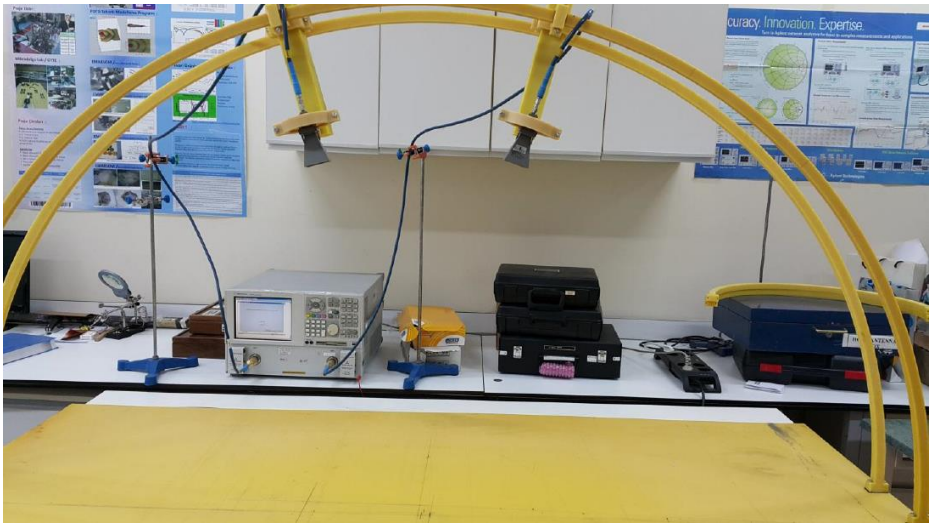


Figure 4.9. New type Arch measurement setup operating at X, P, K and Ka band.

The Figure 4.10.b shows the polyamide components that are built at the mechanical workshop. The new designed Arch measurement system composed of *two arch, two stick, two antenna disk for X, P and K band, two clamp, two movable holder, a test table, PNA E8364B network analyzer, two high performance microwave cable and two horn antenna* for X, P and K band. The antenna is placed at the center of the disk and the clamp can hold firmly the disk. It can rotate easily about its axis. By rotating the disk as 90 degrees, it enables to measure the electromagnetic field for TE or TM mode. The clamp is connected to the stick via long plastic screw. So that the distance between pyramidal absorber/flat absorber and antenna or far field distance can be adjusted for the desired frequency by carefully moving the stick to up and down direction. The point corresponding to the far field distance for X/P/K band is marked at the movable stick. The sticks can pass through the movable holder and be held tightly by it. In addition to this, the movable holder can go on the rail which is created by two the arch.

a) b)

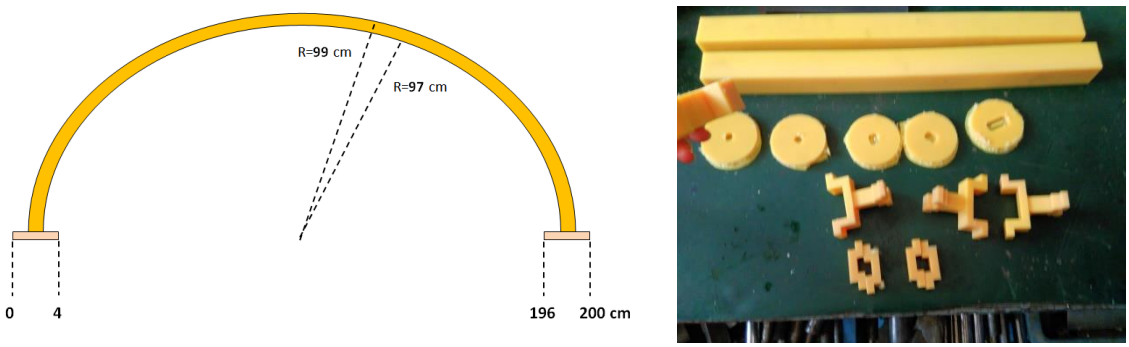


Figure 4.10. (a) The illustration of new design arch operating at 8.2-40 GHz and (b) its parts that are stick, disk, clamp and movable holder made of polyamid.

5. Simulation

In order to test the reflectivity or dielectric constants of microwave absorbers with the simulation, the below method as shown in Figure 5.1 is applied step by step. First step is to synthesize and produce the nanohexaferrite powders. Then the small sample or pyramidal absorber is fabricating using these powders. Third step is to determine the dielectric and magnetic constants via transmission line technique. Fourth step is to model the small and large structure in CST Microwave software. The last stage is to compare the simulation results with the measurement results.

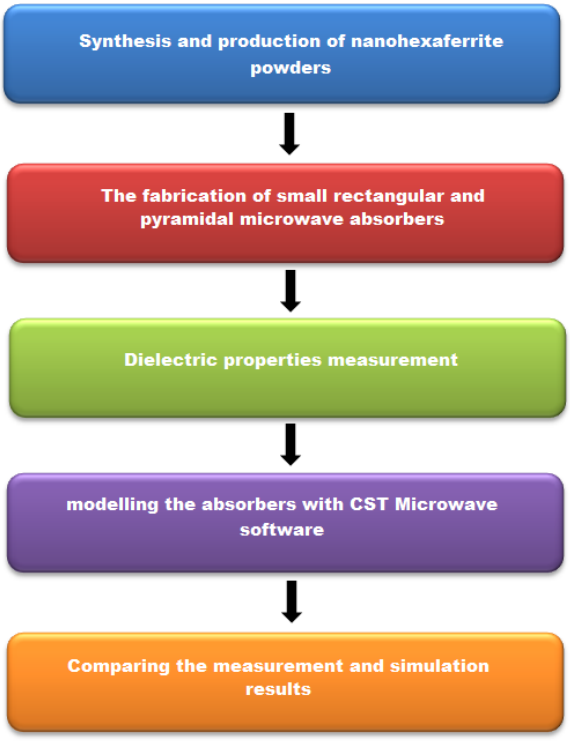


Figure 5.1. Process flow for the developing of the microwave absorbers by simulation method.

5.1. Small Sample

5.1.1 Micro-Sized Rectangular Sample

In this section, the waveguide measurement in P band (12.4-18 GHz) is compared with the simulation result. The dielectric and magnetic constant of micropowder samples was obtained with the measurement by using E8364B network analyzer, as given in 3.4.1. The obtained dielectric and magnetic constant with their real and imaginary part from the microwave measurement are used in the simulation process. The simulation work is performed with the help of full wave electromagnetic simulation tool of CST Microwave Studio. Firstly, the waveguide (WR 62, given in Appendix C) and sample in the simulation tool are designed exactly the same size as that of experiment, as shown in Figure 5.2. Then, the dielectric and magnetic parameter obtained by the experiment are embedded into the simulation. The waveguide is made of PEC (Perfect Electric Conductor) material. In the simulation, two port waveguide technique is used as well as the measurement. The modeling sample is positioned between two waveguides. After loading the dielectric and magnetic constants determined by measurement into sample in the simulation software, they have been linearized with second order. The dimensions of modeling sample are represented in Figure 5.3. The length, width and thickness of the modeling sample is 15.799, 7.899 and 3 mm, respectively [151].

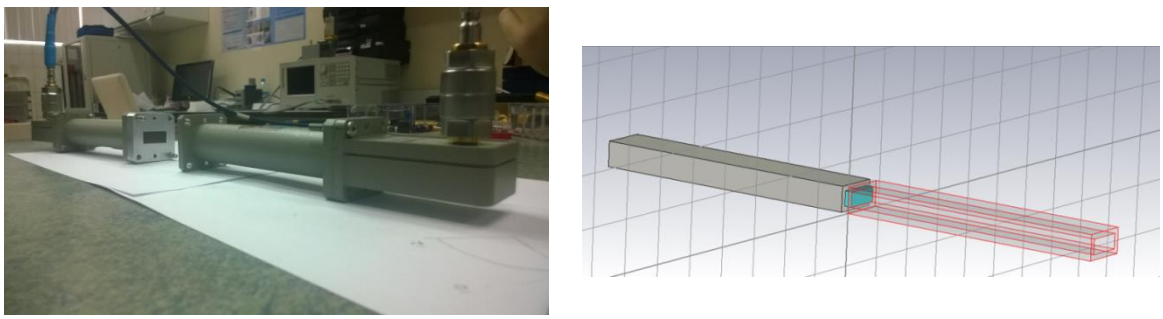


Figure 5.2. 12.4–18 GHz (P Band, WR62) measurement tool (a) and screenshot from simulation (b).

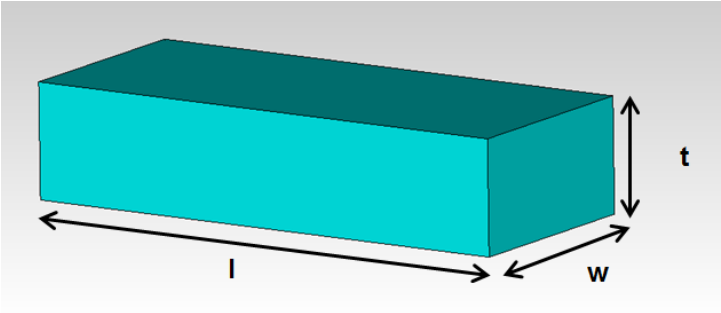


Figure 5.3. Dimensions and perspective image of microwave absorbing sample simulated by using waveguide method.

The scattering parameter (S11, S21) results of modeled micro C, Fe, FeNi, CFeNi, Ni samples for P band are given below figures. In the simulation, the condition well-known as Courant Condition [152] is used:

$$\Delta t = \frac{\Delta x}{\sqrt{n} c_0} \tag{5.1}$$

This formula represents the required minimum distance in a cell where EM wave cannot go faster than light. To provide this condition, the number of points per cell is chosen as 10. The entire simulation consists of 4-5 million of mesh cell. The electromagnetic wave E is set to "0" at the boundary conditions X, Y and Z [153]. Because, the wall of waveguide is made of PEC metal. In this way, the electromagnetic wave confined by PEC can propagate properly through such a material. The trigger signal is selected in the form of the Gaussian form. The simulation results are compared with the one obtained from measurement by network analyzer.

Nickel powder on the microstructure is modeled in the frequency range of 12.4-18 GHz. As shown in Figure 5.4, the scattering parameters obtained from simulation results are consistent with the experimental results. The red and black line shows the

measurement and simulation results, respectively. The symbols (■, ■) represent the reflection coefficient S11 and the symbols (▶, ▶) represent transmission coefficient S21. The S11 parameter shows a decreasing trend from 0.92 to 0.86 in P band and it closes the values of experiment at the higher frequencies. We see that the S11 parameter of simulation and measurement has the same value at 14 and 18 GHz. The S11 parameter in the simulation decreases with increasing frequency as well as the measurement.

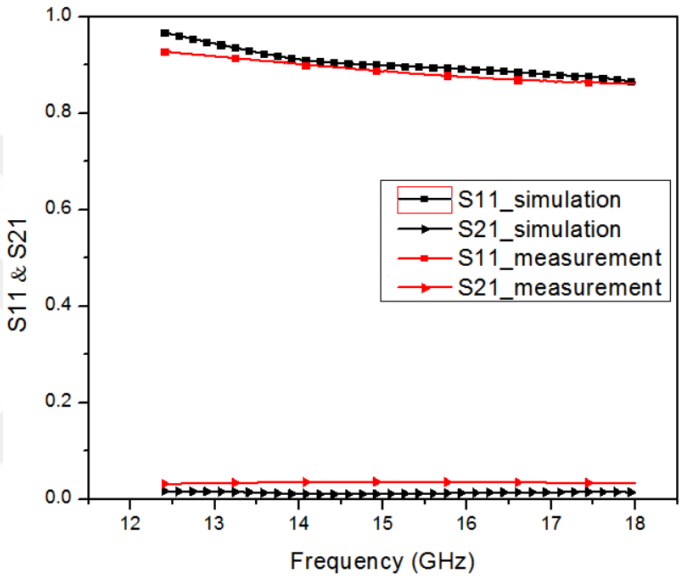


Figure 5.4. Comparison of scattering parameter S11, S21 between simulation and measurement for Ni sample.

The Figure 5.5 shows the comparison of scattering parameter between measurement and simulation for FeNi sample. As the S11 parameter decreases slightly at the whole frequency, the S21 parameter remains constant for both measurement and simulation. For the S21 parameter, high degree of consistency is observed with simulation. For the S11 parameter, it closes the experimental data at the higher frequency. The comparison results between measurement and simulation for CFeNi sample is shown in Figure 5.6. The S21 parameter for simulation is observed to be the same with the experimental results. There is a %5 percentage difference between simulation and measurement results at 12.4 Ghz. However, this difference falls to a minimum level with increasing frequency. As excpected, the S21 parameter for both measurement and simulation is close to zero.

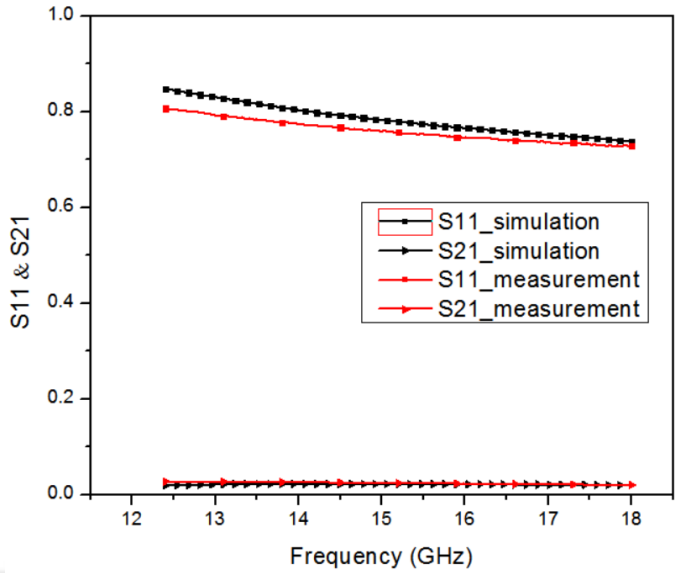


Figure 5.5. Comparison of scattering parameter S11, S21 between simulation and measurement for FeNi sample.

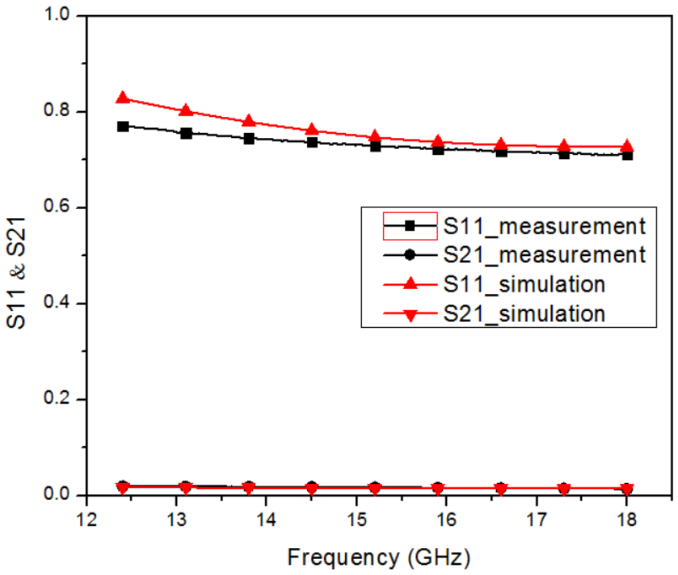


Figure 5.6. Comparison of scattering parameter S11, S21 between simulation and measurement for CFeNi sample.

The simulation result of microstructure Fe sample can be compared to measurement data from the Figure 5.7. While the S11 parameter of measurement and simulation have exactly the same numerical value at the lowest frequency, it is observed that they have small difference at the higher frequencies. For the transmission coefficient

S21, there is a small difference at the high and low frequencies. But it is exactly the same with the measurement data at about 15 GHz. In genearal, the simulation results are consistent with the measurement data. In addition to this, the small difference between simulation and measurement can be result from the mismatch during fitting the dielectric $\varepsilon^{'}, \varepsilon^{''}, \mu^{'}, \mu^{''}$ parameter in the software.

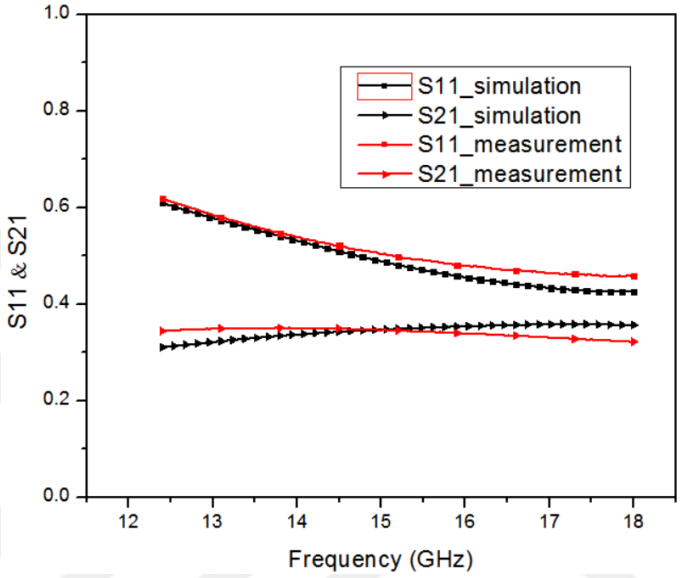


Figure 5.7. Comparison of scattering parameter S11, S21 between simulation and measurement for Fe sample.

5.1.2 Multilayer Absorber

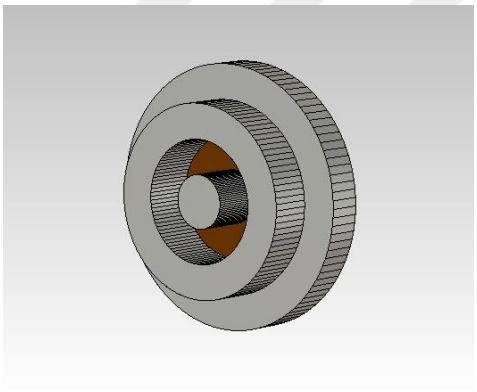
In the previous sections, Barium (Ba), strontium (Sr) and Lead (Pb) nanoparticles synthesized by the Sol-gel method together PMMA as the template due to the advantages of inexpensive precursor, a simple process, time saving and a resulting nano-sized powder [154]. These nanohexaferrite particles are new materials that were produced with a concentration ratio of 20:80 (PMMA/Ba,Sr,Pb) by weight. In this study Dielectric properties (εr and μr) of Ba, Sr ,Pb hexaferrite and iron powder materials were measured with Agilent E8364B VNA (Vector Network analyzer). Coaxial line technique (85050C APC7) between 2-18 GHz is used to determine reflection coefficient S11 and transmission coefficient S21 parameters. The dielectric properties of Ba, Sr and Pb hexaferrites are calculated using the Agilent 85071E

Software (Appendix D). Then these absorbing material are simulated using Computer Simulation Technology (CST) [155-156]. The measured data of permittivity and permeability of these materials are implanted and fitted in CST Microwave Simulation. Toroid shape is designed sufficiently so that associated with the dimension of measurement kits. The absorber have prepared based on different layer and arrangement. Fe absorber is doped between Ba, Sr and Pb hexaferrite absorbers to enhance reflection loss.

a)



b)



c)

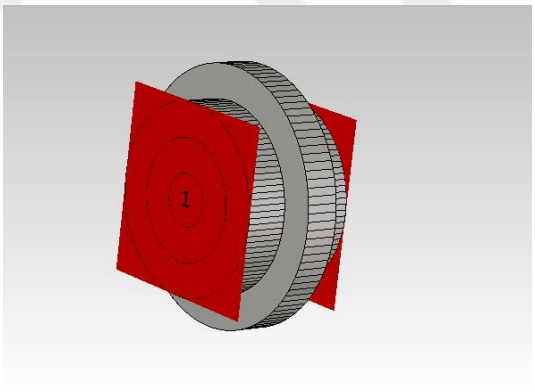


Figure 5.8. APC7 toroid measurement kit (a) with precision airline body (middle) and precision airline center conductor, toroid design in CST software (b), toroid design with waveguide ports 1,2 (c).

The Figure 5.8.a represents the measurement kit (Agilent 85050C APC7) and toroid design from CST software. The APC7 toroid kit consists of *"7mm Precision Airline Body, TRL Adaptor, 7mm Precision Airline Center Conductor and two sexless adapter"*. The TRL (Thru-Reflect-Line) calibration technique is applied before the

measurement. In Figure 5.9.a, the screen of network analyzer shows the S11 and S21 parameter in terms of logarithmic scale after the calibration. It is observed that the plot of S11 is “0 dB” and S21 is lower than -50 dB. For the measurement, the fabricated toroidal sample is put into the Airline Body. Where it should be noted whether the Airline Center is inside the toroidal sample. While the sample is pushed with the help of hand through the hollow of the Airline Body, it requires attention. Because the ones of soft sample can leave tiny pieces as it goes through the hollow. So this can causes the accuracy of measurement to lose. The Figure 5.9.b represents the “pusher” which is made from Teflon material in order to prevent the pieces of sample spreading into the Airline Body. By using the Teflon pusher, the sample can be easily and slowly pushed without any dirty.

The length of the Airline Center and Airline Body is 6.95 ± 0.02 mm. The length of test sample is 3mm. The difference in length between sample and Airline Body is taken into account by entering the numerical values into the Agilent 85071E Software. In the simulation, the Airline Body, Center Conductor and test sample are designed, as shown Figure 5.8.b. The other equipment can be neglected in simulation. Because for measurement the reference plane is defined at the end of the Airline Body after the calibration process is performed. Therefore, excitation waveguide port 1 is applied on the end of Airline Body where the test sample put. The waveguide port 2 is applied on the output end (shown in Figure 5.8.c).

a) b)



Figure 5.9. Plot on the screen of network analyzer after the calibration for toroid measurement (a), pusher to insert easily the sample in the waveguide (b).

In simulation, the background is chosen as “normal” so that the electric permittivity and magnetic permeability is assign to be 1. The material type of the toroid waveguide is chosen as “PEC”. To get the dielectric and magnetic properties of the sample during the simulation, the measurement result obtained before is used. Because the data of measurement has always the random fluctuation caused by thermal effect or noise source, its curve need to be fit. Therefore, the real part of permittivity ε', the imaginary part of permittivity ε'', the real part of permeability μ', the imaginary part of permeability μ'' are fitted in second order. For example, the Figure 5.10 shows only the permittivity ε' for Ba1 sample and its fitting curve.

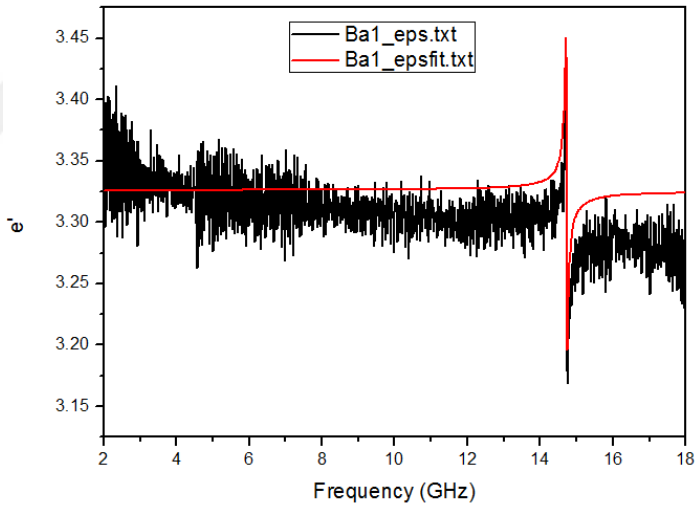


Figure 5.10. Plot of permittivity of Ba1 sample and fitting line.

The scattering parameter of Ba1, Sr1, Pb1 sample in the range of 2-18 GHz that have thickness of 3mm were mentioned in the section 3. In addition of these, the Fe sample having toroidal shape is prepared as thickness of 3mm. Then the scattering parameter is measured in the range of 2-18 GHz via network analyzer. At the same time, the simulation results are performed for these samples to compare with measurement of

scattering parameters. The Figure 5.11 shows that the simulation results are agreed with measurement results. The peak of permittivity at about 15 GHz makes the small dip in the S11 and S21 parameter. Explicitly, the dip of Pb1 sample is sharper than the others. But it has a smooth wavy curve after 15 GHz. The difference between simulation and measurement of Fe sample is very small. The reason for the comparison is that verify the simulation results of Ba1, Sr1, Pb1 and Fe sample which are used in the "multilayer absorber".

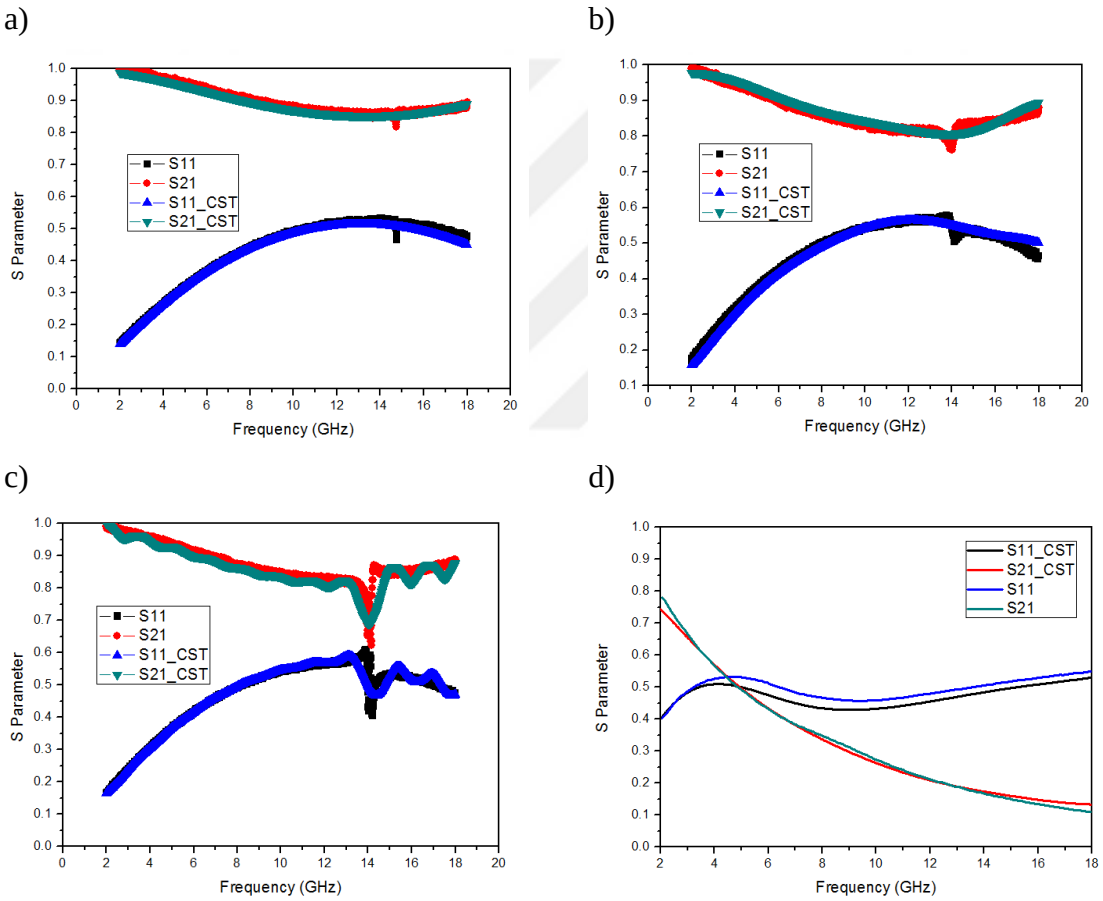


Figure 5.11. Comparision of scattering plots between measurement and simulation of (a) Ba1, (b) Sr1, (c) Pb1 and (d) Carbonly Iron (Fe) .

The new multilayer sample consists of Ba1, Sr1, Pb1 hexaferrite and Fe micropowder layer. Figure 5.12 depicts the multilayer absorber with the value of thickness x and y. Where "x" symbol denotes the thickness of hexaferrite sample such as Ba1, Sr1 and

Pb1 layer. The “y” symbol denotes the thickness of micropowder sample which is Fe layer. The brown, blue, white and grey layer shows the Ba1, Sr1, Pb1 and Fe, respectively. The Fe layer is located in front of the Ba1 and at the back of the Pb1 and between the hexaferrite layers. The configuration of multilayer absorber is “Fe-Ba1-Fe-Sr1-Fe-Pb1-Fe”. At the beginning, we choose that x, y equal 1.3 and 0.15. By using “parametric study”, the scattering parameter is observed when the thickness of each layer changes.

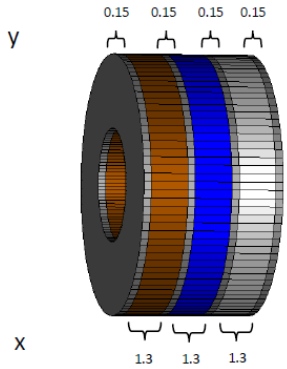


Figure 5.12. Simulation design of multilayer absorber consisted of Ba1, Sr1, Pb1 and Fe layers.

The Figure 5.13.a shows the S11 parameter in dB that changes with the variation of x parameter while the y parameter remains constant. For x=1.3mm and y=0.15mm, the length of the multilayer model reaches 4.5mm. However, the above model Ba1, Sr1 and Pb1 performed simulation has the thickness of 3mm. For comparison, we need to interest the model which has x=0.8 and y=0.15. Because this model has the same thickness with the above sample consists of only Ba1/Sr1/Pb1/Fe. The S11 performance of this multilayer model is similar to the one of Ba1/Sr1/Pb1 modeled sample up to 12 GHz. However, the S11 of multilayer absorber with x=0.8 and y=0.15 provides better performance than the one of Ba1/Sr1/Pb1 model. For instance, the value of S11 parameter for multilayer and Ba1 model at 18 GHz is -10dB and

-7dB, respectively. For the case of x=0.5 and y=0.15, the length of multilayer is 2.1mm. The Figure 5.13.a shows that the S11 parameter performance is not good. It is higher than -10 dB between 4-18 GHz. And we can predict the S11 parameter in the case of x=0.7 that has the value better (below) than -20 dB at the frequency higher than 18 GHz. In generally, they exhibit that the absorption frequency occurs in the frequency range between 14 and 18 GHz. We see that its absorption frequency shifts towards the lower frequency with increasing the value of x. The shifting of absorption frequency to the lower value can be explained with increasing the length of the multilayer. Because, the lower frequencies correspond the longer wavelength. Therefore, the longer wavelength can made the resonance peak with the longer structure. So, we can express that the Fe layer added to the Ba1-Sr1-Pb1 sample cause the resonance at the higher frequencies.

a) b)

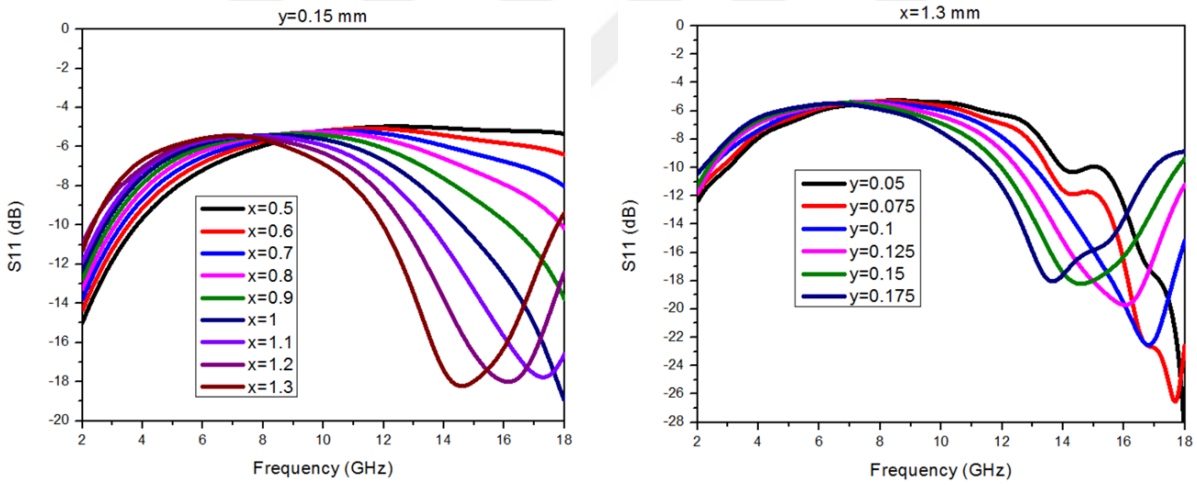


Figure 5.13. S11 parameter versus frequency for multilayer absorber while (a) changing x ,constant y=0.15mm and (b) changing y, constant x=1.3mm.

The Figure 5.13.b shows that the changing of S11 with the x=1.3mm (the thickness of hexaferrite layer remains constant) as the ‘y’ parameter changes from 0.05mm to 0.175mm. If the thickness of Fe sample decreased, the reflection loss depth gets stronger. In the case of the changing of ‘y’ parameter, the smooth wavy curve is

observed at the S11 parameter. Here, ‘y’ means the length of Fe layer. In fact, some S11 curve is made of two or three smooth wave. Especially, the smooth wave is much when the thickness of Fe is smaller. This means that the Fe layer behave like the resistive sheet. From this point of view, the multilayer absorber is similar to Jaumann Layer (as explained in Section 2.6). At the same time, the resonance peak shifts to the lower frequency with increasing “y” parameter.

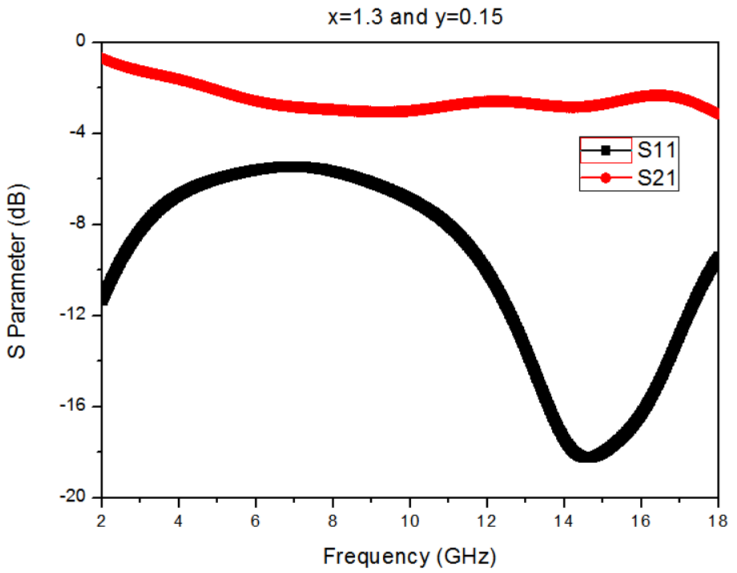


Figure 5.14. Scattering parameter plots versus frequency of multilayer absorber for the case x=1.3mm and y=0.15mm.

The multilayer absorber having the best performance from the all variation is shown in Figure 5.14. It has dimensions of x=1.3mm and y=0.15mm. The multilayer absorber made of the mixture of Ba, Sr, Pb and Fe layer. It exhibits the reflection loss better (below) than -10 dB in the P band range and the resonance peak at about 14.5 GHz. In addition to this, the insertion loss is about -3 dB. It points that the electromagnetic wave can propagate through such material. As a result, by using the Fe layer between hexaferrite layers and at the end of these materials, the new multilayer absorber investigated in this research. This multilayer absorber has -18.22 dB at 14.5 GHz. The bandwidth is 6 GHz at below -10dB.

5.1.3. Metamaterial Absorber

The dielectric properties and scattering parameter of Fe, C, CFeNi, Ni micropowder and BaM, SrM, PbM hexaferrite sample were examined in the previous sections. In this section, only the scattering parameter and absorption property of Fe sample is analyzed as simulation by using U shaped line [157] (shown in Figure 5.15). This U shaped line is made of copper and it is on both front and back of the surface. We also choose the sample as ECCOSORB for reference. Because, it is good absorber that exist in the library of the CST Microwave Studio.

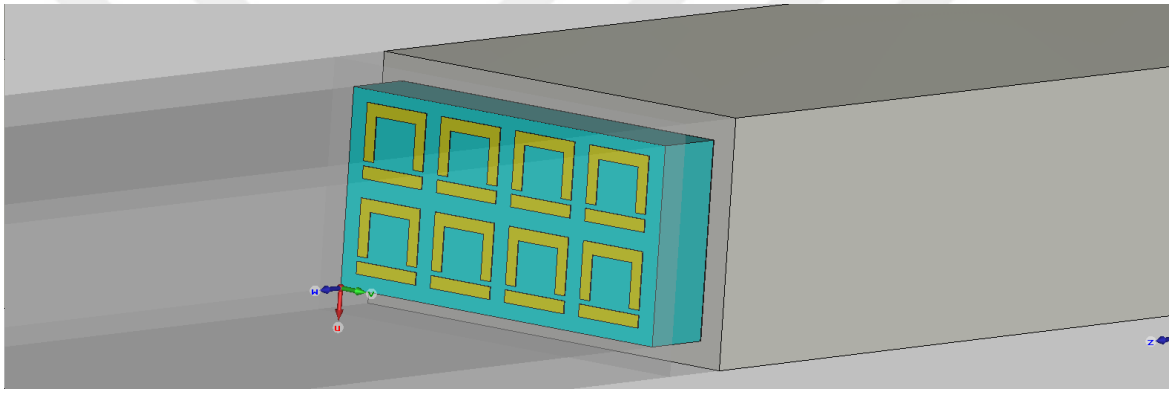


Figure 5.15. Perspective view of metamaterial absorber in waveguide from CST Microwave software.

The metamaterial absorber arranged with the various configurations. All configurations are given in the Table 5.1. The designed absorber is composed of three parts. The front and back of surface is the U shaped structure which is made of copper (conductor). The sample is between both U shaped structures. The various type of absorber is designed with this principle. For example, FFC code means: the front surface of absorber is made of carbonly iron (Fe), the structure at the middle is made of carbonyl iron and the U shaped structure at the back of the metamaterial absorber is made of copper.

The scattering parameter and absorption rate associated with the above absorbers are shown in Figure 5.16. In the case of the front and back of absorber that are the U

shaped structure which is made of Fe sample (FFF code), the decreasing of S11 parameter is observed relative to the "0F0" structure. If the copper (FFC) is used at the back of absorber instead of carbonyl iron, the S11 parameter is lower than one of the FFF absorber up to 15 GHz. After this point, it increases up to 18 GHz. When the copper type of U shaped structure presents at the front and back of the absorber, it is observed that the S11 parameter increases dramatically.

Table 5.1. Metametarial absorbers in various configuration with codes.

Code	Front (U shaped Line)	Middle	Back ((U shaped Line)
CFC	Copper	Carbonly Iron	Copper
FFF	Carbonly Iron	Carbonly Iron	Carbonly Iron
FFC	Carbonly Iron	Carbonly Iron	Copper
CEC	Copper	ECCOSORB	Copper
EEC	ECCOSORB	ECCOSORB	Copper
0F0	---	Carbonly Iron	---

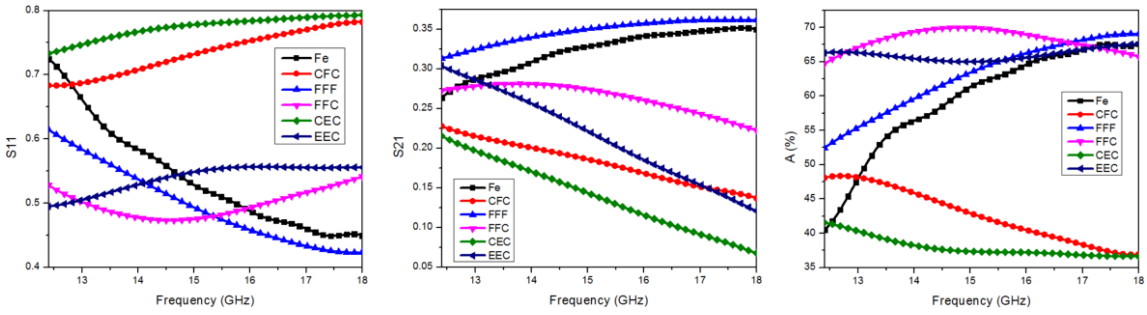


Figure 5.16. Simulation results (a) S11, (b) S21 of metametarial absorber for various codes of Fe, CFC, FFF, FFC, CEC, EEC and (c) their absorption plots.

In similar way, the absorption rates were compared using the Equation of $A = 1 - |S11|^2 - |S12|^2$. The sample having "FFF" code has absorption rate larger than "0F0" sample. It is found that the use of the U shaped structure resulting in an improvement of %12 in absorption for the sample with "FFF" code at 12.4 GHz. At the metametarial absorber with "FFF" code, the U shaped structure located at the front and back of the absorber and the sample located between the U shaped structures are chosen as Fe sample. If the U shaped structure located at the back of the surface is chosen as copper, the absorption rate increases effectively for all frequency range.

5.1.4. Multihole Absorber

It is known that the incident electromagnetic wave firstly hit the surface of the absorber. The impedance between the free space and substrate and also the shape of the surface can affect the absorption performance of sample as negatively or positively (expressed in Section 2.5.1). So we can make holes at the surface of the absorber where is located in the direction of incident wave. Only Fe absorber designed with 50 holes which has cone formed. The height of the cone is the same of the width of absorber which is 3mm. By using "the parametric study", the absorption rate of designed structure is analyzed with the changing radius of cone. The multihole absorber is modeled with the two port waveguide by using CST Microwave Studio software, as shown in Figure 5.17.

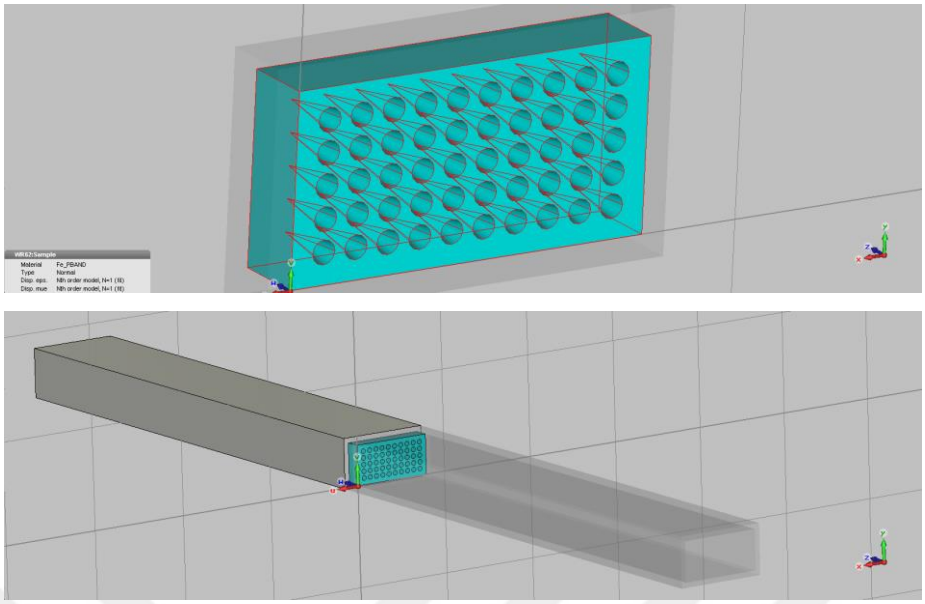


Figure 5.17. Screen image of modeling multihole absorber and perspective view.

The Figure 5.18 shows the absorption rates as percent. Where r_cone represents the radius of cone which designed on the surface of the absorber. Figure reveals that the absorption rate changes in different amounts, while the radius of cone changes. At the lower frequency, the absorption decreases with increasing the radius of cone. However, at the higher frequency, the absorber having large radius of cone exhibits the best absorption performance. Because the large cone allows the electromagnetic wave to strike many times to the inner wall of the cone. That is, this type of absorber behaves like that the electromagnetic wave can enter much inside the absorber in the case of the smaller wavelength. So this causes the increasing the absorption for the case of high frequency. Moreover, the hitting wave inside the wall of cone decreases at the higher frequencies while the hole in the surface of the absorber shrinks. However, the absorption rate decreases because the incident wave cannot interact due to the longer wavelength. Therefore, this affects the absorption performance of sample having the cones that is not better than the absorption of sample without hole at the lower frequency.

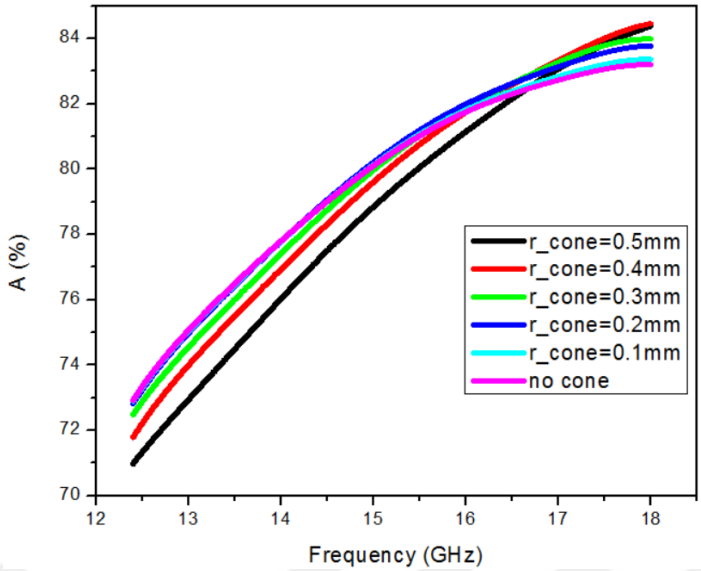


Figure 5.18. Microwave energy absorption curve for multihole absorber changing the radius of cone.

5.2 Pyramidal Absorber

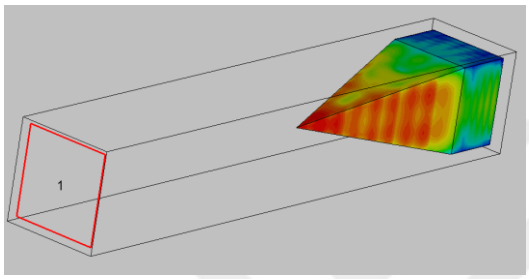
5.2.1 Single Pyramid

5.2.1.a Foam

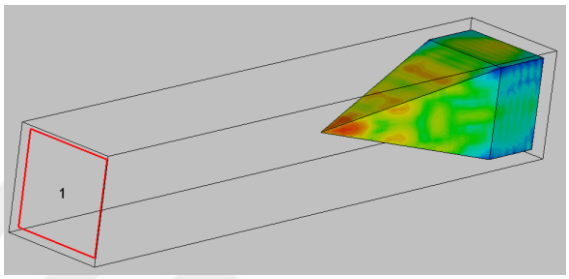
In order to investigate the power loss density, the single unit of pyramidal absorber is designed by using CST Microwave Studio software. The geometry and shape is based on dimensions of ETS- Lindgren EHP-8PCL Pyramidal Microwave Absorber. Figure 5.19 represents the power loss density of single pyramid absorber for C, Fe, Ni, Eccosorb and Teflon at the frequency of 15.2 Ghz. The Pyramidal absorbers have modeled as one port waveguide and backed with the metal. So the methods mentioned in Section 2.8 (reflection loss) are applied to test the absorption performance of the pyramidal absorbers. The port 1 is excitation port that transmits the 3D electromagnetic wave to the pyramidal absorber. The distance between the port and tip of the absorber was chosen as 30cm for each sample. The power scale bar displays the range of 0 and $5000 W/m^3$ (Figure 5.19.f). To conduct the power loss density of C, Fe and Ni sample the dielectric constants obtained from the measurement of the small foam samples in Section 3.4.2 are entered in the simulation.

The dielectric constants of Eccosorb SFU-9.5 and Teflon (Epsilon=2.1, the loss tangent=0.0002) are obtained from the material library of the software. For comparison, the power loss density of microparticle sample of C, Fe and Ni are exhibited together with the best and worst absorber material in the library which are Eccosorb and Teflon.

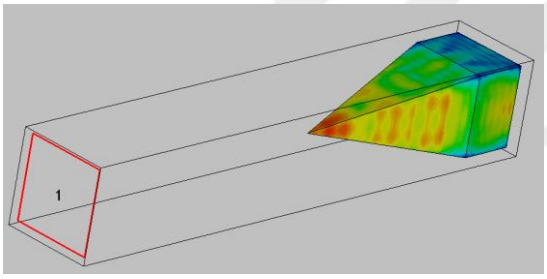
a) C



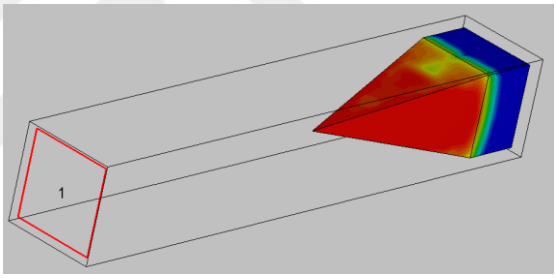
b) Fe



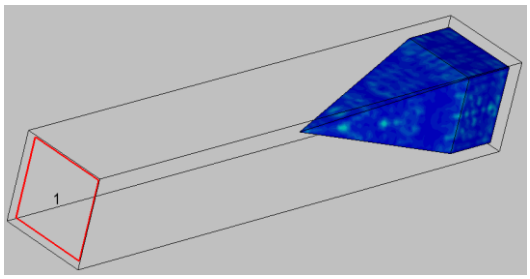
c) Ni



d) Eccosorb



e) Teflon



f) Power scale

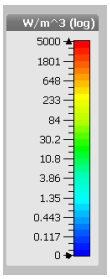


Figure 5.19. Power loss density (PLD), Simulation design and boundary conditions of single pyramid absorber based on Fe, Ni, C, Eccosorb and Teflon samples.

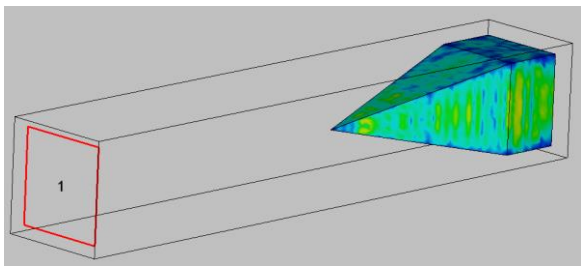
The red region on the surface of the pyramidal absorber indicates the best power loss according to the scale bar. As shown in Figure 5.19.e, the almost all surface of the Teflon pyramid is covered with dark blue region due to its low loss characteristics.

The Eccosorb absorber illustrates well power loss at the pyramid as the base shows the low power loss. The Figure 5.19.a shows that the power loss density for C absorber is high at the tip of the pyramid and it decreases while the electromagnetic wave propagates towards the base. The C absorber exhibits the power loss density higher than the other kind of pyramid absorber based on the microparticle. The maximum value of C, Fe, Ni, Eccosorb and Teflon is $17.32x10^3$, $17.47x10^3$, $17.1x10^3$, $154.4x10^3$, 1729, respectively.

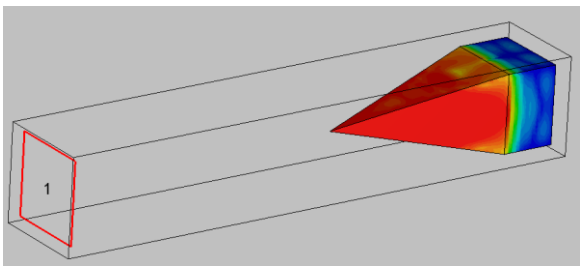
5.2.1.b Bulk

For comparison, the power loss density of Ba1, C and Fe pyramid microwave absorber is calculated by using the CST software, as shown in Figure 5.20. In this case, the dielectric constants of Ba1, C, Fe samples are described in Section 3.1.5 and 6.1. The maximum value of power loss density for Ba1, C and Fe is $11.44x10^3$, $117.4x10^3$, $154.9x10^3$ at 15.2 GHz. Clearly, the Ba1 pyramid absorber has very low absorption compared to the others. Therefore, the Ba1 hexaferrite nanoparticles can be used together C, Fe and Ni microparticles to make composite absorber.

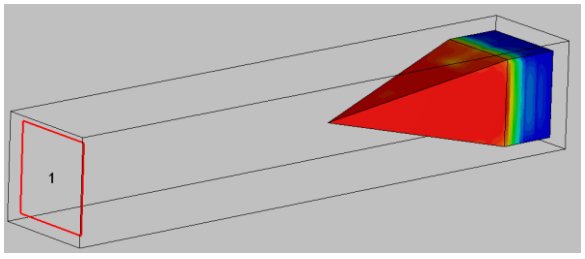
a) Ba1



b) C



c) Fe



d) Power scale

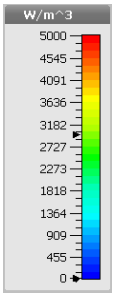


Figure 5.20. Power loss density (PLD), Simulation design and boundary conditions of single pyramid absorber for Ba1, C and Fe samples.

The above graphs (Figure 5.19.b and Figure 5.20.c) show the results of two kind of pyramidal absorber based on Fe powder which one of them is obtained from the foam small and other is obtained from the toroidal sample. It is observed from the comparison between two demonstrations of Fe pyramid absorber that the amount of absorption increases dramatically while the concentration of powder in the absorber increases.

5.2.2 NRL-Arch

In order to compare the simulation and measurement reults, the pyramid absorber can be designed with two antenna and metal plate. Figure 5.21 represents two port antenna and pyramid microwave absorber on the metal. While one port transmits the microwave, second port receive reflected wave from absorber or metal. There are two types of reflection in such a process : actual (Γ_a) and measured (Γ_m). The measured reflection coefficient is obtained by measurement via network analyzer. The actual reflection coefficient is achieved after free-space bistatic calibration which determines unknown error coefficients. For this reason, the simulation without absorber is realized while metal plate moves z=0, λ/8, λ/4 from the reference plane to calculate error coefficients. The 3D field view and S21 result for only metal plate are shown in Figure 5.22.(a) and 5.22.(b). The code which is written for calculation needed for calibration [149] is given Appendix E.

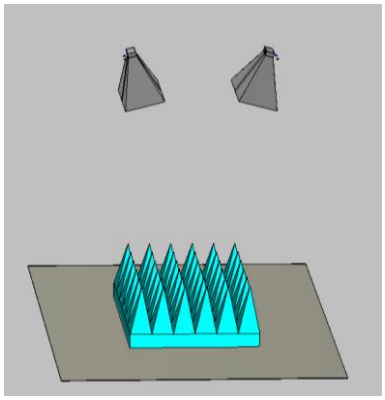


Figure 5.21. Modeling of reflectivity measurement setup in CST microwave studio.

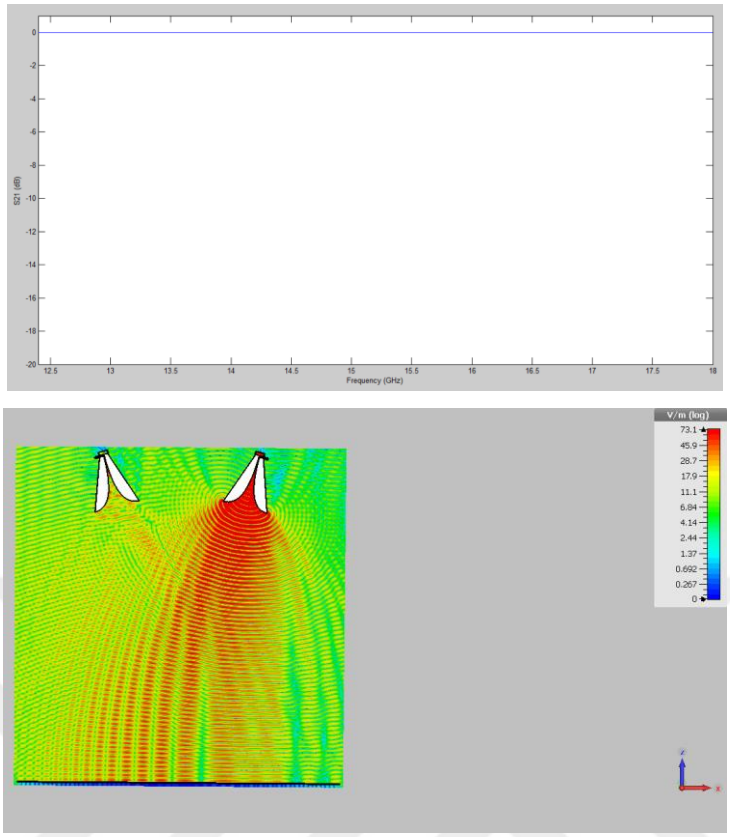


Figure 5.22. (a) S21 parameter and (b) 3D field on two dimensional plane for the metal plate case.

6. Results and Discussion

6.1. Toroidal Sample

The toroidal C, Fe and Ni samples with the thickness of 3mm are fabricated as described in Section 4.1. The TRL calibration and coaxial line technique (85050C APC7) as mentioned in Section 5.1.2 are used to calibrate the system and determine the dielectric and magnetic properties in the frequency range of 2 and 18 GHz. Two port measurement technique is applied to get the reflection and transmission coefficients S11, S21. The Agilent 85071E Materials Measurement Software calculates ε and μ parameters using the S11 and S21 coefficients. In this section, the microwave absorption calculated from the measurement values of S11 and S21 is examined. The reflection loss curve calculated from the dielectric and magnetic constants via Equations (2.117 and 2.118) for the thickness between 2 and 4 mm will be shown.

6.1.1 Carbonyl Iron (Fe)

The scattering parameter S11, S21, S22 and S12 observed from the measurement of coaxial line technique is shown in Figure 6.1.a. The value of the S21 parameter at 2 GHz is 0.78 and then it decreases exponentially to 0.1 as the frequency increases. The S11 and S22 parameter change between 0.4 and 0.55 in all frequency range. The both of them show a wavy characteristic at the lower frequency and increases gradually at the higher frequencies. The rapid change at the S11 parameter and the almost no change at S21 parameter point out that the microwave absorption will be much at the higher frequency. It can be seen from the figure that the transmission coefficients overlap each other while the reflection coefficients are separated from each other slightly. The reason that brings the small difference between the S11 and S22 parameter may be attributed to the surface imperfections in both face.

a) b)

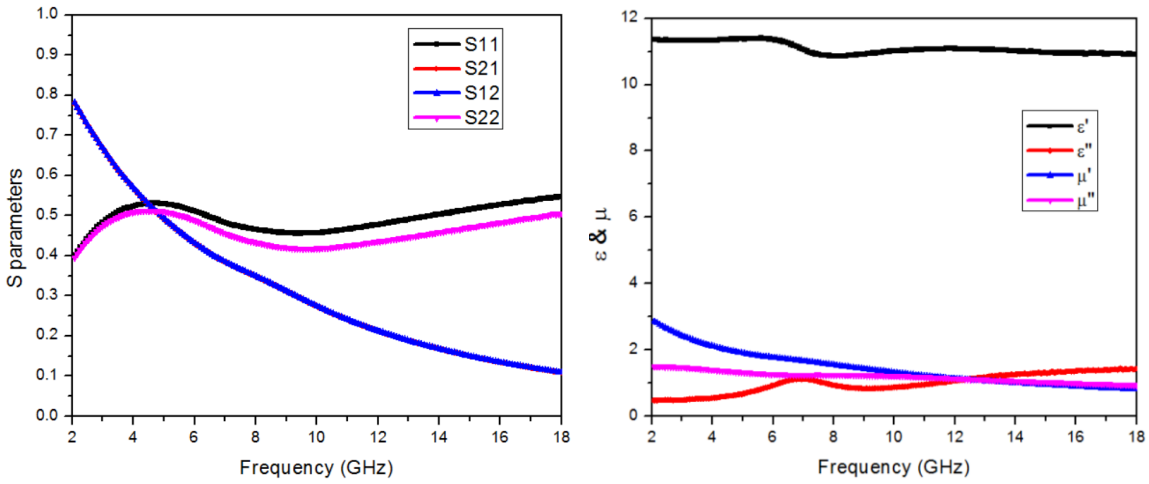


Figure 6.1. (a) Scattering parameters and (b) dielectric/magnetic constants of toroidal Fe sample in the frequency range between 2-18 GHz.

The Figure 6.1.b shows the variation in the permittivity and permeability for Fe toroidal sample at the frequency range of 2 - 18 GHz. The real $\varepsilon^{'}$ and imaginary $\varepsilon^{"}$ part of permittivity exhibit the resonance peak at about 7 GHz. The dielectric behavior of Fe sample can be described by "first order Debye model" [99]. The real part of permittivity $\varepsilon^{'}$ remains almost constant except of the resonant frequency. The imaginary part of permittivity $\varepsilon^{"}$ increases gradually with increasing frequency and it has the value of 1.43 at 18 GHz. The real part of permeability has the value of 3 at 2 GHz and then it decreases slowly. It is larger than the value of 1 in all frequency range. The imaginary part of permeability is between 1.48 and 1. It is assumed that the imaginary part of permeability has a relatively high value because of contribution of ferromagnetic particle.

a) b)

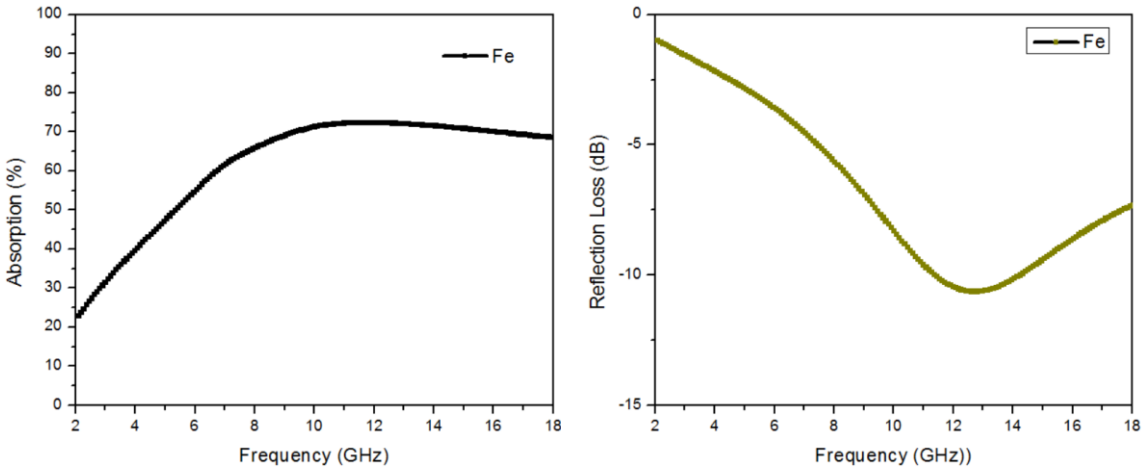


Figure 6.2 (a) Absorption and (b) reflection loss of toroidal Fe sample.

The absorption calculated from the S11 and S21 scattering parameters is shown in Figure 6.2.a. It should be noted that this absorption is obtained experimentally. No metal is placed at the back of the sample during measurement. It can be seen clearly that the absorption is increasing almost linearly up to 7 GHz and then after 11.5 GHz it decreases gradually to %68.6. The maximum value of the absorption is %72.5 at 11.5 GHz. The minimum value of absorption is %23 at 2 GHz. The reflection loss (in dB) curve calculated from the measured dielectric and magnetic constants is shown in Figure 6.2.b. Note that the reflection loss is obtained theoretically so that the sample backed metal plate is considered. The reflection loss curve has a dip at 12.7 GHz. This means that the minimum reflection and/or the maximum absorption of microwave power occur at this frequency value. In addition to this, the reflection loss curve is positioned at the top of the Figure 6.3 for comparison with the curve of matching thickness, the loss tangent and matching impedance (from top to bottom). The matching thickness decreases as the frequency increases and equals 3mm at the point of intersection. Since the thickness of the toroidal sample is 3mm, the point of intersection of two curves points the matching frequency corresponding to the matching thickness. That is, the matching thickness of toroidal Fe sample is 3mm at the intersection point. It can be seen from the figure that the matching frequency is about 12 GHz which is close to the frequency of maximum reflection loss. It is

observed that the magnetic loss tangent is larger than the dielectric loss tangent and it increases rapidly with increasing frequency. At this point, it is similar to the rectangular sample of Fe. Because the dielectric and magnetic loss tangent results of rectangular sample of Fe presents that the values of $\tan\delta_e$ is close to zero and the values of $\tan\delta_m$ is larger than the other samples. Therefore, the most of the absorption may be resulted from the magnetic loss tangent. The bottom graph in Figure 6.3 displays the real and imaginary part of effective impedance depending on the frequency. The real part of effective impedance is maximum and the imaginary part of effective impedance is minimum at about 12 GHz (Eq. 2.96 and 2.117). When the effective impedance is equivalent to 1, the reflectivity can be expected to be minimized and the electromagnetic wave can penetrate to the absorber because of matching at the surface. The absolute value of the effective impedance is 1 at 8 and 16 GHz. These frequencies are located at the left and right side of the resonance frequency on the spectrum. As a result, the matching thickness, the loss tangent and the matching impedance can be interpreted that these quantities defines the reflection loss peak where it occurs.

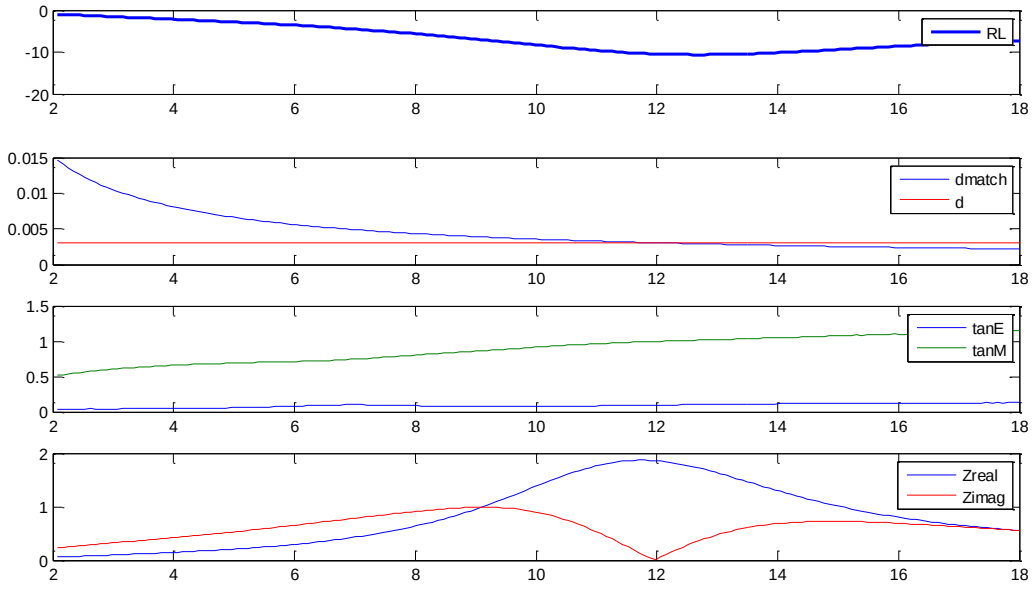


Figure 6.3. Reflection loss analysis graph for toroidal Fe sample. From top to bottom :

reflection loss, matching thickness, loss tangent and matching impedance.

The reflection loss values calculated (in Eq. 121) from dielectric constants for the thickness of between 2 and 4mm and in the frequency range of 2- 18 GHz is displayed in Figure 6.4. In general, while the thickness of sample increases, the reflection loss value varies slightly. According to the graph, the Fe sample exhibits the reflection loss value lower than -10 dB at the higher frequency between 12-18 GHz and at the thickness between 2 and 4mm. For the sample having the thickness of 3mm, the reflection loss is lower than -10 dB at the frequency between 12 and 14 GHz.

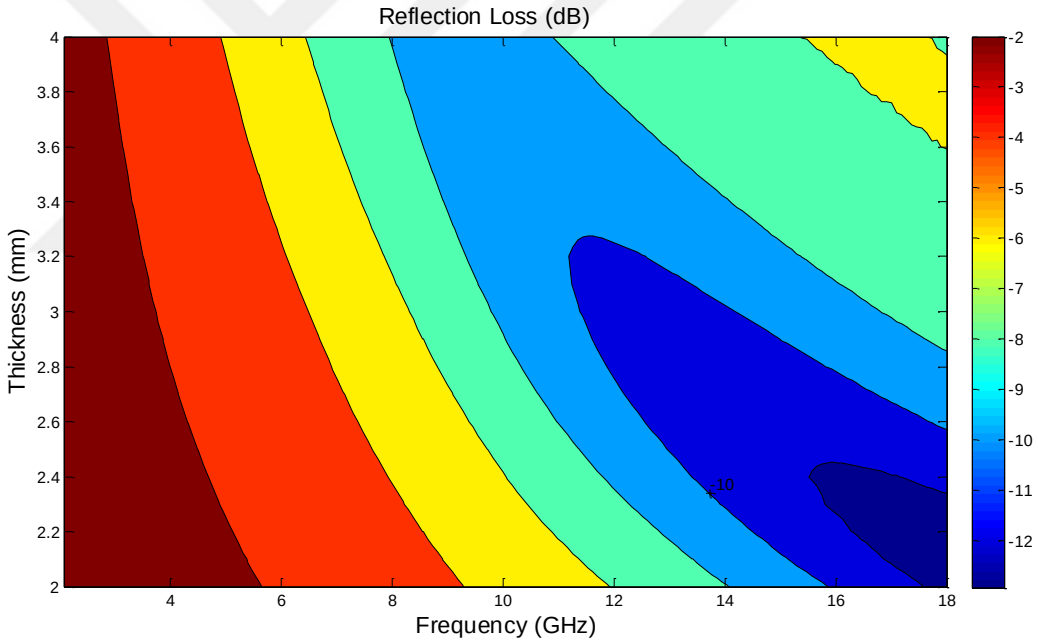


Figure 6.4. Contour graph of reflection loss for toroidal Fe sample.

6.1.2. Nickel (Ni)

The transmission and reflection coefficients of Ni toroidal sample are displayed in Figure 6.5.a. The value of reflection coefficients vary between 0.73 and 0.83. They are slightly different at the frequency between 4 and 16 GHz. They have a little peak at 3.5 GHz and after it decreases gradually up to 18 GHz. The small difference

between them may be result from that they have small different surface roughness on both side of the sample. The transmission coefficients S21 and S12 are exactly the same in all frequency range. However, they decreases exponentially from 0.5 to 0.1.

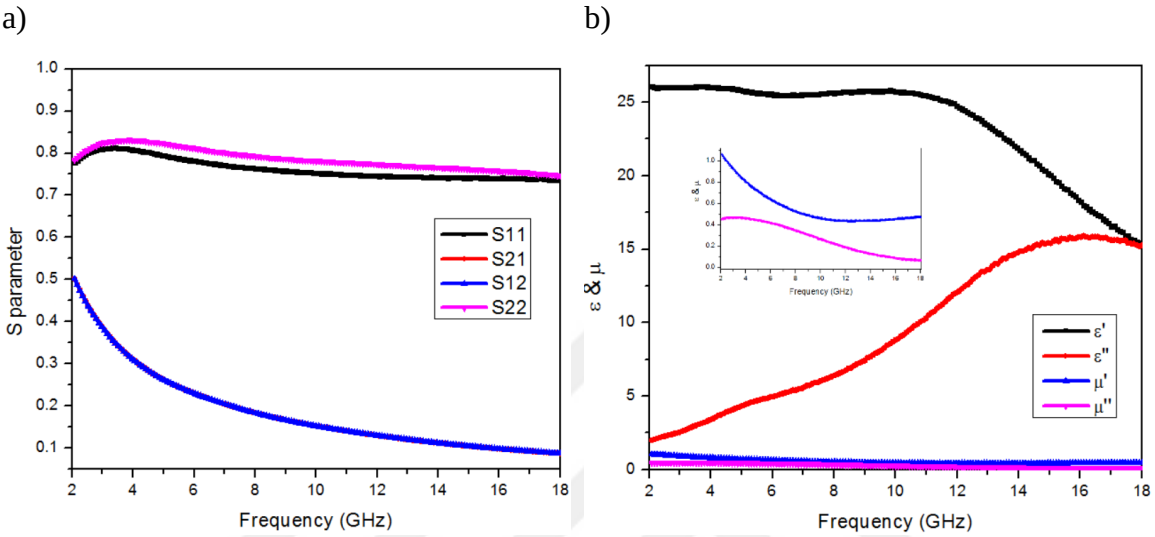


Figure 6.5. (a) Scattering parameters and (b) dielectric/magnetic constants of toroidal Ni sample in the frequency range between 2-18 GHz.

The plots of dielectric constant ε', ε'', μ', μ'' are shown in Figure 6.5.b. It is observed that the broad resonance peak appear at 16 GHz. At the 18 GHz, the dielectric loss tangent reaches to maximum value. While the real part of permittivity decreases at 11 GHz, the imaginary part of permittivity increases and it reaches to the maximum value at 16 GHz. So this type of behavior can be defined as the "first order Debye model". The value of permeability is small as compared to the Fe sample. The value of imaginary part of permeability varies from 0.5 to 0.1. The real part of permeability decreases rapidly up to 10 GHz and it remains almost constant.

a) b)

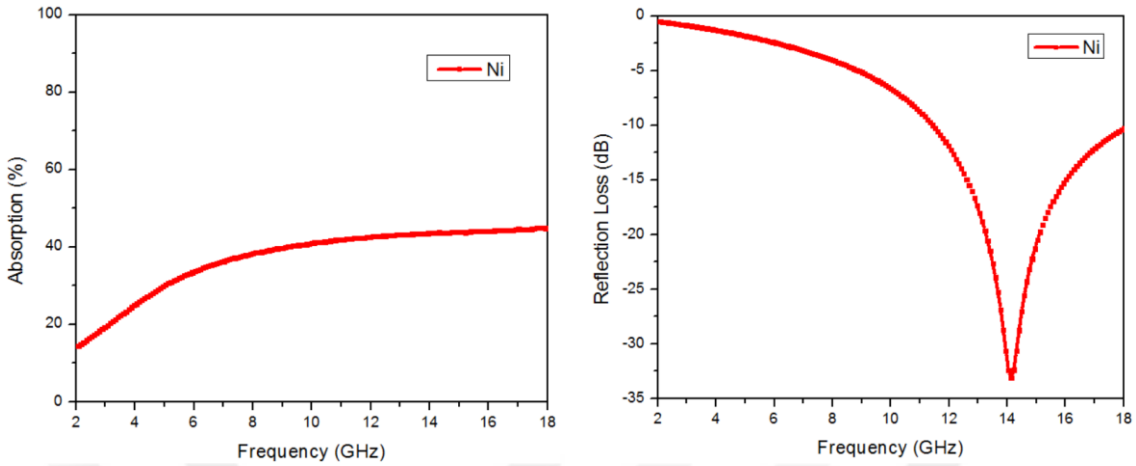


Figure 6.6. (a) Absorption and (b) reflection loss of toroidal Ni sample.

The microwave absorption given in term of the percent is obtained from the measurement value of S11 and S21, as shown in Figure 6.6.a. Firstly, the absorption for Ni sample increases linearly up to 6 GHz and then it increases gradually. The minimum value of absorption at 2 GHz is %14 and the maximum value of absorption at 18 GHz is %45. Because APC7 coaxial line technique is applied, the result of absorption is obtained with the help of the measurement technique which uses the sample backed without metal. The reflection loss is calculated by using the dielectric constants ε', ε'', μ', μ'' for the frequency range between 2-18 GHz, as shown in Figure 6.6.b. The value of the maximum reflection loss is -33 dB at 14.1 GHz. For below -10 dB, its bandwidth is 6.5 GHz. For below -20 dB, its bandwidth is approximately 1.8 GHz. At this point, the ratio of the reflected field to the incident field is 1/10. As a result, It can be said that the absorption of Ni sample higher than the absorption on Fe sample moreover it has deeper and broader reflection loss.

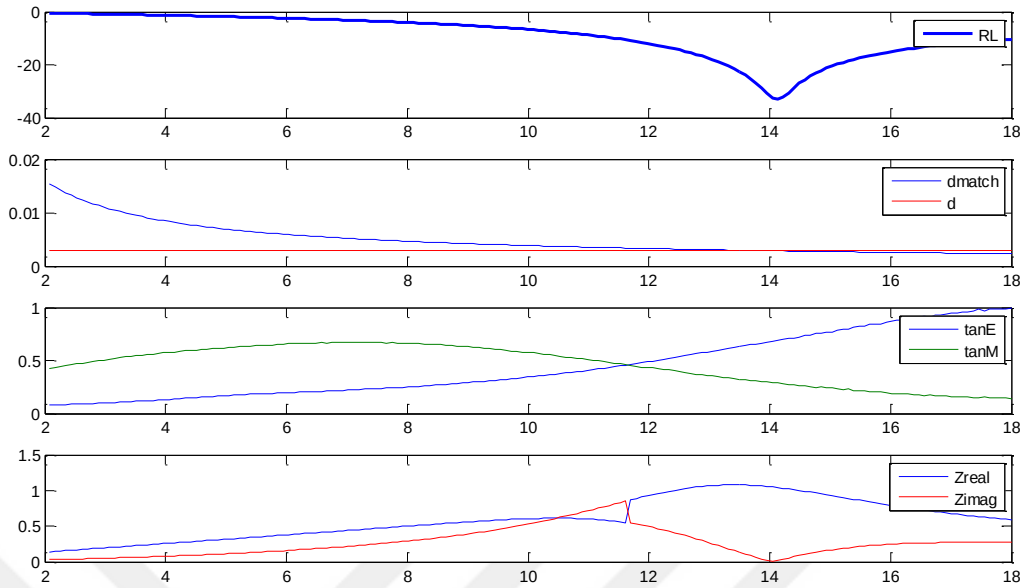


Figure 6.7. Reflection loss analysis graph for toroidal Ni sample.

The reflection loss can be evaluated with the help of matching thickness, the loss tangent and matching impedance, as shown in Figure 6.7. We can see from the figure, the matching thickness decreases exponentially as the frequency increases. At the resonant frequency, the matching thickness is nearly 3mm which corresponds to the thickness of the toroidal sample. It is observed that the electric loss tangent increases with the increasing frequency. Initially, the magnetic loss tangent increases gradually and after 8 GHz it decreases fastly. The magnetic loss tangent is dominant at the lower frequency as the electric loss tangent is dominant at the higher frequency. At 11.8 Ghz, the magnetic loss tangent line intersects with the electric loss tangent line. The value of matching impedance is 1 at about the resonant frequency.

The thickness and frequency dependent reflection loss map is shown in Figure 6.8. The reflectance of any absorber depends on the six parameter [158]: ε', ε'', μ', μ'', f ($frequency$) and t ($thickness$). Here, the reflection loss value is calculated for each thickness and frequency point using the dielectric parameter. In general, for all thickness of the sample the reflection loss value increases as frequency increases. But it decreases after a certain frequency point. For lower frequencies, the lower

reflection loss values are observed. They are approximately -5 dB in the frequency range of 2 and 6 GHz. From the figure, it is observed that the resonant frequency corresponds to the dark blue region. The path which made of these regions points out that the smaller sample causes the higher resonance frequency. At the same time, one can see the dark blue region is surrounded by regions having different color. This means that for a specific thickness there is one resonant frequency and then the reflection loss value begins to decreases towards other regions. It should be noticed that the dark blue region is positioned as close to the higher frequency. So this type of sample operates only in the range of 10 and 18 GHz for -20 dB or lower (dB) values. In addition to this, the thickness of the sample should be chosen between 2.4 and 4mm to obtain the resonance frequency.

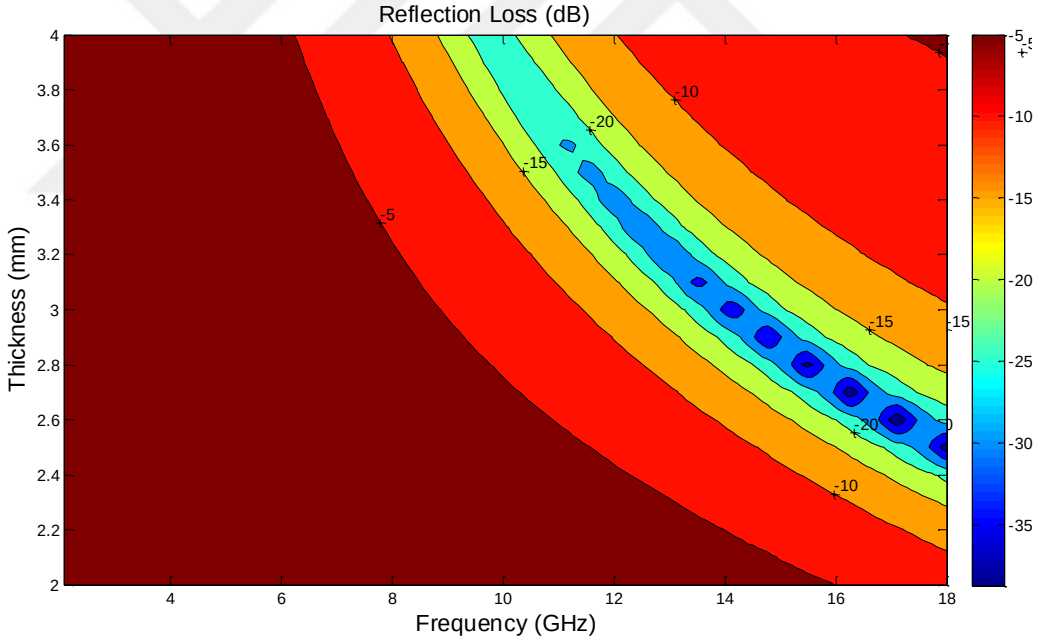


Figure 6.8. Contour graph of reflection loss for toroidal Ni sample.

6.1.3 Carbon (C)

The measurement result of the scattering parameter, dielectric and magnetic properties for C sample is shown in Figure 6.9. The transmission coefficients of S21 and S12 curves are exactly the same in all frequency spectra. They have a decreasing

trend from 0.6 to 0.2. The reflection coefficients of S11 and S22 are slightly different in the frequency range of 6 and 18 GHz. The values of reflection coefficients vary between 0.8 and 0.55. They exhibits distinct peak towards to lower frequencies and fall in between 10 and 16 GHz. More generally, they show a wavy curve. The Figure 6.9.b shows the dielectric and magnetic curves of toroidal C sample. For this sample, the zero value is assigned to the imaginary part of the permeability and the value of 1 is assigned to the real part of permeability due to the non-magnetic property. As expected the Debye relaxation, the real part of permittivity decreases while the imaginary part of the permittivity increases. The Debye relation is primarily determined by three parameters ε_{r0}, $\varepsilon_{r\infty}$ and τ [99]. Where τ is the relaxation time which is quite large for this sample. For all spectra, the real part of permittivity changes from 18.5 to 11.5 and the imaginary part of the permittivity changes from 4.5 to 9.6. In some cases, the dielectric plot is more complicated than the single relaxation [159]. Such sample may show multiple relaxation times so that each of them has different relaxation time. As shown in Figure 6.9.b, the curve of the imaginary part exhibits a wavy between 6 and 14 GHz. Therefore, it may be described with multiple relaxation times.

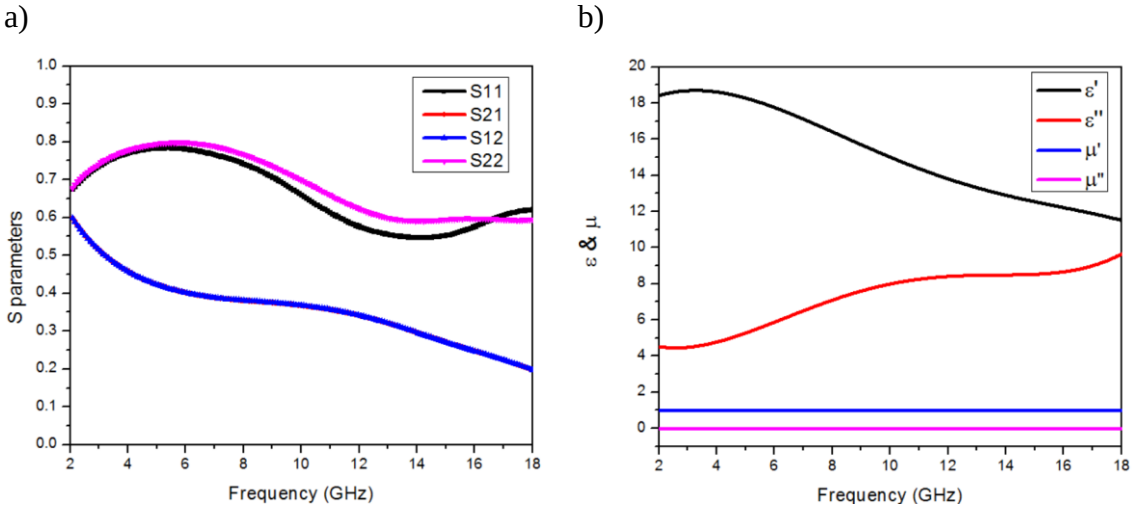


Figure 6.9. (a) Scattering parameters and (b) dielectric/magnetic constants of toroidal C sample in the frequency range between 2-18 GHz.

It can be seen from the Figure 6.10.a, the microwave absorption of C sample is larger at the higher frequencies while it is smaller at the lower frequencies. The maximum absorption is %78 at 14.76 GHz. The peak of the absorption can be result substantially from the sharp decrease in the S11 parameter. The behavior of the reflection loss is related to the curve of the absorption. The resonant occurs at the higher frequencies and the reflection loss value is close to x axis at the lower frequencies. The maximum reflection loss value is -9.9 dB at 14.6 GHz. The maximum reflection loss value of C sample is not good as compared the Fe and Ni sample. It cannot reach the values that is not better than -10 dB.

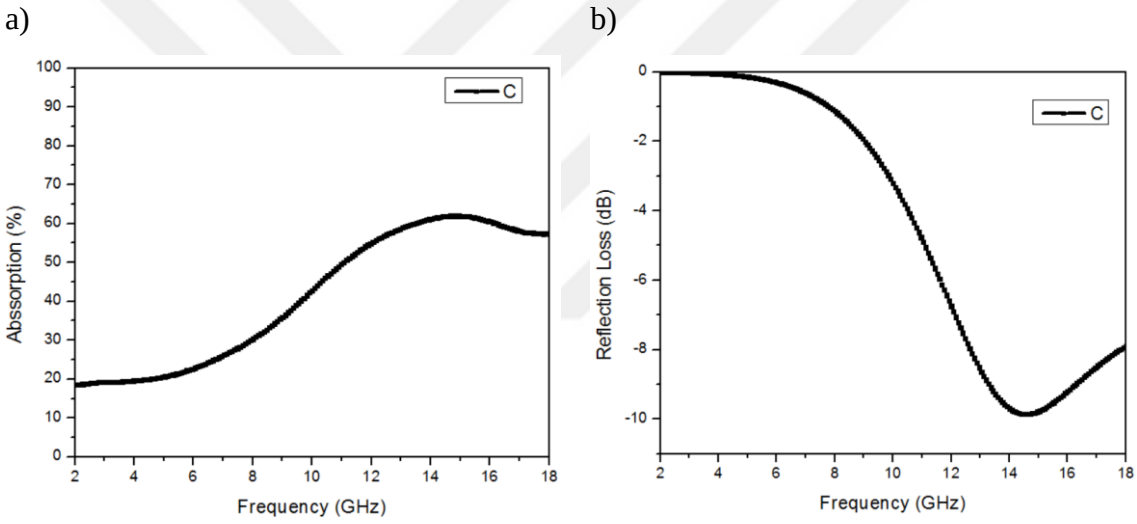


Figure 6.10. (a) Absorption and (b) reflection loss of toroidal C sample.

Figure 6.11 shows reflection loss, matching thickness, loss tangent and matching impedance plot for C sample. For the purpose of determining the reflection loss, the analysis method can be realized by using these plots. As we expect that the matching thickness decreases with increasing frequency. Its plot intersects with the line of 3mm at 13 GHz. Therefore, the maximum reflection may be expected at about 13 GHz. Because the C sample is non-magnetic, the loss magnetic tangent must be zero, as shown third plot in Figure. The dielectric loss tangent has increasing trend from 0.24 to 0.72. At the beginning, the real and imaginary part of the matching impedance

increases together. However the imaginary part of the matching impedance decreases and becomes to zero at 13 GHz. To examine in more detail, the absolute matching impedance (Zin) is calculated by using its imaginary and real part, as shown in Figure 6.12.a. It can be seen that, the value of the absolute matching impedance is 1 at 9 and 16.2 GHz.

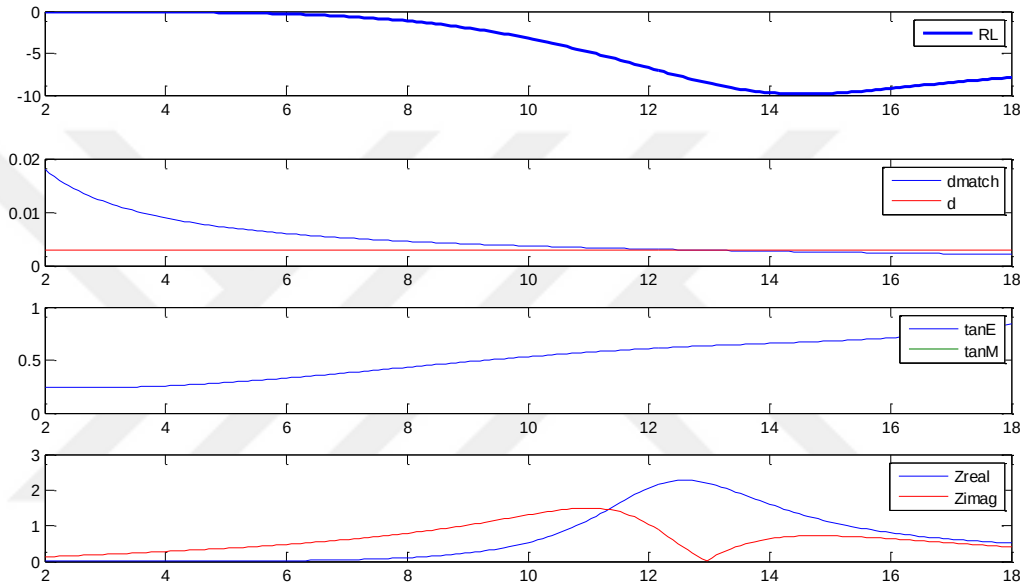


Figure 6.11. Reflection loss analysis graph for toroidal C sample.

The reflection loss graph with thickness dependent is given in Figure 6.12.b. In general, the reflection loss is not very well if it is compared with other samples. Especially, this sample cannot operate at the lower frequencies. For the frequencies between 2 and 8 GHz, the reflection loss can only reach -3 dB at the thickness between 2 and 4mm. At the higher frequencies, the dark blue region that represents the resonant frequencies occurs. The maximum reflection loss value can be obtained at the sample of the thickness between 2.2 and 2.8mm at frequencies between 16 and 18 GHz. As a result, It should be noticed that for the sample of Ni and C the

reflection loss is realized at the frequency corresponding to the relaxation and resonance of permittivity

a) b)

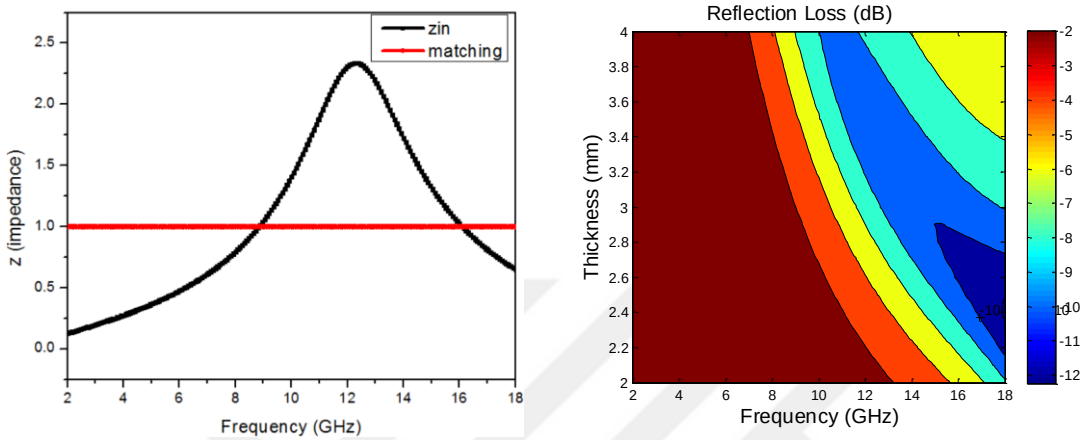


Figure 6.12. (a) Absolute impedance and (b) the contour graph of reflection loss for toroidal C sample

6.2 Pyramidal Absorbers

6.2.1 Conventional

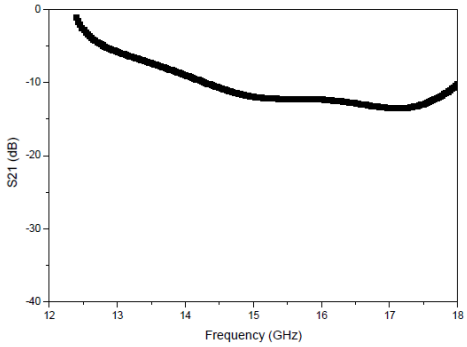
The pyramidal absorbers fabricated as conventional type are tested with NRL-Arch system which is installed in this project. The construction stage of this kind of absorber is described in Section 4.2.1. The pyramidal absorbers were placed at the center of the table of NRL-Arch measurement setup. The transmission coefficients (reflectivity-from first port to second port) of Fe, Ni, C, FeC, FeNi, NiC, FeNiC, A0, A1 and A12 sample were obtained with Network analyzer as shown in Figure 6.13. While the first port transmits the electromagnetic wave, the second port receives the reflection and scattering waves. As expected, the pyramidal shape of the absorber affects positively the reflectivity especially at the specific frequency.

The sample of A0, A1 and A12 represents the only foam, foam with anti-fire paint and foam with anti-fire solution, respectively. From the last plot in

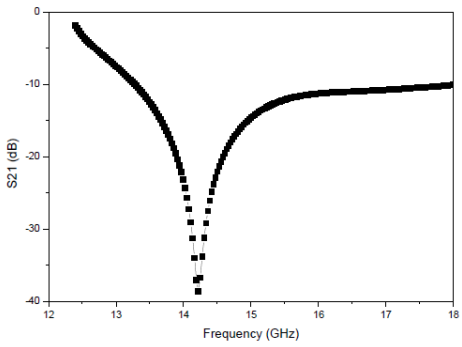
the Figure 6.13, the curve of reflectivity of the foam is close to zero in the frequency range of 12.4-16 GHz and declines slightly at the higher frequency. With the anti-fire paint the reflectivity changes less at the higher frequency. However, the reflectivity decreases with the increasing frequency at the case of foam with the anti-fire paint and solution. The drop in the reflectivity may be caused by the absorption of the particle of the anti-fire solution.

Among the all samples based on the microparticle, the pyramidal microwave absorber based on the Ni has the lowest reflectivity (first plot at right column in Figure 6.13) and the absorber based on the C has the highest reflectivity. The value of the reflectivity of Ni sample is -39 dB at 14.3 GHz. Its bandwidth is 0.5 GHz for below -20dB. But it is observed as 4.5 GHz for the value of reflectivity better (below) than -10dB. In general, the pyramidal absorber whose content includes the Ni particles shows good reflectivity at the certain frequency If it is compared with economic pyramidal absorber made of rice husk-rubber tire dust [160]. Other study points gets the minimum reflectivity of -25 dB by using carbon as absorbing material at frequency range of 1-10Ghz [161]. FeNi and NiC absorbers exhibits approximately reflectivity of -30dB at 16.6 and 15.2 GHz, respectively. Therefore, it can be understood that the resonant frequency changes by the absorber whose content replace from C particle to Fe particle. However, the pyramidal absorber included together with the Fe and C particles presents the curve of reflectivity that change slowly for all frequency range.

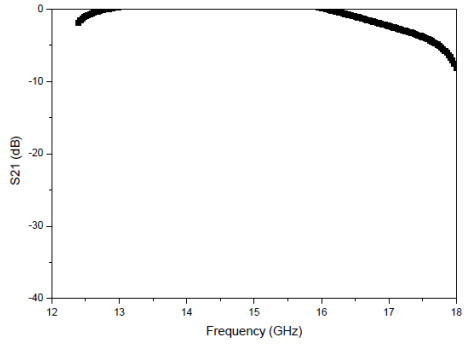
Fe



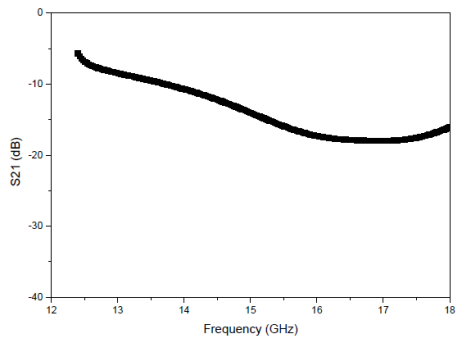
Ni



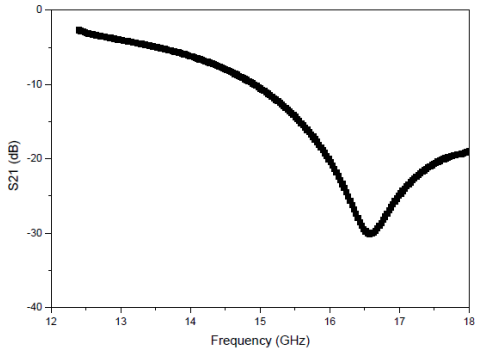
C



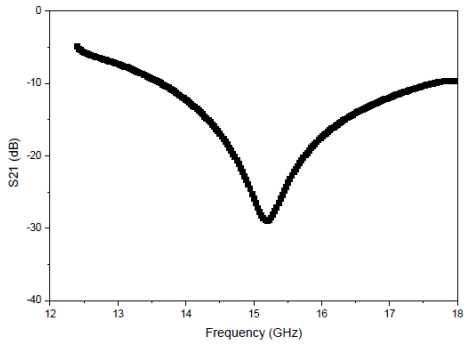
FeC



FeNi



NiC



FeNiC

A0,A1,A12

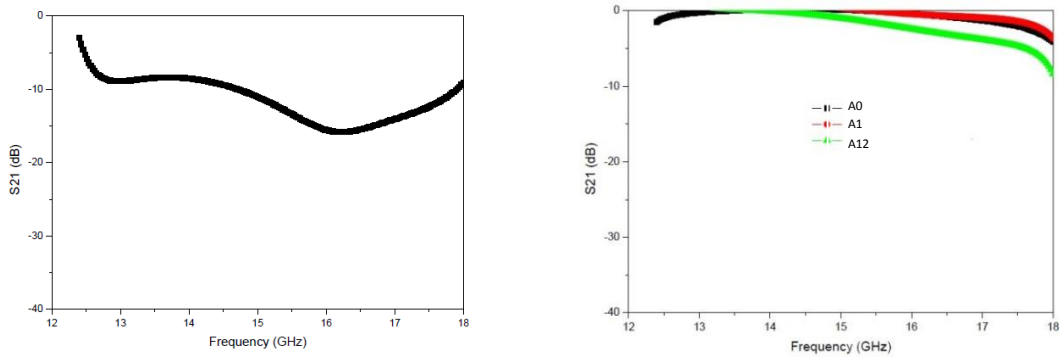


Figure 6.13. Measurement of reflectivity of conventional type absorber

6.2.2 New Design (Double Pyramidal Absorber)

The pyramidal absorbers which are new designed absorbers in this thesis were measured with the NRL-arch system. The absorbers used in the measurement are described in the Section 4.2.2. It consists of two parts which are bottom and top. The bottom parts based on the C/Fe/Ni microparticle are measured individually and together with each of the top parts of C/Fe/Ni as shown in Figure 6.14. The first column of the Figure indicates the S21 measurement result of the absorbers without the top parts. The pyramidal absorber based on the C sample performs relatively low reflectivity and has a small drop at 17.5 GHz. In addition to this, it is observed that the reflectivity of Fe pyramid is higher than the other pyramid.

The rows of the figure present the reflectivity plots related to the absorbers so that the each of the bottom part are fixed and are combined with varying top parts. When the bottom part of pyramidal absorber based on the C sample are combined with the top part of C/Fe/Ni sample, we observe that the resonant frequency occurs clearly at the lower or higher frequency. As for the absorber consist of the bottom part of the C and the top part of C, the resonant frequency shifts toward the lower frequency. In the case of the absorbers which have the bottom part of the C and top part of Fe/Ni, the resonant frequency shifts toward the higher frequency. *The second column* represents that the absorber with top part of C cause the reflectivity of about -20 dB level at the different frequency. For the pyramid absorber with bottom part of C, Fe and Ni the maximum reflectivity occur at 13.7, 14.8 and 16.9 GHz, respectively (C-C, Fe-C, Ni-C). *The third column* shows the case of pyramid absorber with top part based on Fe. All absorbers in this column shows the same minimum reflectivity value (-15 dB).

However, the frequency point in which the reflectivity is lowest shifts toward the lower value for the case that bottom and top part consist of Fe. For the fourth column, the value of the reflectivity is close to zero for the absorber with the bottom part of Fe. While the bottom part is chosen as the C based, the minimum reflectivity is obtained at the higher frequency. But, for this absorber the reflectivity is very high at the lower frequency.

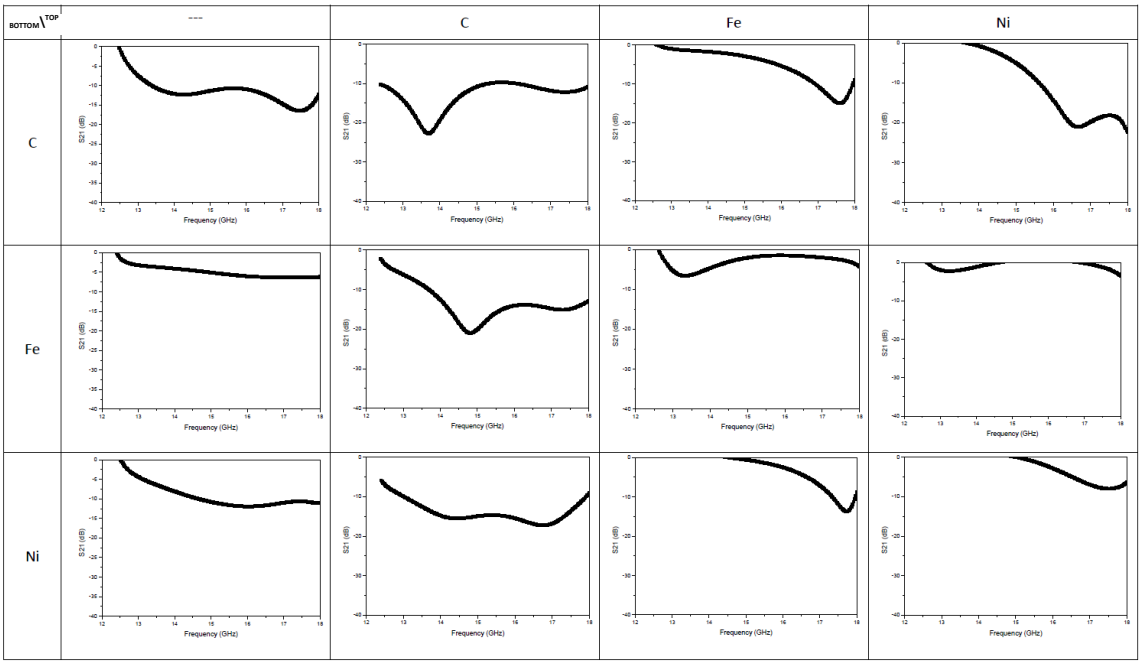


Figure 6.14. Measurement of reflectivity of double type pyramidal absorber.

For comparison, the reflectivity results of commercial ETS-Lindgren model flat and pyramidal absorber are given in Appendix F. The conventional absorbers Ni, NiC, FeNi and the double pyramidal absorber C-C, C-Ni, Fe-C investigated in this thesis show the value of reflectivity below -20 dB as the commercial flat absorber FL-0375. However, our results is not enough good according to Figure E.2 of commercial pyramidal absorber (in Appendix F). Because the synthesized BaM, SrM and PbM nanoparticles didn't used for producing conventional and double pyramidal absorbers. Although the pyramidal absorber doesn't contain nanoparticles, their reflectivity results are better than one of the commercial flat absorber and reach -40 dB value.

The XRD measurement of synthesized nano-hexaferrites ($BaFe_{12}O_{19}$, $SrFe_{12}O_{19}$, $PbFe_{12}O_{19}$) gives consistent results with the literature. VSM result shows that their saturation magnetization becomes less as the amount of PMMA increases. It can be result from that diamagnetic shell effect on the surface of the hexaferrite structure due to the PMMA polymer increasing. In this case, the dielectric parameter is much larger than the magnetic parameter. This may cause less absorption. The changing on the scattering parameter of Ba1, Ba2, Ba3, Sr1, Sr2, Sr3, Pb1, Pb2, Pb3 samples dependent on the changing PMMA is less. The absorption rate with this method can be improved if the PMMA ratio is reduced. Before the studying on the larger size absorber, firstly small piece can be cut from the absorber. Then the dielectric parameter can be used in the simulation work, after this piece is measured on rectangular or circular waveguide.

The NRL arch setup enables the reflectivity measurement of microwave dependent on the angular and frequency. This setup is made of inexpensive polyamide instead of metal to reduce cost and decrease the error reflection resulted from the metal arch. It can be constructed in the anechoic chamber and the absorber material can be attached on the wall of the arch to increase the measurement accuracy.

The reflection loss value of toroidal sample made of microparticles is calculated from their dielectric and magnetic parameter. It is difficult to determine the correct value because there is multiple root in the division of complex numbers during the calculation. Therefore, the reflection loss analysis technique can be used to avoid problems of determining reflection loss plot.

Conclusion

In this thesis, the nanoparticle hexaferrites were synthesized and magneto-polymeric materials were used as absorber in different mixture ratios to investigate "microwave/radar absorbing material". The effect of PMMA addition into the hexaferrites examined. The reflection and transmission of hexaferrite absorbers doesn't change much as PMMA:BaM/SrM/PbM ratio is 20/80, 40/60, 60/40. The multilayer absorber with x=1.3mm and y=0.15 whose configuration Fe-Ba1-Fe-Sr1-Fe-Pb1-Fe is found as the best after the parametric simulation. It can be used radar

absorbing material. The simulation results for rectangular sample based on microparticles are consistent with the measurement results. The reflection loss value of toroidal Ni sample is -33 dB. By using double pyramidal absorber, the reflectivity of C-C sample is greatly improved than the conventional pyramidal absorber of C. The C-C and Fe-C pyramid absorbers among all configurations are the best. They exhibit the value of reflectivity of about -23 dB at 13.7 and 14.8 GHz, respectively. Moreover, they have the quite same patterns of the curve. The result of this study is that the C-C, Fe-C and Ni, FeNi, NiC samples based on the inexpensive microparticles can be used as pyramidal absorbers in the anechoic chamber paint. For future work, sol-gel method with PMMA/BaM (ratios: 5/95, 10/90, 15/85) can be synthesized to increase reflection loss value. Then pyramidal absorber can be tested combining the C-C ,Fe-C microparticle with nanoparticle BaM/PMMA hexaferrites by using measurement and simulation.

REFERENCES

[1] P. B. Jana, A. K. Mallick, S. K. De, IEEE Trans. Electromagn. Compat. 34, 478 (1992).

[2] D. Micheli, R. Pastore, M. Marchetti , "Modeling of Radar Absorbing Materials Using Winning Particle Optimization Applied on Electrically Conductive Nanostructured Composite", Department of Astronautic, Electric and Energy, Sapienza University of Rome. 2012

[3] L. C. Folgueras, M. A. Alves , M. C. Rezende , "Microwave absorbing paints and sheets based on carbonyl iron and polyaniline: measurement and simulation of their properties".

[4] K. K. Mallick, P. Shepherd, R. J. Green, Journal of Magnetism and Magnetic Materials 312 (2007) 418–42.

[5] C. Sudakar, G.N. Subbanna, T.R.N. Kutty, Journal of Magnetism and Magnetic Materials 263 (2003) 253–268

[6] W. Y. Zhao, P. Wei, X. Y. Wu, W. Wang, and Q. J. Zhang, Journal Of Applıed Physıcs 103, 063902 2008

[7] C. Sudakar, G.N. Subbanna, T.R.N. Kutty, Journal of Magnetism and Magnetic Materials 268 (2004) 75–88

[8] Ping Shi, H. How, Xu Zuo, S. D. Yoon, S. A. Oliver, C. Vittoria, IEEE Transactıons On Magnetıcs, Vol. 37, No. 4, July 2001

[9] J. S. McCloy , K. Korolev, J. V. Crum, M. N. Afsar, IEEE Transactıons On Magnetıcs, Vol. 49, No. 1, January 2013

[10] B.K. Kuanr, V. Veerakumar, R.Marson, S.R. Mishra, R.E. Camley, Z. Celinski, Appl. Phys.Lett.94(2009)202505.

[11] R.A.Pawar, S.S.Desai, Q.Y. Tamboli, S. E. Shirsath, S.M. Patange, Journal of Magnetism and Magnetic Materials 378(2015)59–63.

[12] M. Jamalian, A. Ghasemi, E. Paimozd, Current Applied Physics 14 (2014) 909e915.

[13] G. Shen, M. Xub, Z. Xua, Materials Chemistry and Physics 105 (2007) 268–272

[14] O. Akman, Z. Durmus, H. Kavas, B. Aktas, U. Kurtan, A. Baykal, H. Sozeri, Phys. Status Solid A 210, No. 2, 395–402 (2013)

[15] Z. Zhanga, X. Liua, X. Wanga, Y. Wub, R. Li, Journal of Alloys and Compounds 525 (2012) 114– 119.

[16] S.K. Chawla, S.S. Meena, P. Kaur , R.K. Mudsainiyan, S.M. Yusuf, Journal of Magnetism and Magnetic Materials 378(2015)84–91

[17] J. Qiu, L. Lan, H. Zhang, M. Gu, Journal of Alloys and Compounds 453 (2008) 261–264

[18] D. C. Kulkarni, V. Puri, Electronic Materials Letters, Vol. 7, No. 1 (2011), pp. 51-57

[19] A. Baniasadi, A. Ghasemi, A. Nemati, M. A. Ghadikolaei, E. Paimozd, Journal of Alloys and Compounds 583 (2014) 325–328

[20] Esmail Kiani, Amir S.H. Rozatian, Mohammad H. Yousefi, J Supercond Nov Magn (2013) 26:733–738

[21] A. Drmota,J. Koselj, M. Drofenik, A. Znidarsic, Journal of Magnetism and Magnetic Materials 324(2012)1225–1229

[22] J.R. Liu, R.Y. Honga, W.G. Feng, D. Badami, Y.Q. Wang, Powder Technology 262 (2014) 142–149

[23] Z.F. Zi, Y.P. Sun, X.B. Zhu, Z.R. Yang, J.M. dai, W.H. Song, Journal of Magnetism and Magnetic Materials

[24] S. Kolev, T. Koutzarova, A. Yanev, C. Ghelev, I. Nedkov, Institute of Electronics, Bulgarian Academy of Sciences, 72, Tzarigradsko Chaussee, 1784 Sofia, Bulgaria

[25] S.P. Gairola, Vivek Verma, A. Singh, L.P. Purohit, R.K. Kotnal, Solid State Communications 150 (2010) 147151

[26] L. Wang, J. Zhang, Q. Zhang, N. Xu, J. Song, Journal of Magnetism and Magnetic Materials 377(2015)362–367

[27] F. Yakuphanoglu, A. Al.Ghamdi, F. El-Tantawy, Microsyst Technol DOI 10.1007/s00542-014-2394-2

[28] S. Katlakunta, S. S. Meena, S. Srinath, M. Bououdina, R. Sandhya, K. Praveena, Materials Research Bulletin 63 (2015) 58–66

[29] M. C. Dimri, S. C. Kashyap, D. C. Dube, Ceramics International 30 (2004) 1623–1626

[30] M. C. Dimri, R. Stern, S. C. Kashyap, K. P. Bhatti, D. C. Dube, P hys. Status Solidi A 206, No. 2, 270–275 (2009)

[31] N. Koga, T. Tsutaoka, Journal of Magnetism and Magnetic Materials 313 (2007) 168–175

[32] J. Qiu, Q. Zhang, M. Gu and H. Shen, Journal of Applied Physics 98, 103905 (2005); 10.1063/1.2135412

[33] J. Qiu, Y. Wang, M. Gu, Materials Letters 60 (2006) 2728–2732

[34] J. Qiua, M. Gua, H. Shen, Journal of Magnetism and Magnetic Materials 295 (2005) 263–268

[35] G. Mu, X Pan, N. Chen, K. Gan, M. Gu, Materials Research Bulletin 43 (2008) 1369–1375

[36] V. B. Brega, "Advantages of Ferromagnetic Nanoparticle Composites in Microwave Absorbers"

[37] Z. Zheng, H. Zhang, IEEE Transactıons On Magnetıcs, VOL. 49, NO. 7, JULY 2013

[38] R. Sharma, R.C. Agarwala, V. Agarwala, Materials Letters 62 (2008) 2233–2236

[39] P. Singh, V. K. Babbar, A. Razdan, S. L. Srivastava, V. K. Agrawal, T. C. Goel, J Mater Sci (2006) 41:7190–7196.

[40] A. Ghasemi, A. Hossienpour, A. Morisakod, A. Saatchi, M. Salehi, Journal of Magnetism and Magnetic Materials 302 (2006) 429–435

[41] Priyono and A. Manaf, ICICI-BME 2009 Proceedings

[42] F. M. M. Pereira, M. R. P. Santos, R. S. T. M. Sohn, J. S. Almeida, A. M. L. Medeiros, M. M. Costa, A. S. B. Sombra, J Mater Sci: Mater Electron (2009) 20:408–417

[43] S. Pignarda, H. Vincent, E. Flavin, F. Boust, Journal of Magnetism and Magnetic Materials 260 (2003) 437–446

[44] C. Li, B. Wang, J. Wang, Journal of Magnetism and Magnetic Materials 324(2012)1305–1311

[45] Y. Kim, S. Kim, J Electroceram (2010) 24:314–318 DOI 10.1007/s10832-009-9575-x

[46] A. Ghasemi, X. Liuc, A. Morisako, Journal of Magnetism and Magnetic Materials 316 (2007) e105–e108

[47] S.K. Chawla, S.S. Meena, Prabhjoyt Kaur, R.K.Mudsainiyan, S.M.Yusuf, Journal of Magnetism and Magnetic Materials 378(2015)84–91

[48] A. Drmota, J.Koselj, M.Drofenik, A. Znidarsic, Journal of Magnetism and Magnetic Materials 324(2012)1225–1229

[49] G. Reza Gordani, A. Ghasemi, A. Saidi, Ceramics International40(2014)4945–4952

[50] M. Asghari,A. Ghasemi, E. Paimozd, A. Morisako, Materials Chemistry and Physics 143 (2013) 161e166

[51] X. Shen, F. Song, X. Yang, Z. Wang, M. Jing, Y. Wang, Journal of Alloys and Compounds 621 (2015) 146–153

[52] N. Chen, K. Yang, M. Gu, Journal of Alloys and Compounds 490 (2010) 609–612

[53] N. Chen, G. Mu, X. Pan, K. Gan, M. Gu, Materials Science and Engineering B 139 (2007) 256–260

[54] A. Sharbati, J. M. V. Khani, G. R. Amiri, Solid State Communications 152 (2012) 199–203

[55] M. J. Iqbal, M. N. Ashiq, I. H. Gul, Journal of Magnetism and Magnetic Materials 322(2010)1720–1726

[56] X. Pan, G. Mua, H. Shen, M. Gu, Applied Surface Science 253 (2007) 4119–4122

[57] B.T. Shirk, W.R. Buessem, J. Appl. Phys. 40 (1969) 1294–1296

[58] Kojima H. In: Wohlfarth EP, editor. Ferromagnetic materials, vol.3. Amsterdam: North-Holland Physics Publishing; 1982.p. 305–91

[59] Emerson, W. H. IEEE Trans. Antennas Propag. 1973, AP-21, 484.

[60] Machinerieen, N. V., FR Patent 802728. 1936.

[61] SAVILLE P., HUBER T., MAKEIFF D., “Fabrication of Organic Radar Absorbing Materials”; Technical Report DRDC Atlantic TR 2005-124, May 2005

[62] O. Luukkonen, F. Costa, A. Monorchio, S. A. Tretyakov, “A Thin Electromagnetic Absorber for Wide Incidence Angles and Both Polarizations”.

[63] K. J. VINOY, R. M. JHA, "Trends in radar absorbing materials technology", Computational Electromagnetics Lab, Aerospace Electronics&Systems Division, National Aerospace Laboratories, Bangalore 560017, India

[64] S.B. Bibikov, E.I. Kulikovskij, A.M. Kuznetsov, V.N. Gorshenev, V.V. Orlov, M.V. Prokof'jevin, Second International Workshop on Ultrawideband Ultrashort Impulse Signal Proceeding UWBUSIS, 2004, p. 129.

[65] P.B. Jana, A.K. Mallick, S.K. De, IEEE Trans. Electromagn. Compat. 34 (4) (1992) 478.

[66] M.A. Soloman, P. Kurian, M.R. Anantharaman, P.A. Joy, Polym. Plast. Technol. Eng. 43 (4) (2004) 1013.

[67] B.S. Zhang, Y. Feng, J. Xiong, Y. Yang, H.X. Lu, IEEE Trans. Magn. 42 (7) (2006) 1778

[68] S.P. Gairola, Vivek Verma, A. Singha, L.P. Purohitb, R.K. Kotnala, "Modified Composition Of Barium Ferrite To Act As A Microwave Absorber In X-Band Frequencies", Solid State Communications Volume 150, Issues 3–4, January 2010, Pages 147–151

[69] X. Yu, G. Lin, D. Zhang, H. He, "An Optimizing Method For Design Of Microwave Absorbing Materials".

[70] Fernandez A, Valenzuela A. "General solution for single-layer electromagnetic wave absorber". Electron Lett 1985;21(1):20–1.

[71] Leendert J du Toit. The design of Jauman absorbers. IEEE Antennas Propag Mag 1994;36(6):17–25.

[72] Zhao H, Qin B, Hu D, Qin R. "The design rules for single-layer radar absorbings". J Harbin Univ Technol 1993;25(2):104–10.

[73] Mahmoud SF, Habib MK. "Design of a two layer microwave absorber. J Electromagnet Wave". 1998;12(8):1005–14.

[74] Valenzuela AQ, Fernandez Anibal F. "General design theory for single-layer homogeneous absorber". IEEE Trans Anttennas Propag 1996;44(7):822–6.

[75] Z.J. Fan, G.H. Luo, Z.F. Zhang, L. Zhou, F. Wei, Mater. Sci. Eng. B 132 (2007) 85–89.

[76] S. Ruan, B. Xu, H. Suo, F.Wu, S. Xiang, M. Zhao, J. Magn. Magn. Mater. 212 (2000) 175–177.

[77] V.K. Babbar, A. Razdan, R.A. Puri, T.C. Goel, J. Appl. Phys. 87 (2000) 4362–4366.

[78] A. Verma, A.K. Saxena, D.C. Dube, J. Magn. Magn. Mater. 263 (2003) 228–234.

[79] D.L. Zhao, X. Li, Z.M. Shen, J. Alloys Compd. (2008).

[80] Y. Fan, H. Yang, X. Liu, H. Zhu, G. Zou, J. Alloys Compd. 461 (2008) 490–494.

[81] D.L. Zhao, X. Li, Z.M. Shen, Mater. Sci. Eng. B 150 (2008) 105–110.

[82] R.A. Stonier, SAMPE J. 27 (1991) 9–18.

[83] J.Q. Wei, Z.Q. Zhang, B.C. Wang, T. Wang, F.S. Li, J. Appl. Phys. 108 (2010) 123908.

[84] R.K.Srivastava, T.N.Narayanan, A.P.ReenaMary, M.R.Anantharaman, A.Srivastava, R.Vajtai, P.M.Ajayan, Appl.Phys.Lett.99(2011) 113116.

[85] N. Tian, J.W.Wang, F.Li, Z.Mei, Z.X.Lu,L.L.Ge,C.Y.You,J.Magn.Magn.Mater. 324 (2012)4175–4178.

[86] Z.H. Yang, Z.W.Li, Y.H.Yang, L.Liu, L.B.Kong, J.Magn.Mater.331(2013) 232–236.

[87] Z.W.Li, Z.H.Yang, L.B.Kong, Appl.Phys.Lett.96(2010)092507.

[88] T.H.Ting, K.H.Wu, J.Magn.Magn.Mater.322(2010)2160–2166.

[89] G. Dash, Ampyx LLC, "How RF Anechoic Chambers Work"

[90] X.Tong, "Advanced Materials and Design for Electromagnetic Interference Shielding", 2009,CRC Press Taylor & Francis Group, CHAPTER 9

[91] Dong Il Kim, Dae Hun Kim, Dong Han Choi, "Design of a super wide-band EM wave absorber for a general purpose anechoic chamber", Department of Radio Science and Engineering, Korea Maritime University, Pusan 606-791, Republic of Korea

[92] Bryan F. Lawrance, "Anechoic Chamber, Past and Present", Conformity Magazine, February 2005

[93] Emerson, W. H. IEEE Trans. Antennas Propag. 1973, AP-21, 484.

[94] Vinoy, K. J.; Jha, R. M. Sadhana 1995, 20, 815.

[95] Petrov, V. M., Gagulin, V.V. Inorganic Materials 2001, 37, 93.

[96] Lederer, P. G. "An Introduction to Radar Absorbent Materials (RAM)"

[97] Christopher L. Holloway, Ronald R. Delyser, Robert F. German,Paul McKenna, Motohisa Kanda, "Comparison of Electromagnetic Absorber Used in Anechoic and Semi Anechoic chambers for Emissions and Immunity Testing of Digital Devices". IEEE Transactions on Electromagnetic compability, vol 39, no1, February 1997

[98] Halpern, O., Johnson, M. H. J.; Wright, R. W., US Patent 2951247. 1960.

[99] Salisbury, W. W., US Patent 2599944. 1952

[100] S.J. Orfanidis, Electromagnetic Waves and Antennas, (Rutgers University, June 21, 2004).

[101] GRIFFITHS D.J., Introduction to Electrodynamics (3rd Edition), Published: January 9th 1999 by Benjamin-Cummings Publishing Company.

[102] POZAR D.M., Microwave Engineering, 3rd Edition John Wiley & Sons, Inc. 2005

[103] CHEN L. F., ONG C. K., NEO C. P., VARADAN V. V. and. VARADAN V. K. , "Microwave Electronics Measurement and Materials Characterization", 2004 John Wiley & Sons, Ltd ISBN: 0-470-84492-2, 2004.

[104] Agilent, "Basics of Measuring the Dielectric Properties of Materials, Application note", www.agilent.com/find/materials

[105] D. W. Hess, "Introductıon To RCS Measurements", 1125 Satellite Boulevard, Suite 100 Suwanee, GA 30024, U.S.A.

[106] H.Nornikman,F.Malek,P.J.Soh,A.A.H Azremi, "Reflection Loss Performance of Hexagonal Base Pyramid Microwave Absorber using Different Agricultural Waste Material"

[107] S. Imai, K. Taguchi ,T. Kashiwa ,T. Tabata, K. Kubo, E. Satou, "Effect of Incident Angle on Temperature Characteristics in Pyramidal Radiowave Absorber"

[108] H. Nornikman, P.J Soh, A.A.H Azremi, M.S Anuar, "Performance Simulation of Pyramidal and Wedge Microwave Absorbers"

[109] H. Nornikman, F. Malek, P.J Soh, A.A.H Azremi, A. Ismahayati, "Reflection Loss Performance of Triangular Microwave Absorber"

[110] F. Malek, Z. Liyana, F.H. Wee, H. Nornikman, "Reflection Loss Performance of Double Pyramidal Microwave Absorber".

[111] W.Duan, H. Chen, M. Sun, Y. Ding, X. Sun, C. Cai, X.Sun, "A Composite Electromagnetic Absorber for Anechoic Chambers"

[112] M.Park, J. Choi,S. Kim," Wide Bandwidth Pyramidal Absorbers of Granular Ferrite and Carbonyl Iron Powders"

[113] H. Nornikmanl, P. Sohl, F Malek, A.A.H Azremi , F.H Wee , R.B Ahmad , "Microwave Wedge Absorber Design using Rice Husk An Evaluation on Placement Variation", 2010 Asia-Pacific International Symposium on Electromagnetic Compatibility, April 12 - 16,2010, Beijing, China

[114] M. W. B. Silva , L.C. Kretly, "A New Concept of RAM-Radiation Absorbent Material: Applying Corrugated Surfaces to Improve Reflectivity"

[115] David C. Jenn, Radar and Laser Cross Section Engineering, AIAA, 1995

[116] Eugene F. Knott, John F. Schaeffer, Michael T. Tuley, Radar Cross Section, 2nd edition, Artech House, 1993

[117] B. Erenoglu, "Naval Postgraduate School Anechoıc Chamber Evaluatıon", 2004,42-43

[118] L. Chi, C. Wei, S. Bor, "The Optimum Design of Electromagnetic Wave Anechoic Chamber and Performance Analysis".

[119] C. L. Holloway, R.R. DeLyser, R. F. German, P. McKenna, M. Kanda, "Comparison of Electromagnetic Absorber Used in Anechoic and Semi-Anechoic Chambers for Emissions and Immunity Testing of Digital Devices", IEEE Transactıons On Electromagnetıc Compatıbılıty, VOL. 39, NO. 1, FEBRUARY 1997 33

[120] Ibrahim, N. Yaakob, M. Husain, S. Meng Se, A.Shaaban, "The Effect of the Carbon to the S11 Measurement on the Pyramidal Microwave Absorbers"

[121] Y. Huang, K. Boyle, "Antennas From Theory To Practice", John Wiley & Sons Ltd,1st Edition,2008

[122] "Design and İmplementation aspects of a small anechoic room and sound-actuation system", J.G. Rodriguez, 2010-2011, Erasmus Hogeschool Brussel

[123] D. Kim, D. Kim, D. Choi, "Design of a super wide-band EM wave absorber for a general purpose anechoic chamber", Current Applied Physics 7 (2007) 457–462

[124] LECTURE 8: Basic Methods in Antenna Measurements, McMaster University, http://www.ece.mcmaster.ca/faculty/nikolova/antenna_dload/current_lectures/

[125] Nicolson, A. M. and Ross, G. F. (1970). "Measurement of the intrinsic properties of materials by time domain techniques", IEEE Transactions on Instrumentation and Measurement, 19 (4), 377–382.

[126] Ghodgaonkar, D. K. Varadan, V. V. and Varadan, V. K. (1990)."Free-space measurement of complex permittivity and complex permeability of magnetic materials at microwave frequencies", IEEE Transactions on Instrumentation and Measurement, 39, 387–394.

[127] M. W. B. Silva, L. C. Kretly, "A New Concept of RAM-Radiation Absorbent Material: Applying Corrugated Surfaces to Improve Reflectivity"

[128] Y. Naıto, K. Suetake, "Application of Ferrite to Electromagnetic Wave Absorber and Its Characteristics". IEEE trans. microwave Eng. Theory Tech., 65, 19, 1971.

[129] T. Wang , C. Pan, Y. Wang, G. Tan, H. Wang, R. Li, F. Li, "Improvement of absorption performance for Co_2Z barium ferrite composite by increasing the reflected electromagnetic wave from air–absorber interface", Journal of Magnetism and Magnetic Materials 354(2014)12–16

[130] G. Mu, N. Chen, X. Pan, H. Shen, M. Gu, "Preparation and microwave absorption properties of barium ferrite nanorods", Materials Letters 62 (2008) 840–842

[131] X. Tang, Y.G. Yang, Materials Science-Poland, Vol. 27, No. 2, 2009

[132] Guohong M., Xifeng P., Na C., Keke G., Mingyuan G., Materials Research Bulletin 43 (2008) 1369–1375

[133] Robert C. Pullar, "Hexagonal ferrites: A review of the synthesis, properties and applications of hexaferrite ceramics", Progress in Materials Science 57 (2012) 1191–1334

[134] B.T. Shirk, W.R. Buessem, J. Appl. Phys. 40 (1969) 1294–1296

[135] Y.Y. Meng, M.H. He, Q. Zeng, D.L. Jiao, S. Shukla, R.V. Ramanujan, Z.W. Liu, Journal of Alloys and Compounds 583 (2014) 220–225

[136] P. Singh, V.K. Babbar, A. Razdan, T.C. Goel, S.L. Srivastava, "Magnetic, dielectric and microwave absorption studies of Ba-CoTi hexaferrite–Epoxy composites", Indian Journal of Pure & Appl Phys 42:221 March 2004

[137] Kojima H. In: Wohlfarth EP, editor. Ferromagnetic materials, vol.3. Amsterdam: North-Holland Physics Publishing; 1982.p. 305–91

[138] KITTEL C., Rev. Mod.Phys. 21, 541, 1949

[139] Diaz S, Suarez N, Faloh JC, Sanchez JC, Leccabue F, Watts BE, et al. J Phys IV 1997;7:C1–333

[140] Study on matching map for the absorber filled by metallic magnetic particles, T. Wang, F. Xu, L. Tang, L. Qiao, F. Li, Journal of Applied Physics 116, 173912 (2014)

[141] Akman Ö., "Investigating The Microwave Absorber Nanoparticles", PHD thesis, GTU 2012

[142] Microwave Absorber Selection Guide, ETS-Lindgren, Rantec Microwave Absorber

[143] R.E. Hiatt, E.F. Knott, T.B.A. Senior, "A Study of VHF Absorbers and Anechoic Rooms", The University of Michigan 5391-1-F

[144] D. Micheli, C. Apollo, R. Pastore, R. B. Morles, M. Marchetti, G. Gradoni, "Electromagnetic Characterization of Composite Materials and Microwave Absorbing Modeling",

[145] R. S. Biscaro, E. L. Nohara, G. G. Peixoto, R. Faez, M. C. Rezende, "Performance Evaluation of Conducting Polymer Paints as Radar Absorbing Materials (RAM)"

[146] "NRL Arch Reflectivity Test Setup Technical Bulletin 101", MAST Technologies

[147] I. Noordin, H. A. Idris, M. N. Taib, J. Sharif, A. Rosli, A. Zanal, A. T. Abdullah, "Investigation of Oil Palm Ash Microwave Absorber for Broadband Application", 2012 IEEE 8th International Colloquium on Signal Processing and its Applications

[148] C. R. Brito, A. A. Lubiano, N. Hui, D. Arakaki, "Absorber Foam Characterization For Predicting Overall Anechoic Chamber Performance",

[149] Stephen A. Brumley, “Evaluation Of Microwave Anechoic Chamber Absorbing Materials”, Arizona State University, May 1988

[150] M. H. Umari, D. K. Ghodgaonkar, V.V. Varadan, V. K. Varadan, “A Free-Space Bistatic Calibration Technique for the Measurement of Parallel and Perpendicular Reflection Coefficients of Planar Samples.”

[151] Y.S. Lee, F. Malek, E.M. Cheng, W.W. Liu, F.H. Wee, M. N. Iqbal, Z. Liyana,"An Experimental Thickness of Microwave Absorber Effect Absorption in Ku-band Frequency”.

[152] Dennis M. Sullivan, Electromagnetıc Sımulatıon Usıng The Fdtd Method, Second Edition WILEY

[153] Main Features of CST MICROWAVE STUDIO®

[154] G. Mu, X Pan, N. Chen, K. Gan, M. Gu, Materials Research Bulletin 43 (2008) 1369–1375

[155] Y.S. Lee, F. Malek, E.M. Cheng, W.W. Liu, F.H. Wee, M. N. Iqbal, Z. Liyana, Farrah Salwani Abdullah, “Difference Loss Tangent Layer Microwave Absorber Effect Absorption in X-band Frequency”.

[156] Y.S. Lee, F. Malek, E.M. Cheng, W.W. Liu, F.H. Wee, M. N. Iqbal, Z. Liyana, M.N.A Karim, M. F. H. A. Malek, “An Experimental Thickness of Microwave Absorber Effect Absorption in Ku-band Frequency”

[157] Y. Z. Cheng, Y. Nie, Z. Z. Cheng, R. Z. Gong, “Dual-band Circular Polarizer and Linear Polarization Transformer Based on Twisted Split-Ring Structure Asymmetric Chiral Metamaterial”, Progress In Electromagnetics Research, Vol. 145, 263-272, 2014

[158] P. Singh, V. K. Babbar, A. Razdan, S. L. Srivastava, V. K. Agrawal, T. C. Goel, “Dielectric constant, magnetic permeability and microwave absorption studies of hot-pressed Ba-CoTi hexaferrite composites in X-band”

[159] Shodghang , “Theory of Dielectrics”, Chapter 2.

[160] F. Malek, H. Nornikman, O. Nadiah, “Pyramidal Microwave Absorber Design from Waste Material using Rice Husk and Rubber Tire Dust” , ISSN: 2180 - 1843 Vol. 4 No. 1 January - June 2012.

[161] I. M. Ibrahim, N. Yaakob, M. Husain, S. Se, A. Shaaban, “The Effect of the Carbon to the S11 Measurement on the Pyramidal Microwave Absorbers”. 2011

IEEE Symposium on Wireless Technology and Applications (ISWTA), September 25-28, 2011, Langkawi, Malaysia

APPENDIX

Appendix A

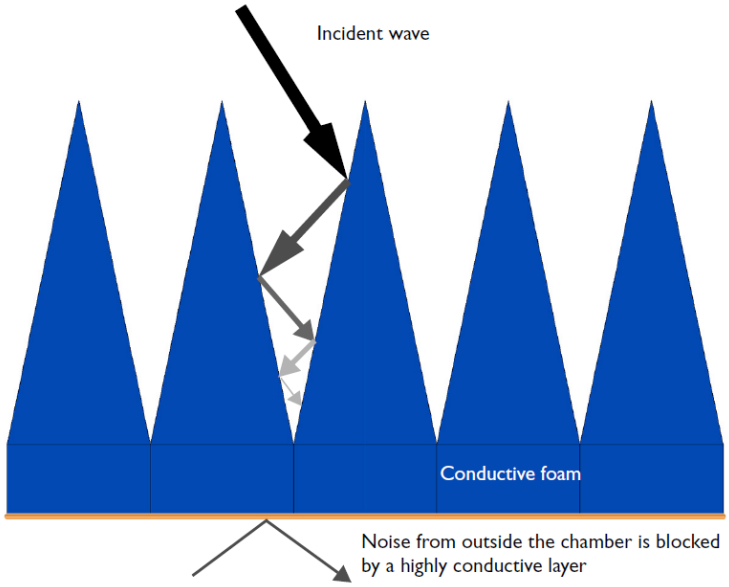


Figure A.1. The representation of absorption in pyramidal absorber due to the multiple reflections.

Appendix B

Table B.1. The model of antenna waveguide, frequency range,VSWR

Model	WG Size	Frekans Aralığı (GHz)		VSWR	insertion length (inch)	insertion length (mm)
PNR 22/28-2-6-6	WR22 to WR28	33	40	1.17	2	5.08
PNR 28/34-4-6-6	WR28 to WR34	26.5	33	1.17	4	10.16
PNR 34/42-4-6-6	WR34 to WR42	22	26.5	1.17	4	10.16
PNR 42/51-4-6-6	WR42 to WR51	18	22	1.1	4	10.16
PNR 62/75-4-6-6	WR62 to WR75	12.4	15	1.08	4	10.16
PNR 75/90-5-6-6	WR75 to WR90	10	12.4	1.08	5	12.7

Table B.2. The features of antennas and far-field distances.

R BAND								
WG Size	Frequency	Gain	Width		Long side (inch)	Short side (inch)	Far Field (m)	FAR FIELD CALCULATION
			E Plane	H Plane				
WR430	1.70 - 2.60	10	64.8°	45.4°	8	4	0.47 - 0.72	0.894621867
WR430	1.70 - 2.60	15	33.1°	32.0°	11.6	8.3	0.98 - 1.51	2.275135235
WR430	1.70 - 2.60	20	17.3°	17.4°	22	16	3.54 - 5.42	8.275252267
D BAND								
WG Size	Frequency	Gain	Width		Long side (inch)	Short side (inch)	Far Field (m)	
			E Plane	H Plane				
WR340	2.20 - 3.30	10	60.0°	49.3°	5.71	3.43	0.31 - 0.46	0.629752289
WR340	2.20 - 3.30	15	32.2°	30.8°	9.45	6.69	0.85 - 1.27	1.90276342
WR340	2.20 - 3.30	20	18.5°	16.3°	18.79	11.81	3.34 - 5.01	6.99087918
S BAND								
WG Size	Frequency	Gain	Width		Long side (inch)	Short side (inch)	Far Field (m)	
			E Plane	H Plane				
WR284	2.60 - 3.95	10	50.8°	54.1°	4.33	3.46	0.21 - 0.32	0.521917128
WR284	2.60 - 3.95	15	31.0°	30.6°	7.96	5.83	0.71 - 1.08	1.653908413
WR284	2.60 - 3.95	20	17.2°	16.5°	15.57	10.67	2.71 - 4.12	6.052811593
E BAND								
WG Size	Frequency	Gain	Width		Long side (inch)	Short side (inch)	Far Field (m)	
			E Plane	H Plane				
WR229	3.30 - 4.90	10	58.6°	51.9°	3.62	2.36	0.19 - 0.28	0.393558783
WR229	3.30 - 4.90	15	32.7°	32.4°	6	4.41	0.51 - 0.76	1.168581276
WR229	3.30 - 4.90	20	17.1°	16.7°	12.25	8.6	2.13 - 3.16	4.721324966
G BAND								
WG Size	Frequency	Gain	Width		Long side (inch)	Short side (inch)	Far Field (m)	
			E Plane	H Plane				
WR187	3.95 - 5.85	10	55.0°	54.1°	2.89	2.12	0.14 - 0.21	0.32323387
WR187	3.95 - 5.85	15	33.8°	33.3°	4.88	3.57	0.40 - 0.60	0.919877322
WR187	3.95 - 5.85	20	18.9°	19.2°	8.92	6.53	1.35 - 2.00	3.074887205
F BAND								
WG Size	Frequency	Gain	Width		Long side (inch)	Short side (inch)	Far Field (m)	
			E Plane	H Plane				
WR159	4.90 - 7.05	10	59.8°	48.3°	2.68	1.58	0.15 - 0.22	0.293485607
WR159	4.90 - 7.05	15	31.3°	30.8°	4.33	3.15	0.40 - 0.57	0.8693891
WR159	4.90 - 7.05	20	14.3°	16.9°	9.8	7.64	2.03 - 2.91	4.682088184
C BAND								
WG Size	Frequency	Gain	Width		Long side (inch)	Short side (inch)	Far Field (m)	
			E Plane	H Plane				
WR137	5.85 - 8.20	10	55.1°	54.2°	2.02	1.48	0.10 - 0.14	0.221163257
WR137	5.85 - 8.20	15	33.7°	33.2°	3.42	2.5	0.29 - 0.41	0.632947035
WR137	5.85 - 8.20	20	18.7°	18.8°	6.26	4.57	0.99 - 1.38	2.118681784
H BAND								
WG Size	Frequency	Gain	Width		Long side (inch)	Short side (inch)	Far Field (m)	
			E Plane	H Plane				
WR112	7.05 - 10.0	10	56.8°	55.2°	1.63	1.18	0.08 - 0.11	0.174163093
WR112	7.05 - 10.0	15	32.4°	32.0°	2.93	2.15	0.26 - 0.37	0.568059079
WR112	7.05 - 10.0	20	19.3°	19.3°	4.97	3.64	0.75 - 1.06	1.632276305
BAND								
WG Size	Frequency	Gain	Width		Long side (inch)	Short side (inch)	Far Field (m)	
			E Plane	H Plane				
WR102	7.00 - 11.0	10	55.5°	54.1°	1.58	1.14	0.07 - 0.12	0.17959534
WR102	7.00 - 11.0	15	29.6°	29.3°	3.04	2.23	0.28 - 0.44	0.672512633
WR102	7.00 - 11.0	17	26.2°	25.3°	3.6	2.54	0.39 - 0.61	0.918396443
WR102	7.00 - 11.0	20	17.0°	16.7°	5.57	3.94	1.00 - 1.57	2.202290219
X - BAND								
WG Size	Frequency	Gain	Width		Long side (inch)	Short side (inch)	Far Field (m)	
			E Plane	H Plane				
WR90	8.20 - 12.4	10	48.5°	47.4°	1.58	1.15	0.09 - 0.13	0.203674259
WR90	8.20 - 12.4	15	29.3°	29.0°	2.66	1.95	0.25 - 0.38	0.580164173
WR90	8.20 - 12.4	20	16.1°	16.5°	4.87	3.62	0.84 - 1.27	1.963798739

X - P BAND								
WG Size	Frequency	Gain	Width		Long side (inch)	Short side (inch)	Far Field (m)	
			E Plane	H Plane				
WR75	10.0 - 15.0	10	50.2°	49.2°	1.26	0.92	0.07 - 0.10	0.157031944
WR75	10.0 - 15.0	15	35.4°	28.5°	2.25	1.33	0.22 - 0.33	0.440734602
WR75	10.0 - 15.0	20	16.3°	17.2°	3.88	2.98	0.65 - 0.97	1.544177557
P BAND								
WG Size	Frequency	Gain	Width		Long side (inch)	Short side (inch)	Far Field (m)	
			E Plane	H Plane				
WR62	12.4 - 18.0	10	55.3°	50.9°	1	0.68	0.05 - 0.08	0.113217838
WR62	12.4 - 18.0	15	30.1°	31.2°	1.69	1.3	0.15 - 0.22	0.351955425
WR62	12.4 - 18.0	17.5	23.0°	24.5°	2.19	1.72	0.25 - 0.37	0.600347186
WR62	12.4 - 18.0	20	18.8°	18.9°	2.88	2.11	0.44 - 0.64	0.986823833
P - K BAND								
WG Size	Frequency	Gain	Width		Long side (inch)	Short side (inch)	Far Field (m)	
			E Plane	H Plane				
WR51	15.0 - 22.0	10	55.1°	54.2°	0.77	0.56	0.04 - 0.06	0.085776173
WR51	15.0 - 22.0	15	32.0°	31.8°	1.36	1	0.12 - 0.17	0.269639031
WR51	15.0 - 22.0	20	16.9°	18.0°	2.51	1.93	0.41 - 0.51	0.948600253
K BAND								
WG Size	Frequency	Gain	Width		Long side (inch)	Short side (inch)	Far Field (m)	
			E Plane	H Plane				
WR42	18.0 - 26.5	10	58.0°	57.0°	0.6	0.44	0.03 - 0.04	0.063098368
WR42	18.0 - 26.5	15	31.3°	31.5°	1.14	0.85	0.10 - 0.15	0.230475453
WR42	18.0 - 26.5	16	27.9°	27.9°	1.29	0.96	0.13 - 0.19	0.294713604
WR42	18.0 - 26.5	20	17.5°	17.8°	2.13	1.56	0.35 - 0.52	0.794485508
K-Ka BAND								
WG Size	Frequency	Gain	Width		Long side (inch)	Short side (inch)	Far Field (m)	
			E Plane	H Plane				
WR34	22.0 - 33.0	10	54.1°	53.2°	0.53	0.39	0.03 - 0.04	0.061457942
WR34	22.0 - 33.0	15	23.1°	40.8°	0.95	0.7	0.09 - 0.13	0.197644766
WR34	22.0 - 33.0	20	17.0°	17.4°	1.76	1.29	0.29 - 0.44	0.675852842

Ka BAND								
WG Size	Frequency	Gain	Width		Long side (inch)	Short side (inch)	Far Field (m)	
			E Plane	H Plane				
WR28	26.5 - 40.0	10	54.2°	54.4°	0.42	0.315	0.02 - 0.03	0.04741926
WR28	26.5 - 40.0	15	32.1°	31.3°	0.76	0.55	0.07 - 0.10	0.151414751
WR28	26.5 - 40.0	20	16.7°	18.3°	1.38	1.01	0.22 - 0.33	0.503138779

Appendix C

Table C.1. Waveguide frequency bands and interior dimensions

Frequency Band	Waveguide Standard	Frequency Limits (GHz)	Inside Dimensions (mm)
R band	WR-430	1.70 to 2.60	109.22 x 54.61
D band	WR-340	2.20 to 3.30	86.36 x 43.18
S band	WR-284	2.60 to 3.95	72.136 x 34.036
E band	WR-229	3.30 to 4.90	58.166 x 29.21
G band	WR-187	3.95 to 5.85	47.5488 x 22.1488
F band	WR-159	4.90 to 7.05	40.386 x 20.193
C band	WR-137	5.85 to 8.20	34.8488 x 15.7988
H band	WR-112	7.05 to 10.00	28.4988 x 12.6238
X band	WR-90	8.2 to 12.4	22.86 x 10.16
X-P band	WR-75	10.0 to 15.0	19.05 x 9.525
P band	WR-62	12.4 to 18.0	15.7988 x 7.8994

K band	WR-51	15.0 to 22.0	12.954 x 6.477
K band	WR-42	18.0 to 26.5	10.668 x 4.318
Ka band	WR-28	26.5 to 40.0	7.112 x 3.556
Q band	WR-22	33 to 50	5.6896 x 2.8448

Appendix D

Table D.1. Agilent 85071E Materials Measurement Software, Technical Overview

Software models

Model name	Measured S-parameters	Number of samples	Optimum sample thickness[1]	Results	Comments
Refl/Tran μ **&** ε (Nicolson-Ross)	S_{11}, S_{21}, S_{12}, S_{22} (or S_{11}, S_{21})	1	$\lambda_g/4$	ε_r^* & μ_r^*	Fast, but has nλ/2 discontinuities. Best for magnetic, short or lossy MUTs
Refl/Tran ε (NIST Precision)	S_{11}, S_{21}, S_{12}, S_{22}	1	$n\lambda_g/2$	ε_r^*	Accurate, no discontinuities. Best for long, low-loss MUTs
Refl/Tran ε (Fast)	S_{21}, S_{12}, (or S_{21})	1	$n\lambda_g/2$	ε_r^*	Similar to precision but faster and better for lossy MUTs Best for long, low-loss MUTs
Refl ε (Short-backed)	S_{11}	1	$\lambda_g/2$	ε_r^*	Best for liquids or powders
Refl ε (Arbitrary-backed)	S_{11}	1	$\lambda_g/2$	ε_r^*	Best for thin films
Refl μ_r & ε_r (Single/Double)	S_{11}	1[2]	$\lambda_g/4$[3]	$\varepsilon_r^*$and μ_r^*	Best for liquids or powders

Appendix E

```
clear all;clc;

%%%%% Calibration %%%%%%%
% all reflection for calibration standarts
gamma=load('calib_stdt.txt');
%Frequency points
f=gamma(:,1)*1e9;
% reflection for metal
gam0=gamma(:,2)+j*gamma(:,3);
% reflection for metal with distance lambda/8
gam8=gamma(:,4)+j*gamma(:,5);
% reflection for metal with distance lambda/4
gam4=gamma(:,6)+j*gamma(:,7);

%%%%%%% Measurement of S21 with Absorber
S21abr=load('absorber_real.txt');
S21meas=S21abr(:,2)+j*S21abr(:,3);
```

```
%S21meas=gam0; %for calibration test
%incoming parameter
c=3e8;
theta=pi/12;              % Arch angle
wl0=c./f;                 % wavelength in free space
wlc=c/15.2e9;             % center wavelength
wlz=wl0/cos(theta);
Beta=2*pi./wlz;           % phase change coefficient
N=length(f);
z=[0 wlc/8 wlc/4];
% actual reflection coefficient for metal z=0,lambda/8,lambda/4
for j=1:3
   for i=1:N
   gama(i,j)=(j*tan(Beta(i,1)*z(j))-1)/(j*tan(Beta(i,1)*z(j))+1);
   end
end
% measured or simulated reflection coefficient for metal z=0,lambda/8,lambda/4
Meas=[gam0 gam8 gam4];

   for k=1:N
   A(:,:,k)= [gama(k,3) 1 -gama(k,1)*Meas(k,1);gama(k,2) 1 -gama(k,2)*Meas(k,2);
       gama(k,1) 1 -gama(k,3)*Meas(k,3)];

   B(:,1,k)= [Meas(k,1); Meas(k,2); Meas(k,3)];
   end

   %error coefficients a,b,c
for m=1:N
X(:,:,m)=inv(A(:,:,m))*B(:,:,m);
end
   %actual reflection coefficient for absorber
for i=1:N
   S21act(i)=(S21meas(i)-X(2,1,i))./(X(1,1,i)-X(3,1,i)*S21meas(i));
end

plot(f/1e9,20*log10(abs(S21act)));
axis([12.4 18 -20 1]);xlabel('Frequency (GHz)');ylabel('S21 (dB)');
```

Appendix F

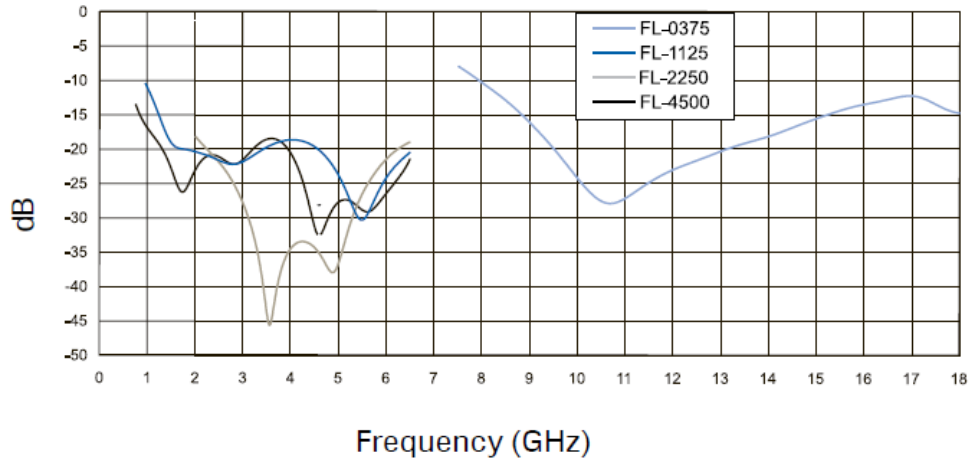


Figure E.1. The reflectivity results of flat laminate absorber FL-0375, FL-1125, FL-2250, FL-4500 model for ETS-Lindgren.

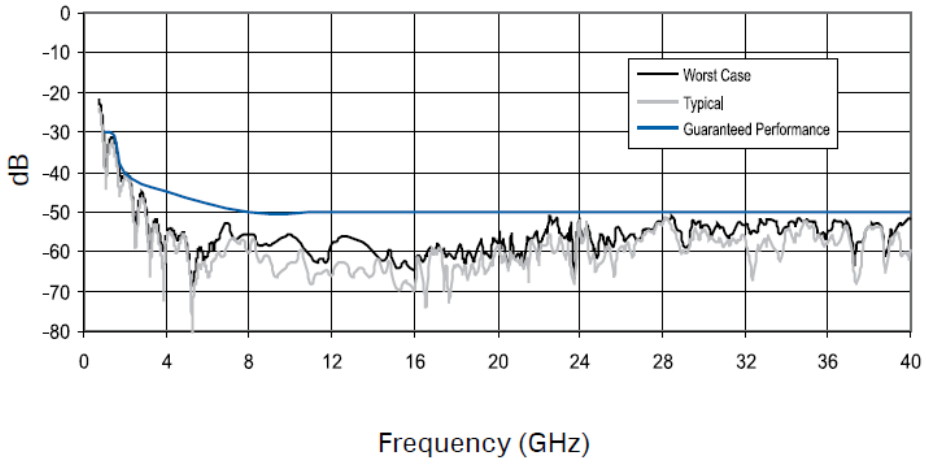


Figure E.2. The reflectivity results of pyramidal absorber EHP-8PCL model for ETS-Lindgren.

ÖZGEÇMİŞ

Serdar Gökçe, 1987 yılında İstanbul'da doğdu. İlkokul, Lise (Kartal Anadolu Lisesi) ve Üniversite öğrenimini İstanbul'da tamamladı. 2011 yılında Gebze Teknik Üniversitesi Fizik Bölümü'nden mezun olmuştur. 2013 yılında Marmara Üniversitesi 'nde yüksek lisansa başladı. 2013-2016 yılları arasında Tübitak tarafından desteklenen 113F118 numaralı "Mikrodalga soğurucu nanomalzemelerin (MISONAM) geliştirilmesi" projesinde asistan olarak yer aldı. Ulaştırma, Sanayi ve Ticaret Bakanlığı tarafından desteklenen 1611.TGSD.2015 numaralı "Yakıt Tankı Doluluk Seviyesi için Cihaz Üretimi ve Sistem Tasarımı, (2015-2016)" teknogirişim projesini tamamladı. Aynı yıl "PRODAR ARGE" isimli mikrodalga araştırma-geliştirmeye yönelik hizmet veren şirketin açılışını yaptı. 2015 yılında Marmara Üniversitesi Elektrik Elektronik Mühendisliği'nde yüksek lisansa başladı ve halen devam etmektedir.